Physik-Department

Lehrstuhl für Topologie korrelierter Systeme

Neutron scattering investigation of Ce based heavy fermion systems: from magnetism to unconventional phenomena

Philipp Geselbracht

Vollständiger Abdruck der von der Fakultät für Physik der Technischen Universität München zur Erlangung des akademischen Grades eines
Doktors der Naturwissenschaften (Dr. rer. nat.)
genehmigten Dissertation.

Vorsitzender: Prof. Dr. Norbert Kaiser
Prüfer der Dissertation:

1. Prof. Dr. Christian Pfleiderer
2. Prof. Dr. Philipp Gegenwart

Die Dissertation wurde am 31.8.2016 bei der Technischen Universität München eingereicht und durch die Fakultät für Physik am 05.12.2016 angenommen.

Abstract

In Ce based heavy fermion systems the hybridization of the 4f orbital of the Ce ion and the conduction band lead to unconventional phenomena such as quantum critical points or superconductivity. The aim of this thesis is to investigate and compare the magnetism on a microscopic scale within the heavy fermion families CeT_2X_2 (X = Si, Ge) and $CeTIn_5$. To do so neutron scattering was used as the experimental method.

For $CeCu_2Ge_2$, the antiferromagnetic order AF1 ($\vec{\tau}$ = (0.285 0.285 0.544)) is well described as a spin density wave with reduced ordered moments in $[1\bar{1}0]$ direction. The phase diagram with magnetic field applied along $[1\bar{1}0]$ direction was investigated. Two new phases were observed: the elliptical helix phase AF2 with modified propagation vector $\vec{\tau}$ = (0.34 0.27 0.55) and the C-phase with a yet unknown magnetic order. Above T_N, in zero field, short range order was observed, hinting competition of AF1 and AF2. It is assumed that both structures are due to different nesting properties of the Fermi surface. The RKKY character of the electronic system leads to effective Landé factors in the AF1 ($g^{\text{eff}} = 0.36$) and AF2 ($g^{\text{eff}} = 0.525$) phases. From the zero field dispersion the strength of the next nearest neighbor RKKY interactions was extracted, yielding $2SJ_1 = (-0.042 \pm 0.007)$ meV (basal plane) and $2SJ_2 = (-0.18 \pm 0.01)$ meV (body diagonal). Comparing the RKKY interaction to $CeCu_2Si_2$ and $CeNi_2Ge_2$ reveals a strong enhancement of the interaction in the basal plane going from antiferromagnetism ($CeCu_2Ge_2$) to superconductivity ($CeCu_2Si_2$) and finally paramagnetism ($CeNi_2Ge_2$). This new finding appears to be an important puzzle piece for the understanding of the CeT_2X_2 family as it suggests a dependence of the aniosotropy of the RKKY interaction from the hybridization strength of the 4f orbital and the conduction band.

The obtained phase diagram for $CeCu_2(Si_{0.55}Ge_{0.45})_2$ has large similarities to $CeCu_2Ge_2$ for large magnetic field.

For the $CeTIn_5$ compounds, superconducting samples were grown, i.e. $CeCo_xIr_{1-x}In_5$. The results indicate that no miscibility gap is present. For further neutron scattering studies, additional work will be required to make the growth process more reliable. Important directions how to do so, were developed from the growth attempts in this work.

Kurzfassung

In Ce basierten Heavy Fermion Systemen führt die Hybridisierung des 4f Orbitals der Ce-Ionen und des Leitungsbandes zu unkonventionellen Phänomenen wie beispielsweise quantenkritische Punkte oder Supraleitung. Ziel dieser Dissertation ist die Untersuchung und der Vergleich des Magnetismus auf mikroskopischer Skala innerhalb der Heavy Fermion Familien CeT_2X_2 (X = Si, Ge) und $CeTIn_5$. Als experimentelle Methode wurde hierfür Neutronenstreuung verwendet.

Die antiferromagnetische Ordnung AF1 ($\vec{\tau}$ = (0.285 0.285 0.544)) des $CeCu_2Ge_2$ lässt sich gut als Spindichtewelle mit reduzierten Momenten in $[1\bar{1}0]$-Richtung beschreiben. Bei der Bestimmung des Phasendiagrammes mit Magnetfeld in $[1\bar{1}0]$-Richtung wurden zwei neue Phasen beobachtet: Die elliptische Helixphase AF2 mit modifiziertem Propagationsvektor $\vec{\tau}$ = (0.34 0.27 0.55) und die C-Phase mit bisher unbekannter magnetischer Ordnung. Oberhalb von T_N wurde das Auftreten kurzreichweitiger Ordnung beobachtet, was auf Wettbewerb zwischen der AF1 und der AF2 Phase schließen lässt. Es ist anzunehmen, dass beide Strukturen verschiedener Nestingeigenschaften der Fermioberfläche entspringen. Der RKKY-Charakter des Elektronensystems führt zu verschiedenen effektiven Landé Faktoren in der AF1 ($g^{eff} = 0.36$) und AF2 ($g^{eff} = 0.525$) Phase. Aus der Nullfelddispersion wurden die über-nächste-Nachbarn RKKY Wechselwirkungen extrahiert. Das Ergebnis ist $2SJ_1 = (-0.042 \pm 0.007)$ meV (Basalebene) und $2SJ_2 = (-0.18 \pm 0.01)$ meV (Raumdiagonale). Der Vergleich mit den Wechselwirkungen in $CeCu_2Si_2$ und $CeNi_2Ge_2$ zeigt eine deutliche Verstärkung der Wechselwirkung in der Basalebene ausgehend von Antiferromagnetismus ($CeCu_2Ge_2$) über Supraleitung ($CeCu_2Si_2$) und schließlich Paramagnetismus ($CeNi_2Ge_2$). Dieses neue Ergebnis kann ein wichtiges Puzzleteil für das Verständnis der CeT_2X_2 Familie darstellen, da sie einen Zusammenhang zwischen der Anisotropie der RKKY Wechselwirkung und der Hybridisierung der 4f Orbitalen und des Leitungsbandes vermuten lässt.

Das für $CeCu_2(Si_{0.55}Ge_{0.45})_2$ erhaltene Phasendiagram hat große Ähnlichkeit mit dem von $CeCu_2Ge_2$.

Von den $CeTIn_5$ Verbindungen wurden supraleitende Proben, d. h. $CeCo_xIr_{1-x}In_5$, gewachsen. Die Ergebnisse zeigen, dass das System keine Mischungslücke aufweist. Für spätere Neutronenstreuung muss der Wachstumsprozess weiter verbessert werden. Wichtige Vorschläge wie dies zu erreichen ist, wurden aus den Ergebnissen der Wachstumsversuche abgeleitet.

Acknowledgements

Many people contributed to the success of this thesis due to their help and support. I would like to thank all of them and especially:

Prof. Dr. Christian Pfleiderer and **Prof. Dr. Winfried Petry** for giving me the opportunity to work on this thesis.

Dr. Astrid Schneidewind for her supervision of my work, the patient introduction in neutron scattering and her advice on the dos and don’ts of academic life.

The members of the **PANDA** group, namely **Dr. Alexandre Bertin**, **Dr. Petr Čermák**, **Dr. Peng Cheng**, **Dr. Joshua Lim**, **Dr. Markos Skoulatos** and **Florin Stoica**, who provided a great working atmosphere.

All the **local contacts** of the neutron scattering experiments, namely **Dr. Diana Quintero Castro**, **Dr. Kirill Nemkovski**, **Dr. Bjørn Pedersen**, **Dr. Karel Prokeš**, **Dr. Karin Schmalzl** and **Dr. Fabiano Yokaichiya** along with the **technical staff** of the neutron facilities **Heinz Maier-Leibnitz Zentrum**, **Helmholtz-Zentrum Berlin** and **Institut Laue-Langevin**. Without their dedicated support non of the neutron scattering experiments could have realized.

Prof. Dr. Michael Loewenhaupt and **Dr. Oliver Stockert** for their advice and the fruitful discussions.

Dr. Václav Petříček for his support with the Jana2006 software.

Dr. Micha Deppe for providing the $CeCu_2Ge_2$ single crystal.

Dr. Martin Rotter for providing the McPhase model and the fruitful discussions.

Prof. Dr. Vladimír Sechovský for financing by stay in stay in Prague and giving me the opportunity to work in his research group.

Dr. Marie Kratochvílová for her hospitality during my stay at the Charles University in Prague and all the help she provided with the sample preparation and characterization.

At the end, I would like to further thank my family and friends for alway supporting me during my busy PhD life.

Contents

Chapter 1

Introduction

The object of investigation of this thesis is the magnetism in the Ce based heavy fermion systems $CeCu_2Ge_2$, $CeCu_2(Si_{0.55}Ge_{0.45})_2$ and $CeTIn_5$ (T = Rh, Ir, Co) on the microscopic scale. In doing so, the gaps in existing research will be filled. The obtained results are used to compare the microscopic magnetic properties in the paramagnetic, superconducting and antiferromagnetic states.

For $CeCu_2Ge_2$, the incommensurate ($\vec{\tau}$ = (0.285 0.285 0.544)) antiferromagnetic structure of the AF1 phase was investigated using polarized and unpolarized neutron diffraction. The results indicate a spin wave structure. The T-B phase diagram up to 15 T (B$||$[$1\bar{1}0$]) was also investigated using neutron diffraction. The magnetic order in the newly found AF2 phase was identified as an elliptical helix with incommensurate propagation vector $\vec{\tau}$ = (0.34 0.27 0.55). An investigation of the transition lines revealed a 2nd order transition of the AF2 phase at high temperature while at low temperature the phase transitions are 1st order. The investigation of the low energy ($E < 4$ meV) magnetic excitation spectrum using neutron triple axis spectroscopy revealed single site fluctuations due to the Kondo effect and inter site spin wave excitations due to the RKKY interaction. The comparison of the RKKY interaction to $CeCu_2Si_2$ and $CeNi_2Ge_2$ shows a strong enhancement of the interaction in the basal plane going from antiferromagnetism ($CeCu_2Ge_2$) to superconductivity ($CeCu_2Si_2$) and finally paramagnetism ($CeNi_2Ge_2$). This new finding appears to be an important puzzle piece for the understanding of the CeT_2X_2 family as it suggests a dependence of the aniosotropy of the RKKY interaction from the hybridization strength of the 4f orbital and the conduction band.

For $CeCu_2(Si_{1-x}Ge_x)_2$, the T-B phase diagram was investigated. For large magnetic field it shows similarities to the T-B phase diagram of $CeCu_2Ge_2$.

For the $CeTIn_5$ (T = Rh, Ir, Co) compounds, the general objective is the study of the low energy excitation spectrum in the superconducting state of $CeCo_xIr_{1-x}In_5$ with inelastic neutron scattering. In this thesis, the feasibility of such an investigation is done by the verification of the published composition phase diagram to rule out a miscibility gap as well as by establishing an initial baseline for the preparation of samples suitable for the inelastic neutron scattering. This is done using In self-flux growth for sample preparation and standard lab characterization techniques, i.e. energy dispersive X-ray spectroscopy, X-ray diffraction and specific heat measurements. The results indicate that no miscibility gap is present. For further neutron scattering studies, additional work will be required to make the growth process more reliable. Promising steps to do so are the prealloying of the starting materials, changing the amount of In-flux and altering the colling profile.

This thesis is organized in the following main chapters:

- **chapter 2** summarizes the current state of research on the CeT_2X_2 (X = Si, Ge) and $CeTIn_5$ (T = Rh, Ir, Co) compounds.
- **chapter 3** presents the experimental realization of the neutron scattering experiments and the material preperation.
- **chapter 4** presents the results on $CeCu_2Ge_2$. The magnetic structure is solved for B = 0 T, the T-B phase diagram is investigated and the magnetic RKKY interaction strength is determined. A comparison to the magnetic interactions in $CeCu_2Si_2$ and $CeNi_2Ge_2$ is made.
- **chapter 5** presents the results on the $CeCu_2(Si_{1-x}Ge_x)_2$ phase diagram. The results will be compared to the phase diagrams of $CeCu_2Ge_2$.
- **chapter 6** presents the initial growth attempt of $Ce(Co/Ir)In_5$ single crystals with the general objective of an inelastic neutron scattering investigation.
- **chapter 7** gives a summary of the obtained results in this thesis.

Chapter 2

Ce-based Heavy Fermion Systems

The effective electron mass m^* in heavy fermion systems is on the order of magnitude of 100-1000 times the free electron mass. For comparison, in semiconductor materials, the effective mass is on the order of magnitude of one or less of the free electron mass. The strict, even though arbitrary, definition is that a compound with Sommerfeld coefficient $\gamma > 400$ mJ/molK^2 is called heavy fermion system [1]. Heavy fermion systems contain elements with partially filled 4f or 5f shells, i.e. lanthanide or actinide elements. In Ce based heavy fermion systems this is realized if Ce^{3+} ($4f^1$) ions are present. According to Hund's rule the total angular momentum is 5/2 and therefore a magnetic moment is expected for the ions. The distance between the ions is larger than 4 Å preventing an overlap of f states. Without hybridization with the s, p or d states, which form the conduction band, the magnetic moments are localized [1]. Indeed, at high temperature, above the boiling point of liquid nitrogen, the susceptibility of heavy fermion systems follows the Curie-Weiss law with moments of the order of the free ion value 2.54 μ_B [2; 3].

At low temperature the magnetism is determined by the crystalline electric field and the hybridization between the f states and the conduction band. The hybridization leads to reduced magnetic moments of the ions and a delocalization of the f electrons. Some compounds undergo a superconducting phase transition (e.g. $CeCu_2Si_2$ [4], $CeCoIn_5$, $CeIrIn_5$ [5]) or an antiferromagnetic phase transition (e.g. $CeCu_2Ge_2$, $CeRhIn_5$ [6]) while other remain paramagnetic (e.g. $CeAl_3$ [2], $CeCu_6$ [1]).

It is possible to tune the compounds between the different phases using either chemical substitution, pressure or magnetic field. Examples for tuning by alloying are the CeT_2X_2 compounds which become antiferromagnetic, superconducting or paramagnetic, depending on the element T and X, as well as antiferromagnetic $CeRhIn_5$ that becomes superconducting by substituting Rh with Co or Ir. $CeRhIn_5$, $CeCu_2Ge_2$ and

$CeAu_2Si_2$ become superconducting under pressure. $CeCu_{5.8}Au_{0.2}$ can be tuned by magnetic field from antiferromagnetic to paramagnetic [7]. A schematic overview of the resulting three-dimensional phase diagram is shown in Fig. 2.1.

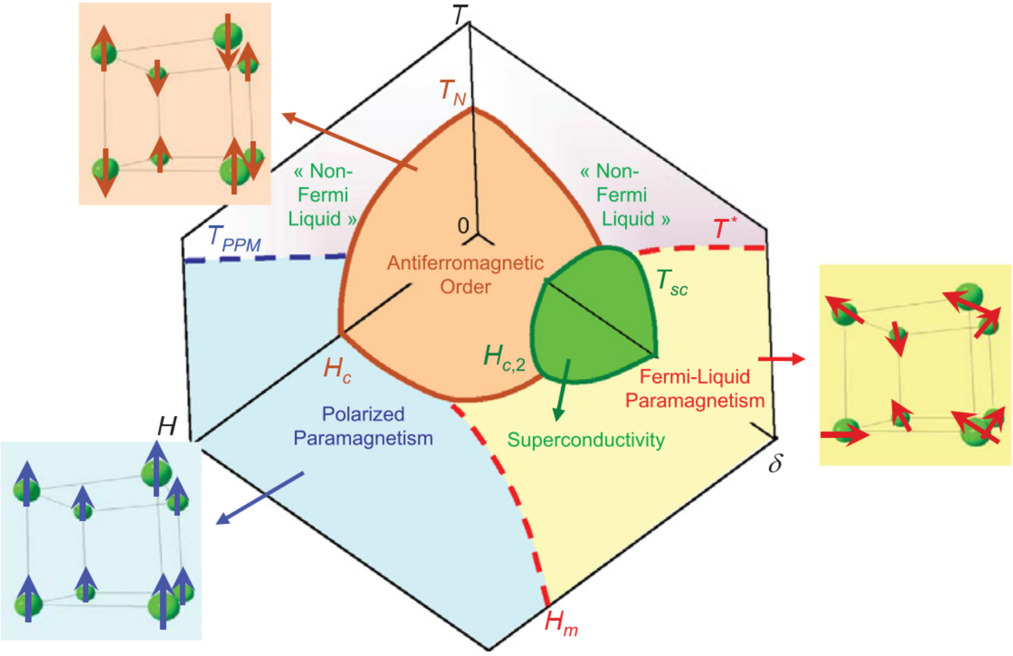

FIGURE 2.1: Schematic three-dimensional (T, δ, B) phase diagram of heavy-fermion systems close to an antiferromagnetic-to-paramagnetic quantum instability, where δ can be the pressure or alloying [8].

For tuning by substitution as well as tuning by pressure the following line of reasoning is established in literature: substitution or pressure controls both the Kondo effect and the RKKY interaction via the hybridization strength J between the f and the conduction electrons. Kondo effect and RKKY interaction compete with each other. If the RKKY interaction predominates, magnetic order is established. If the Kondo effect predominates the compound is paramagnetic. If both are on similar energy scale, unconventional phenomena such as quantum critical points or superconductivity emerge. So far no generally accepted theoretical framework exists

For the magnetic field the situation is even less clear. Sufficient high field is expected to force all magnetic moments along the direction of the field, resulting in polarized paramagnetism. For intermediate magnetic field, metamagnetic transitions are expected due to the interaction of the magnetic moments with the magnetic field. The exact nature of the meatmagnetic transition depends heavily on the on the conditions of the compound. Additionally, magnetic field induced modifications of the fermi surface were reported for $CeRu_2Si_2$ [9].

2.1 Effect of the crystalline electric field on the Ce ion

Without hybridization, the magnetic properties of Ce-based compounds are determined by the Ce-ion in its local environment. The free Ce^{3+} ion with J = 5/2 is 2J+1 = 6 times degenerate with the moment $\mu_{\mathrm{free}} = g\mu_{\mathrm{B}}\sqrt{J(J+1)} = 2.54\ \mu_{\mathrm{B}}$. If the Ce ion is incorporated in a crystal lattice, it is subject to the electrical field from the surrounding ions. This field is called the crystalline electric field (CEF). As a result, the 5/2 ground state splits, lifting the degeneracy.

In rare earth elements the splitting due to the CEF is smaller than the spin-orbit energy [10]. Thus, only the lowest J multiplet has to be considered [11] and the Hamiltonian can be expressed as

$$H_{\mathrm{CEF}} = \sum_{l,m} B_l^m O_l^m \tag{2.1}$$

O_l^m are the Stevens Operators and B_l^m the CEF parameters in Stevens notation [12]. In tetragonal systems Eq. 2.1 becomes

$$H_{\mathrm{CEF}} = B_2^0 O_2^0 + B_4^0 O_4^0 + B_4^4 O_4^4 \tag{2.2}$$

The magnetic properties of the Ce ion can be calculated from the three parameters B_2^0, B_4^0 and B_4^4 then.

Adjacent charges are placed on the z axis to the Ce ion. As a result, the charge distribution for the 5/2 multiplet is oblate, while the 1/2 multiplet is prolonged. The deformation leads first of all to a preferred direction of the magnetic moment and thereby to a coupling of the of the magnetic moments to the crystal lattice. Second, the size of the moments is altered from the free ion value.

2.2 The Doniach phase diagram: competition between the RKKY interaction and the Kondo effect

The RKKY interaction, introduced by Ruderman, Kittel, Kasuya und Yosida [13; 14; 15], describes a long range indirect interaction between local magnetic atoms via the polarization of the conduction band electrons. The electrons of two magnetic atoms both interact with the conduction band electrons by the spin-spin interaction, leading to an exchange constant depending of the distance r of the atoms [16].

$$J_{\mathrm{RKKY}}(r) \propto -J^2 g(E_{\mathrm{F}}) \frac{cos(2k_{\mathrm{F}} r)}{(k_{\mathrm{F}} r)^3} \tag{2.3}$$

The sign of J_{RKKY} changes periodically with $2k_{\mathrm{F}}r$, leading to either ferromagnetic ($J_{\mathrm{RKKY}} > 0$) or antiferromagnetic ($J_{\mathrm{RKKY}} < 0$) order.

The characteristic energy scale and temperature for the RKKY Interaction is

$$E_{RKKY} = k_B T_{RKKY} \propto J^2 g(E_f) \tag{2.4}$$

We turn now to the Kondo effect. In metals without magnetic impurities, the resistivity is expected to decrease monotonically on reducing the temperature due to electron-phonon scattering. If magnetic impurities are introduced to an otherwise non magnetic crystal lattice, non-monotonic temperature dependence is observed. This is called the Kondo effect [17]. Kondo modeled this by coupling the local magnetic moment to the spins of the conduction electrons via an exchange interaction J. The result is an additional logarithmic term in the resistivity, explaining the nonmonotonic temperature dependence. For temperature below the characteristic Kondo temperature T_{K}

$$k_B T_K \propto \frac{1}{g(E_{\mathrm{F}})} \exp\left(-\frac{1}{Jg(E_{\mathrm{F}})}\right) \tag{2.5}$$

spin-flip scattering at a magnetic impurity localizes the conduction electrons and screen the magnetic moment. The situation can be pictured as the electron spins of the scattered conduction electrons align anti parallel to the spin of the magnetic ion forming a cloud of of electrons around the magnetic ions.

As the energy scales of both the RKKY interaction and the Kondo effect depend heavily on the exchange interaction J between 4f and conduction electrons, competition between the ordering RKKY interaction and the screening Kondo effect occur. The behavior of a system, depending on J, can be easily summarized in the Doniach phase diagram [18]. For small J the quadratic scaling RKKY interaction dominates, leading to (anti-)ferromagnetic order. Increasing J leads to exponential increase of the Kondo screening, weakening the magnetic order established by RKKY. Eventually the Kondo screening will exceed the ordering RKKY interaction at J_c and the ordering temperature vanishes. At this point, a quantum critical point occurs. For $J > J_{\mathrm{c}}$ the system is in a paramagnetic state as Kondo energy scale exceeds by far that of the RKKY interaction.

2.3 Metamagnetic phase transitions: the spin-flop transition

In this section the principle of metamagnetic phase transition will be discussed for the simple case of the so-called spin-flop transitions.

If the scale of an externally applied magnetic field exceeds the internal magnetic forces, the magnetic moments are forced to align parallel to the magnetic field. This can be observed in the saturation of the magnetization at sufficient high field. If the magnetic moments of the zero field structure are perpendicular to the magnetic field, one can expect that the moments continuously rotate in the field direction upon increasing the field. If the zero field structure is antiferromagnetic with moments parallel or antiparallel to the field direction a spin flop transition may occur.

Consider a simple two sublattice antiferromagnet with one sublattice M_+ parallel and one antiparallel M_- to the magnetic field B. For simplicity B is along the easy axis. The total Energy E at $T = 0$ for the magnetic structure is then given as [19]

$$E = \underbrace{-AM^2\cos(\Theta+\Phi)}_{\text{spin-spin interaction}}\underbrace{-\tfrac{1}{2}\Delta(\cos(\Theta)^2+\cos(\Phi)^2)}_{\text{spin-lattice interaction}}\underbrace{-MB\cos(\Theta)-MB\cos(\Phi)}_{\text{spin-magnetic field interaction}} \tag{2.6}$$

Θ is the angle of M_+ and Φ is the angle of M_- to the field. The first term corresponds to a spin-spin exchange interaction preventing the spins from aligning along the magnetic field and inducing antiferromagnetic order in zero field. The second term arises from the coupling to the crystal lattice and the third term corresponds to the Zeeman energy of each spin in magnetic field.

The energy for the zero field structure ($\Theta = 0$, $\Phi = 180^\circ$) is $E_{\mathrm{ZF}} = -AM^2 - \Delta$ and for the spin-flop ($\Theta = \Phi$) the energy is

$$E_{\mathrm{SF}} = -AM^2\cos(2\Theta) - \Delta\cos^2(\Theta) - 2MB\cos(\Theta) \tag{2.7}$$

If $E_{\mathrm{ZF}} = E_{\mathrm{SF}}$ at $B_{\text{spin-flop}}$, a spin flop transition occurs. The magnetization is shows a step at $B_{\text{spin-flop}}$.

In [20], a phase diagram for a spin-flop transition was derived (Fig. 2.2). T_{N} marks the Néel-temperature of the zero field phase, while T'_{N} marks the Néel-temperature of the spin-flop phase. At $B = 0$ the transition temperatures satisfy $T_{\mathrm{N}} > T'_{\mathrm{N}}$. As T_{N} is suppressed faster than T'_{N} upon applying field, a crossover point is reached at $B \gtrsim B_{\text{spin-flop}}$.

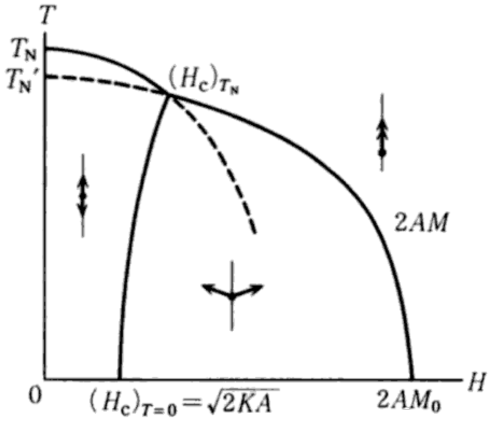

FIGURE 2.2: T-B=$\mu_0 H$ phase diagram for a spin-flop transition [20].

If Δ is sufficient large, the spins of the M_- sublattice will directly flip in the direction of the field and thus the polarized state is reached. This is called a spin-flip transition.

In the CeT_2X_2 (X = Si, Ge) compounds, the the interplay of the Kondo effect, the RKKY interaction and crystal electric field may lead to a much more complcated situation.

2.4 Current research on $CeCu_2Ge_2$

2.4.1 The CeT_2X_2 (X = Si, Ge) compounds

The CeT_2X_2 compounds are heavy fermion systems, where T is a transition metal and X a group IV semiconductor either Silicon or Germanium. CeT_2X_2 crystallizes in the tetragonal body centered $ThCr_2Si_2$ structure (space group I4/mmm) [21]. The Wyckoff positions as well as an illustration of the unit cell are given in Tab. 2.1 and Fig. 2.3, respectively.

atom	multiplicity	Wyckoff letter	coordinates
Ce	2	a	(0,0,0)
T	4	d	(0,1/2,1/4) (1/2,0,1/4)
X	4	e	(0,0,z) (0,0,-z)

TABLE 2.1: Wyckoff positions in CeT_2X_2 ($ThCr_2Si_2$ type, space group I4/mmm). T = transition metal, X = Si, Ge.

A classification of the isoeletronic CeT_2X_2 (T = Cu, Ag, Au and X = Si, Ge) compounds as well as $CeNi_2Ge_2$ is shown in Fig. 2.4. The phase boundary of the magnetically ordered phase (AFM) follows that of the Doniach phase diagram. A superconducting dome around the quantum critical point is assumed here. $CeAg_2Ge_2$, $CeAu_2Si_2$,

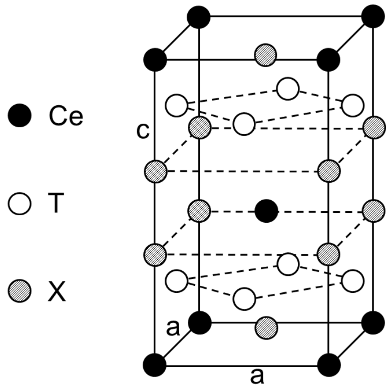

FIGURE 2.3: Nuclear structure of CeT_2X_2 ($ThCr_2Si_2$ type, space group I4/mmm). T = transition metal, X = Si, Ge.

$CeAg_2Si_2$ are located closely together in the $T_K << T_{RKKY}$ regime [22]. In $CeAg_2Ge_2$, the magnetic structure is an incommensurate spin-density-wave with moments along the a-direction and incommensurate propagation vector $\vec{\tau}_{CeAg_2Ge_2}$ = (0.28 0 0.9) [23]. An incommensurate spin-density-wave ($\vec{\tau}_{CeAg_2Si_2}$ = (0.685 0 0)) with moments along the a-direction is also assumed for $CeAg_2Si_2$, but a distinction from a square-wave structure could not be made [23]. For $CeAu_2Si_2$, the magnetic moments are aligned along the c-direction with alternating signs of the moments on the edge and body center Ce-ions [23]. $CeAu_2Ge_2$ is not explicitly mentioned in the classification of [22]. Its ordering temperature $T_K^{CeAu_2Ge_2}$ = 16 K is very close to that of $CeAu_2Si_2$ ($T_K^{CeAu_2Si_2}$ = 10 K) and also a similar magnetic structure was reported [24]. Therefore, it is reasonable to classify $CeAu_2Ge_2$ along its Si counterpart $CeAu_2Si_2$ in the phase diagram.

$CeCu_2Si_2$ becomes either antiferromagnetic (historically labeled A) at $T_N^{CeCu_2Si_2}$ = 0.8 K, superconducting (labeled S) at $T_C^{CeCu_2Si_2}$ = 0.5 - 0.7 K or both (labeled A/S). The Kondo temperature is $T_K^{CeCu_2Si_2} \approx$ 10 - 15 K. The magnetic structure of $CeCu_2Si_2$ (A) has not been determined yet. A strongly reduced ordered moment $\mu_{ord}^{CeCu_2Si_2}$ = 0.1 μ_B (compared to $\mu_{Ce^{3+}}$ = 2.54 μ_B) was estimated by assuming a spin-density-wave structure with moments along [110] [25]. From the investigation of $CeCu_2(Si_{1-x}Ge_x)_2$ with x = 0.18 and x = 0.45, also a cycloidal structure is plausible [26; 27; 28]. $CeCu_2Si_2$ has to be placed right at the point were the magnetic order is suppressed and replaced by superconductivity. This is evidenced by the calculation of the f-d hybridization strength [22], the sample depended occurrence of either magnetic order or superconductivity [29], the strongly reduced ordered moment [25] and the slowing down of the spin dynamics near the quantum critical point [30].

$CeNi_2Ge_2$ is not isoelectronic to CeT_2X_2 (T = Cu, Ag, Au and X = Si, Ge). It stays paramagnetic even down to 70 mK [31]. Below $T_K \approx$ 30 K, inelastic neutron scattering [32] revealed stripes of magnetic intensity on the energy scale $\approx$ 4 meV with a maximum

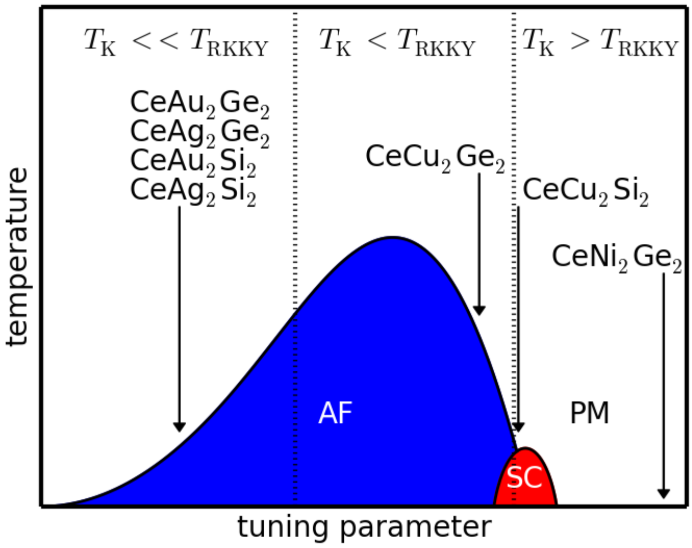

FIGURE 2.4: Classification of the isoelectronic CeT_2X_2 (T = Cu, Ag, Au and X = Si, Ge) compounds as well as $CeNi_2Ge_2$.

corresponding to a wave vector $\vec{\tau}_1^{CeNi_2Ge_2} = (0.23\ 0.23\ 0.5)$. Because of this propagation vector is very similar to that of $CeCu_2Ge_2$ and $CeCu_2Si_2$, it is included in this discussion. The stripes are in the HH direction, while in L direction the fluctuations decay fast (FWHM along L is 0.2 r.l.u.). No dispersion was observed. Comparing the evolution of the inelastic intensity in several Brillouin zones confirms the fluctuations are in the basal plane. The fluctuations have a quasi-two-dimensional character.

Additionally, low energy excitation with energy scale 0.6 meV are present at $\vec{\tau}_2^{CeNi_2Ge_2} = (0.5\ 0.5\ 0)$ and $\vec{\tau}_3^{CeNi_2Ge_2} = (0\ 0\ 0.75)$ [33]. The fluctuations at $\vec{\tau}_2^{CeNi_2Ge_2}$ are also confined to the basal plane. The non Fermi-liquid behavior of the specific heat is a direct result of the low energy excitations. The temperature scaling of the total excitation spectrum is not in line with the expected temperature scaling for a quantum critical point. Thus, [33] concluded that $CeNi_2Ge_2$ is considerably far in the paramagnetic region. This view is supported by the more than two times larger Kondo temperature compared to $CeCu_2Si_2$.

In the compound investigated in this work, $CeCu_2Ge_2$, antiferromagnetic order is established at $T_N = 4.2$ K. Susceptibility data published in [34] point towards a magnetic structure with moments in the basal plane. The propagation vector $\vec{\tau}^{CeCu_2Ge_2} = (0.284\ 0.284\ 0.543)$ has been deduced from neutron powder diffraction in the 1980ies and 1990ies [35; 36]. An analysis based on the same neutron powder diffraction data set yielded either a spiral structure with $\mu_{ord}^{CeCu_2Ge_2,spiral} = 0.7\ \mu_B$ [35] or a spin-density-wave with a not further specified moment direction and $\mu_{ord}^{CeCu_2Ge_2,SDW} = 1.0\ \mu_B$ [36].

An initial inelastic neutron scattering investigation of magnetic excitations in $CeCu_2Ge_2$ using powder samples was previously reported in [37] and [35]. In this early investigation the CEF scheme was derived. The ground state doublet is dominated by the $|5/2>$ state. Two energetically degenerate excited doublets are separated from the ground state by approximately 200 K. Corrected CEF parameters were reported in [38], establishing B_2^0 = -10.26 K, B_4^0 = -0.056 K and B_4^4= 2.67 K. These are in line with the specific heat [39] and susceptibility [40].

Furthermore, [37] and [35] also investigated the temperature dependence of the quasi elastic line width Γ for $T > T_N$, which is inversely proportional to the spin relaxation rate. Γ follows the $\Gamma = \Gamma_0 + \gamma\sqrt{T}$ scaling for $T > T_N$, that is expected for Ce^{3+} metals [11]. The extracted Kondo temperature is $T_K^{CeCu_2Ge_2} = 6$ K. For $T < T_N$, a pronounced peak around 0.9 meV was reported. It was speculated that this peak corresponds to spin wave excitations. The existence of spin wave excitations is anticipated from the specific heat which follows the T^3 scaling for antiferromagnets [41; 42; 40].

The electronic band structure of $CeCu_2Ge_2$ was calculated in the local density approximation assuming either localized or itinerant 4f states [43]. In both cases the calculation predict $CeCu_2Ge_2$ to be a metal. In the localized model, no nesting with the experimentally observed propagation vector is present. In contrast, the itinerant model shows nesting for the experimentally observed propagation vector.

Based on the classification in [22], the reduced ordered moment, the fact that $T_K \approx T_N$ and the result of the band structure calculation, $CeCu_2Ge_2$ is classified in the $T_K < T_{RKKY}$ regime.

A detailed investigation of the spin wave dispersion in correlation with the magnetic structure should give an insight into the RKKY interaction in $CeCu_2Ge_2$. This will further enable a comparison to the superconducting $CeCu_2Si_2$, where the RKKY interaction was investigated via the paramagnon dispersion [25]. Also a comparison with the high energy fluctuations in $CeNi_2Ge_2$ will be possible then.

2.4.2 Hydrostatic pressure tuning of $CeCu_2Ge_2$

It has been demonstrated by [44], that the antiferromagnetic $CeCu_2Ge_2$ can be tuned by hydrostatic pressure to a similar state as $CeCu_2Si_2$. Their results are summarized here. The pressure dependence of the relevant temperature scales in $CeCu_2Ge_2$ is shown in Fig. 2.5. At low pressure, the temperature dependence of the resistivity shows two maxima T_1^{max} and T_2^{max} due to the Kondo effect, where conduction electrons scatter on the Ce^{3+} ion ground state at high temperature and on the CEF ground state

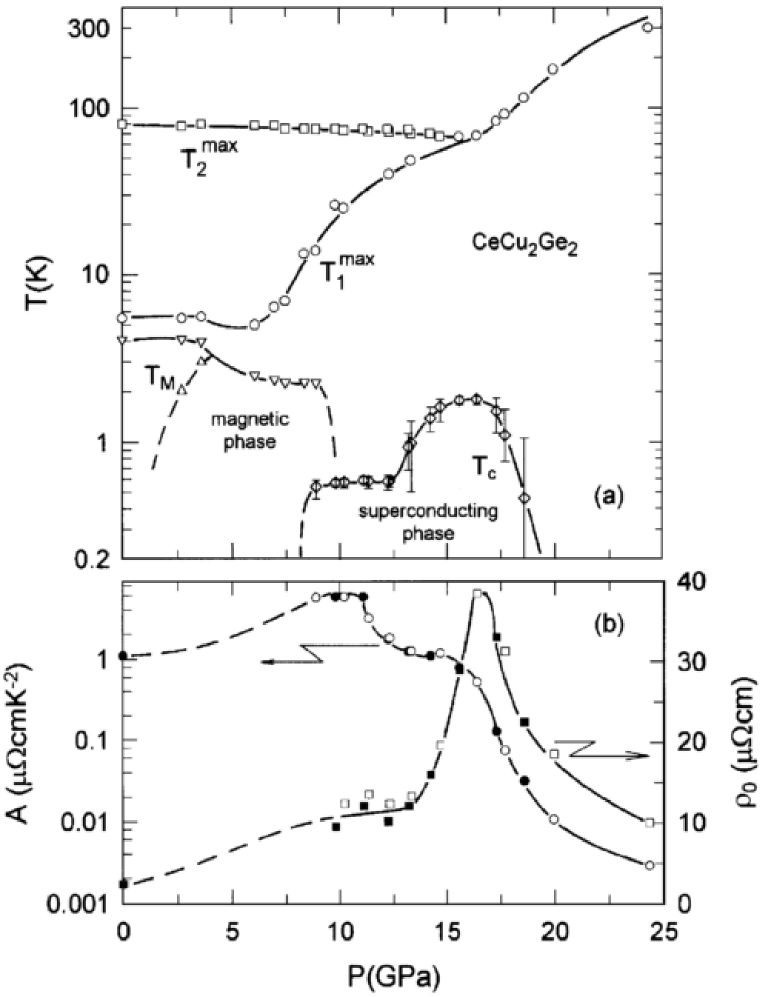

FIGURE 2.5: Pressure dependence of the magnetic ordering T_M, superconducting transition T_c and the resistivity maxima T_1^{max} and T_2^{max}. Vertical bars indicate the width of superconducting transition. (b) Pressure dependence of the residual resistivity ρ_0 and of the coefficient A in $\rho = \rho_0 + AT^2$ [44].

at low temperatures. While T_2^{max} remains constant over a large pressure range, T_1^{max} increases rapidly for $7 < P < 15$ GPa until T_1^{max} and T_2^{max} eventually merge. The occurrence of two maxima in the temperature dependence of the resistivity is a typical sign for low Kondo temperature, the increase of T_1^{max} and eventual merging with T_2^{max} can be interpreted as a rise of Kondo temperature. It is accompanied by a decrease and eventually suppression of the magnetic ordering temperature T_M to zero at 10 GPa. This resembles the situation in the Doniach phase diagram, where the exchange interaction is tuned by the applied pressure.

Just before T_M is tuned to zero, the superconducting phase emerges and $T_c \approx 0.6$ K is constant up to 13 GPa. Then, T_c reaches a maximum at 16 GPa, coinciding with the merging of T_1^{max} and T_2^{max}. Also a peak in ρ_0 appears and the coefficient A drops two orders of magnitude. As A is related to the effective mass m* $\propto \sqrt{A}$, two regimes of effective masses can be identified. In [44], it is speculated that this corresponds to a change in valence from Ce^{3+} to Ce^{4+}.

2.4.3 Composition tuning of $CeCu_2Ge_2$: Si substitution

As the $CeCu_2(Si_{1-x}Ge_x)_2$-series has no miscibility gap, it has been the subject of investigations following the transition from antiferromagnetic order in $CeCu_2Ge_2$ to superconductivity in $CeCu_2Si_2$. The introduction of the larger Ge to $CeCu_2Si_2$ serves as negative chemical pressure. Applying pressure on $CeCu_2(Si_{1-x}Ge_x)_2$ may be used to tune the system towards a similar state as $CeCu_2Si_2$ at ambient pressure. Various phase diagrams, depending on the Ge concentration, were derived [45; 46; 42; 47; 48]. The most recent one from [48] for $0 \leq x \leq 0.5$, that used the optimized growth process, described in [47], is shown in Fig. 2.6 (left).

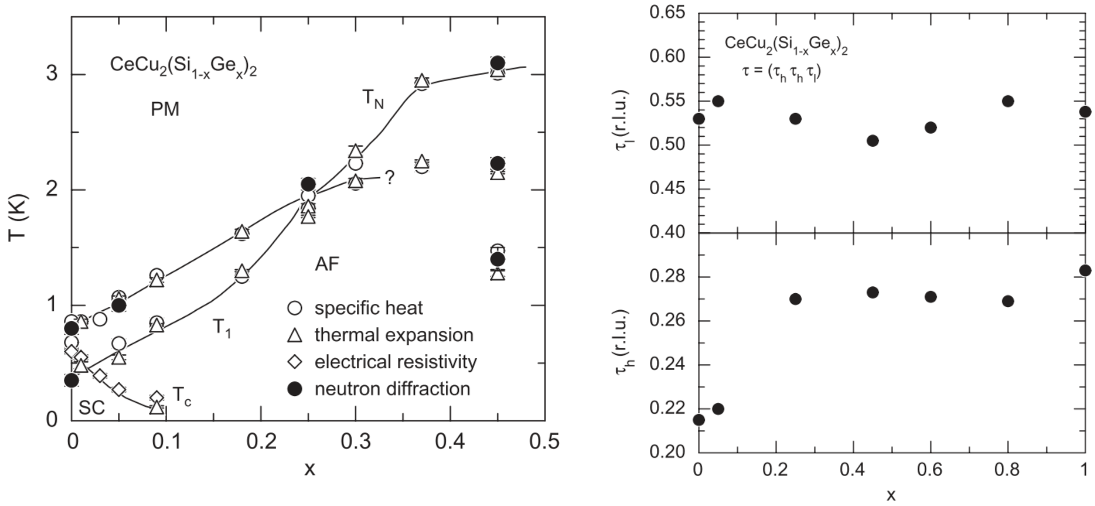

FIGURE 2.6: Left: x-T phase diagram for $CeCu_2(Si_{1-x}Ge_x)_2$. From [27], data are from [48] and references there in. Right: Components of the propagation vector $\vec{\tau} = (\tau_h\ \tau_h\ \tau_l)$ in $CeCu_2(Si_{1-x}Ge_x)_2$ as a function of Ge concentration x. From [27], and references there in.

The existence of magnetic order was confirmed for x = 0.05, 0.25, 0.45 with an incommensurate propagation vector $\vec{\tau} = (\tau_h\ \tau_h\ \tau_l)$. For $x < 0.1$, the h component τ_h is smallest ($\tau_h^{x<0.1} = 0.22$), while it is $\tau_h^{0.1<x<0.9} = 0.27$ for $0.1 < x < 0.9$ and further raises to $\tau_h^{x=1} = 0.285$ for x =1. The l component τ_l is approximately constant ($0.50 < \tau_l < 0.55$) for the whole x range. The magnetic moments decrease substantially with the Si concentration $(1 - x)$ [27]. This can be attributed to increasing Kondo screening, consistent with resistivity data [47]. A comparison of the diffraction pattern for $x = 0.18$ and $x = 0.45$ did not show any change of magnetic structure [28].

Introducing a relative pressure $\Delta p = p - p_{c1}$, where p is the experimentally applied pressure and p_{c1} is a characteristic pressure offset depending on x, the phase diagrams of

$CeCu_2(Si_{1-x}Ge_x)_2$ with different x can be superimposed as in Fig. 2.7 (a) [49]. In $CeCu_2Si_2$ and $CeCu_2Ge_2$ under pressure, superconductivity exists in a strangely deformed phase, even sometimes called “potato” [50]. In the $CeCu_2(Si_{1-x}Ge_x)_2$ series with x = 0.1, the superconducting phase dismantles in two separate domes under pressure around p_{c1} and p_{c2} [51].

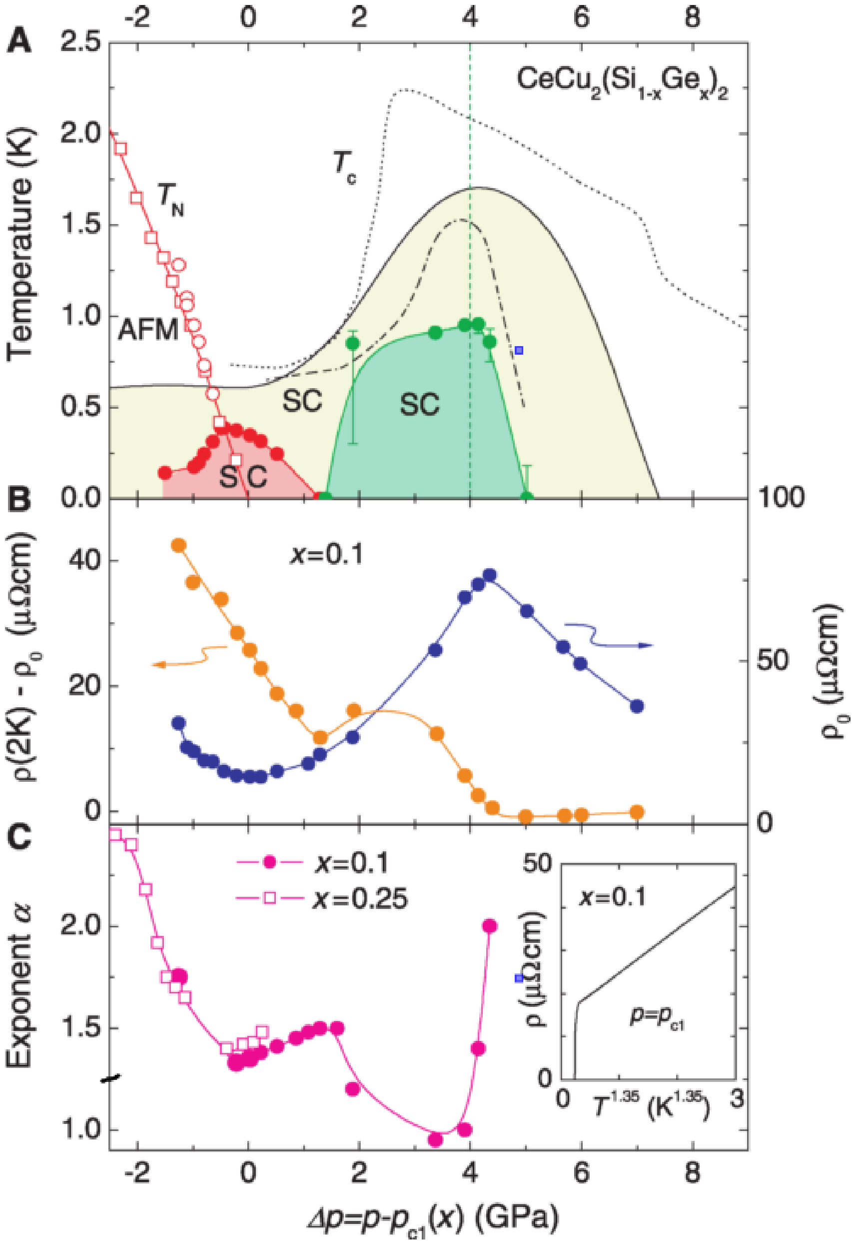

FIGURE 2.7: Relative pressure $\Delta p = p - p_{c1}$ dependence of the $CeCu_2(Si_{1-x}Ge_x)_2$ series showing (A) the phase diagram with the antiferromagnetic temperature T_N and superconducting transition T_c; (B) residual resistance ρ_0 (right) and low temperature scattering $\rho(2K) - \rho_0$ (left); (C) power law T^α coefficient α. Δp depends on the Ge concentration as explained in the text. The symbols in (A) are organized in the following way: circles x = 0.1 (p_{c1} = 1.5 GPa); squares x = 0.25 (p_{c1} = 2.4 GPa); continuous line x = 1 (p_{c1} = 11.5 GPa, data from [44]); dashed line x = 0 (p_{c1} = 0.4 GPa, data from [52]); dotted-dashed line x = 0 (p_{c1} = 0 GPa, data from [53]). Figure from [49].

In the following, the results of [49] are reproduced, if not stated otherwise. The separation into distinct domes was attributed to the introduction of additional disorder with the Ge atoms, weakening the superconductivity. Measurements of the temperature dependence of the upper critical field in $CeCu_2(Si_{0.9}Ge_{0.1})_2$ revealed, that the superconducting coherence length increases upon approaching p_{c1}, pointing toward antiferromagnetic fluctuation mediated superconductivity in the vicinity of quantum critical point. Also the resistivity (Fig. 2.7 (b) and (c)) shows non-Fermi liquid behavior in the normal state similar to other heavy fermion compounds, where the superconductivity is attributed to the presence of an antiferromagnetic quantum critical point, namely in $CePd_2Si_2$ and $CeIn_3$ [54]. X-ray diffraction at p_{c2} revealed a volume collapse in $CeCu_2Ge_2$ under pressure [55]. It is accompanied by a maximum of the residual resistivity ρ_0 and a linear temperature dependence of the resistivity (see Fig. 2.7 (b) and (c)). This can be interpreted as the presence of valence fluctuations of the Ce-ion [56; 57], leading then to the second superconducting dome.

2.4.4 Composition tuning of $CeCu_2Ge_2$: Ni doping

Additionally to the Si substitution, the possibility of Ni doping was explored. Ni is incorporated on the 4d Wyckoff position, replacing the Cu instead of the Ge.

A phase diagram for the $Ce(Cu_{1-x}Ni_x)_2Ge_2$ series was reported by [58]. Two different phases, marked by T_{N1} and T_{N2} in Fig. 2.8, are present. For low Ni concentration $x < 0.2$, the propagation vector stays close to the one in $CeCu_2Ge_2$. For $0.2 < x < 0.8$ a different type of magnetic order is present. [59] reported for $x = 0.28$ a longitudinal spin-density-wave with $\vec{\tau}_{x=0.28} = (0.11\ 0.11\ 0.25)$ and reduced moments $\mu_{x=0.28} = 0.7$ μ_B. For $x = 0.5$ a spiral or spin-density-wave with $\vec{\tau}_{x=0.5} = (0\ 0\ 0.14)$ and $\mu_{x=0.5} = 0.3\ \mu_B$ was reported. For $0.5 < x < 0.8$, the ordered moment is smaller than 0.2 μ_B and for $x > 0.8$, $Ce(Cu_{1-x}Ni_x)_2Ge_2$ is paramagnetic.

Based on the short propagation vector and the reduced moments for $0.2 < x < 0.8$, [59] concluded that at $x = 0.2$, a change from local moment magnetism to itinerant band mechanism is present. This picture is supported by calculation based on a simplified Kondo lattice model [60]. The valley of the magnetic transition temperature around $x = 0.2$ could not be reproduced, but is interpreted as competition between both ordering mechanisms.

In contrast, [36] argued that the Kondo screening is on the same order of magnitude for $x < 0.2$ and $0.5 < x < 0.8$ as seen from the Kondo temperature in Fig. 2.8 and hence the magnetic moments should be localized in both regimes. It was proposed that the change of the magnetic structure is due to a change of the environment for the

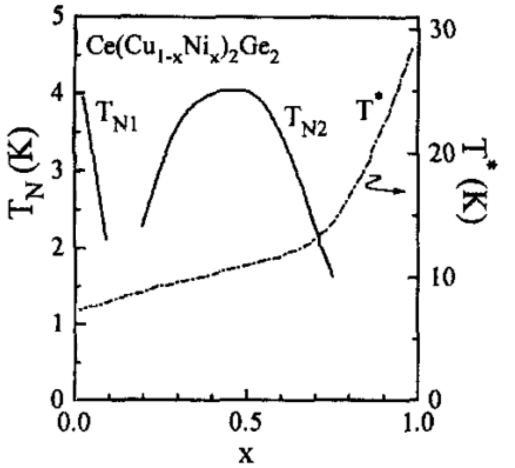

FIGURE 2.8: Phase diagram of $Ce(Cu_{1-x}Ni_x)_2Ge_2$. T_{N1} and T_{N2} indicate the respective Néel temperature and T^* indicates the Kondo temperature. [58]

Ce ion, e.g. the number of Ni next-neighbors. In this picture, local moment magnetism is always present regardless of x. The RKKY interaction is exceeded by the Kondo screening for $x > 0.8$. The situation is very similar to that of $CeCu_2Ge_2$ under pressure or as in the $CeCu_2(Si_{1-x}Ge_x)_2$ series. This interpretation is further supported by NMR spectroscopy showing sililar Kondo screening for $x = 0$ and $x = 0.5$ [61].

2.4.5 Application of magnetic field on $CeCu_2Ge_2$

The situation for the magnetic field as a tuning parameter for $CeCu_2Ge_2$ is less clear than for the tuning by pressure or the composition.

A neutron scattering investigation by [62] reported unusual temperature scaling of the magnetic excitations for $T < T_N$ at B_{qcp} = 8 T (B||[1$\bar{1}$0]). The unusual temperature scaling was interpreted as the presence of a quantum critical point at B_{qcp}. A phase diagram was drawn, where the zero field magnetic order persist to B_{qcp}, were the magnetic order is destroyed by quantum fluctuations resulting in a paramagnetic phase.

[34] derived a different phase diagram from bulk measurements (susceptibility, resistivity and specific heat) with B||[100] and B||[001]. Magnetic order persists to at least 14 T. The complete suppression of magnetic order was extrapolated to $B_c^{[100]}$ = 35 T and $B_c^{[001]}$ = 30 T. An additional peak in the specific heat appeared at 9 T (B||[100]). It was speculated that this peak corresponds to a metamagnetic transition. The peak roughly coincides with anomalies in the magnetization at 10.5 T for B||[100] and 7.8 T for B||[1$\bar{1}$0] [63]. Saturation of the magnetization was reported at H_{sat}^{basal} = 27 T with μ_s = 0.6-0.7 μ_B for B||[110] and B||[100], and at H_{sat}^{c} = 15.5 T with μ_s = 1.0 μ_B for B||[001]. This suggests a similar phase diagram for B||[110] and B||[100] but this is in contrast

to the phase diagram proposed by [62]. These results are summarized in Fig. 2.9 (top row).

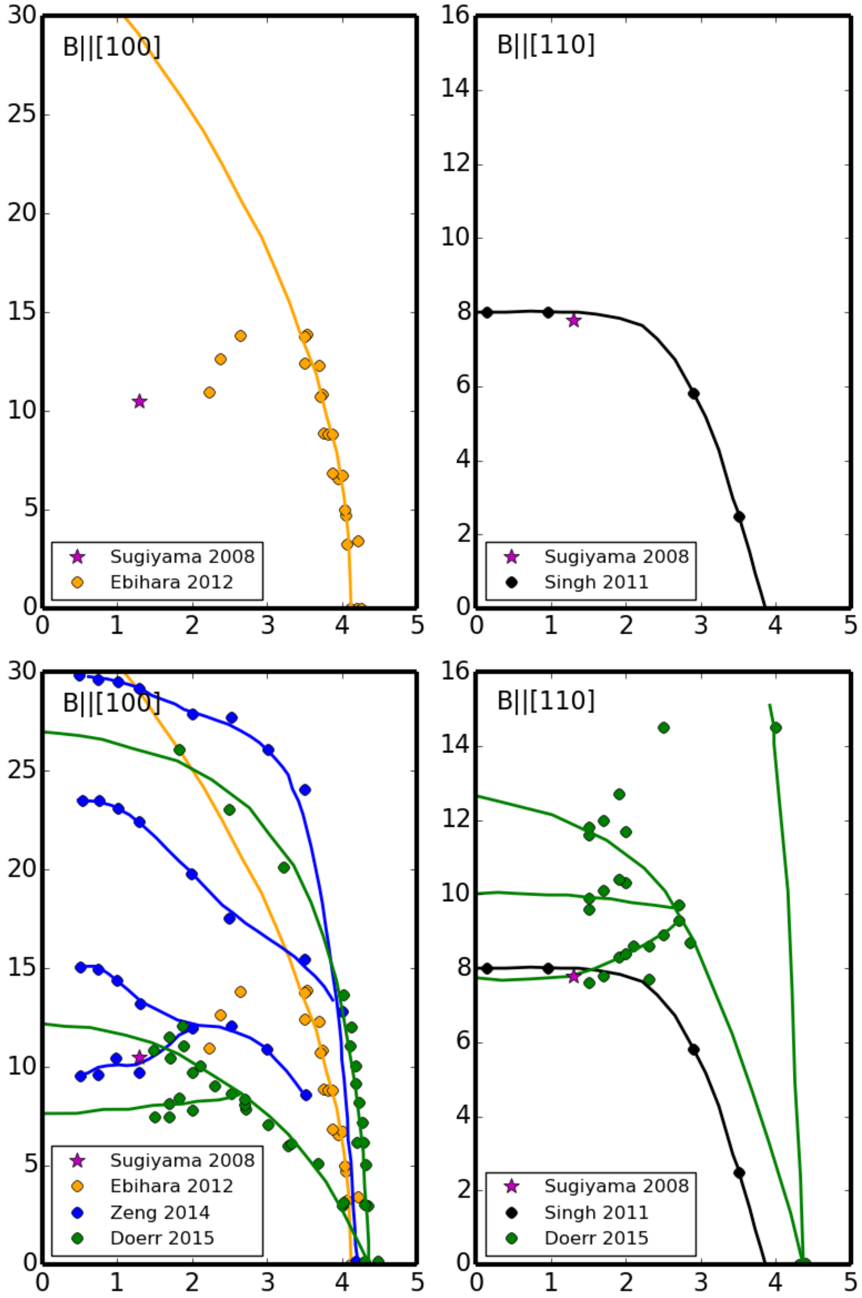

FIGURE 2.9: Summary of the published T-B phase diagrams [34; 62; 63; 64; 65] with B||[100] (left column) and B||[110] (right column). The top row shows the published data before the start of this work. The data points are based on magnetization (Sugiyama et al. [63], Doerr et al. [65]), resistivity (Ebihara et al. [34], Zeng et al. [64]), susceptibility (Ebihara et al.), specific heat (Ebihara et al.), magnetic torque (Zeng et al.), magnetostriction (Doerr et al.) and neutron scattering (Singh et al. [62]).

During the course of this thesis, further thermodynamic and transport data for B||[100] and B||[001] were published by [64] that hinted a quantum critical point at ≈ 30 T

(B||[100]) and a critical end point on the transition line of the zero field phase. Several not further specified metamagnetic transitions are reported for B||[100].

Magnetostriction and magnetization data were acquired for B||[100] and B||[110] by my collaborator (M. Doerr, CPfS) and subsequently published in [65]. The results suggest only small anisotropy for magnetic field in the basal plane. From tracking the features in the temperature or field dependence, several lines are recognized above 8 T. The nature of this features can not be determined unambiguously from the present data.

2.5 Current research on $CeCu_2(Si_{0.55}Ge_{0.45})_2$

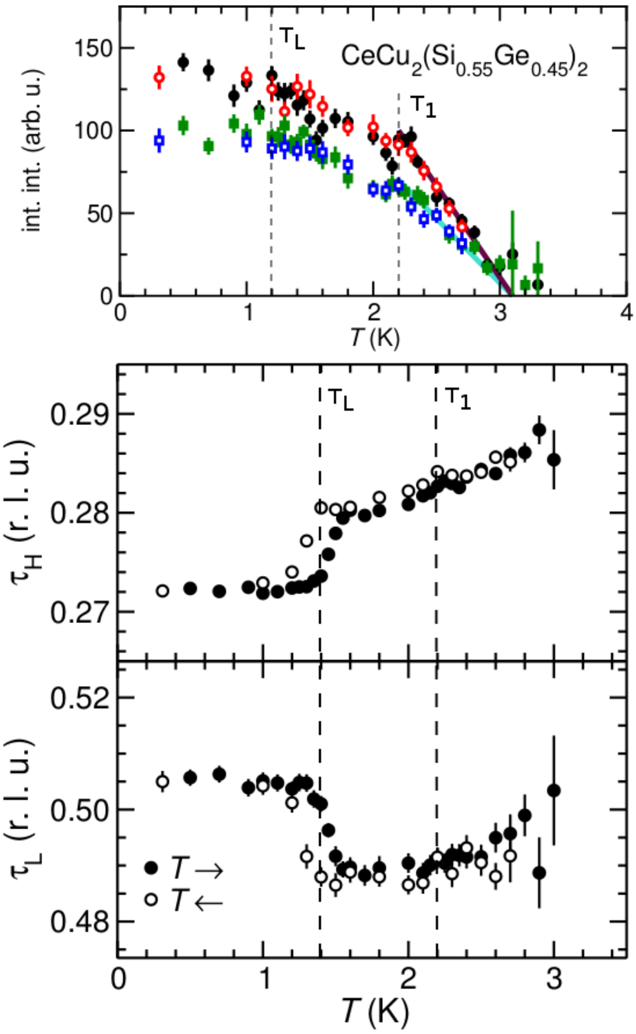

FIGURE 2.10: Top: temperature dependence of the integrated intensity of the magnetic Bragg peak. Center: temperature dependence of the h component of the propagation vector. Bottom: temperature dependence of the l component of the propagation vector. [66]

$CeCu_2(Si_{0.55}Ge_{0.45})_2$ was already investigated by neutron scattering in zero field [66]. Below T_N = 3.8 K, three cycloidal magnetic phases were identified: the high temperature antiferromagnetic (HAF), the medium temperature antiferromagnetic (MAF) and the low temperature antiferromagnetic (LAF) phase.

The propagation vector of HAF and MAF has a strong temperature dependence in the τ_h component of the propagation vector. The exact magnetic structure has not been identified, only the magnetic structure of the LAF phase has been solved yet: the magnetic moments of the Ce-atoms on the edges and in the center of the nuclear parent structure order in two counter rotating cycloids with the direction of moments perpendicular to [1$\bar{0}$ 8 5] [66]. The body centered symmetry of the parent structure is therefore broken for the magnetic ordering.

Specific heat measurements with B||[001] were priviousoly reported in [47]. It was found that transitions below T_N, except the lock-in transition, are suppressed at 8 T, while the effect on T_N is minimal. So far, no data for B||[1$\bar{1}$0] was reported.

2.6 Current research on $CeTIn_5$ (T = Rh, Ir, Co)

Besides the above discussed CeT_2X_2 (X = Si, Ge), successful growth of $CeTIn_5$ compounds with T = Rh, In and Co was reported in the early 2000s [67; 68; 69]. It crystallizes in the $HoCoGa_5$ structure, which is also tetragonal as CeT_2X_2 (X = Si, Ge) but not body centered (space group P4/mmm). The nuclear structure is shown in Fig. 2.11 and the Wyckoff positions listed in Tab. 2.2. The nuclear structure can be considered as a stacking along c of ($CeIn_3$) and (TIn_2) layers. Magnetic correlations develop in the ($CeIn_3$) layer, similar as in bulk $CeIn_3$ [70]. The intra layer coupling through the (TIn_2) layers is only weak, leading to quasi 2D magnetism [71].

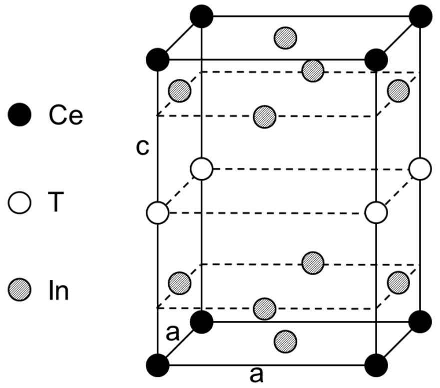

FIGURE 2.11: Nuclear structure of $CeTIn_5$ ($HoCoGa_5$ type, space group P4/mmm). T = Rh, In, Co.

atom	multiplicity	Wyckoff letter	coordinates
Ce	1	a	(0,0,0)
T	1	b	(0,0,1/2)
In1	1	c	(1/2 1/2 0)
In2	4	i	(0 1/2 z) (1/2 0 z) (0 1/2 -z) (1/2 0 -z)

TABLE 2.2: Wyckoff positions in $CeTIn_5$ ($HoCoGa_5$ type, space group I4/mmm). T = Rh, In, Co.

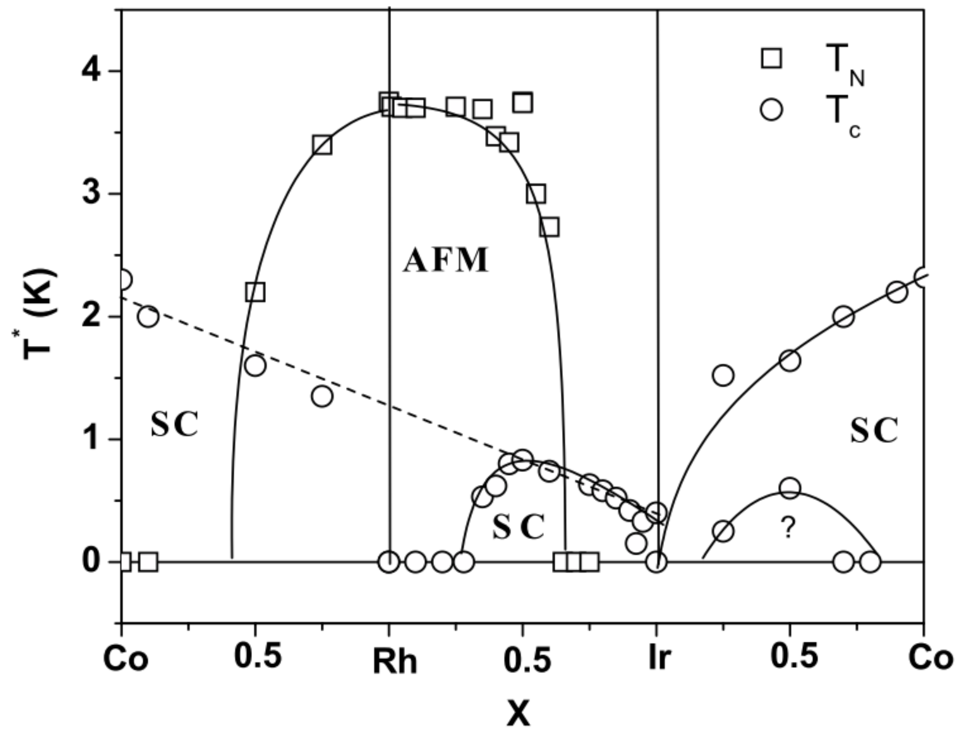

FIGURE 2.12: Peudo binary phase diagram for mixtures of $CeTIn_5$ (T = Rh, In, Co) [72]. An impurity phase corresponding to the dome marked by “?” can not be ruled out.

A pseudo binary phase diagram for mixtures Rh/In/Co was derived by [73] (Fig. 2.12). Starting from the antiferromagnetic ordered phase of $CeRhIn_5$, Ir substitution leads to suppression of the magnetic order and a superconducting dome is present. A broad region of coexistence exists [73], pointing towards magnetic fluctuation driven superconductivity. This would be consistent with a pressure induced quantum critical point in $CeRhIn_5$ [74]. With high Ir concentration, close to pure $CeIrIn_5$, the superconducting phase splits in two separated domes, whose separation can be further tuned under pressure [75]. $Ce(Co/Rh)In_5$ and $Ce(Co/Ir)In_5$ are less well investigated. The coexistence of magnetic order and superconductivity in $Ce(Co/Rh)In_5$ points also towards magnetic fluctuation driven superconductivity, even though one would expect the maximum of T_c closer to the suppression of magnetic order. Paramagnon excitations in

$CeCoIn_5$, which open up a gap in the superconducting state, were discovered in the normal state. This behavior is consistent with such a magnetic fluctuations scenario [76]. For $CeIrIn_5$, the situation is ambiguous. On one hand, the temperature dependence of the dynamic susceptibility, magnetic correlation length and spin damping were reported as consistent with magnetic quantum fluctuation driven superconductivity [77]. On the other hand, magnetic fluctuations are suppressed under pressure while at the same time T_c is increased [78]. It has been speculated, that in fact $CeIrIn_5$ is tuned away from a antiferromagnetic quantum critical point with pressure and that the superconductivity is connected to valence fluctuations [79]. This view is also supported by the similarity of the phase diagram of $CeCu_2(Si_{1-x}Ge_x)_2$ series. The superconductivity of $Ce(Co/Ir)In_5$ might be an equivalent of the high pressure superconductivity in $CeCu_2Si_2$, but here it is already accessible at ambient pressure, enabling inelastic neutron scattering experiments.

Chapter 3

Experimental Methods

3.1 Material preparation

3.1.1 $CeCu_2Ge_2$ and $CeCu_2(Si_{0.55}Ge_{0.45})_2$

For the measurements on $CeCu_2Ge_2$ and $CeCu_2(Si_{0.55}Ge_{0.45})_2$, single crystal samples prepared and characterized by M. Deppe (CPfS), were used. The samples were grown from Cu self flux using a modified Bridgman technique described in [47]. Small pieces from the same growth batch as the samples for neutron scattering were characterized by single crystal X-ray diffraction. The nuclear structure and lattice constant are in agreement with the previously published data. The Ge content in $CeCu_2(Si_{0.55}Ge_{0.45})_2$ was determined by EDX-analysis and is match with the estimation from the lattice constants using Vegard's law.

An overview of the two used $CeCu_2Ge_2$ and $CeCu_2(Si_{0.55}Ge_{0.45})_2$ samples is given in Tab. 3.1. Both samples were used in previous neutron scattering studies. The single crystal character of the samples for neutron neutron scattering was confirmed by X-ray Laue images. X-ray Laue imaging was further used to determine the orientation. An appropriate side of the crystals was cut and polished before gluing to a copper sample holder. For this purpose, the two component epoxy encapsulant STYCAST 2850 FT with 24LV curing agent was used.

material	mass (g)	volume (mm^3)	used in
$CeCu_2Ge_2$	3	$\approx$ 5x5x12	[38]
$CeCu_2(Si_{0.55}Ge_{0.45})_2$	0.5	$\approx$ 3x4x5	[26; 28; 66]

TABLE 3.1: Overview of the $CeCu_2(Si_{1-x}Ge_x)_2$ samples used for neutron scattering experiments.

For the $CeCu_2Ge_2$ sample, signs of an impurity phase were noticed: intensity peaks form nuclear scattering was present at the (-1 -1 1.4) and (0 0 2.78). As the H components of the peaks coincide with the nuclear structure of $CeCu_2Ge_2$, the impurity phase has also tetragonal symmetry with similar *a* lattice constant. Assuming c = 14.8 Å for the impurity phase, these intensities correspond to the (112) and (004) Bragg peaks. Such lattice constants with a similar tetragonal structure have been reported for $CeGe_{2-x}$ [80; 81]. Additionally, several grains in the sample were noticed. However, judging from the observed intensities the volume of impurity phase and of the grains is $\approx$ 200 times smaller then the bulk volume. The only exception is a grain that is rotated $\approx 1^\circ$ away from the bulk volume.

3.1.2 $CeCo_xIr_{1-x}In_5$

For the investigation of $CeCo_xIr_{1-x}In_5$, no samples were available for examination in this work. In addition, no growth recipe has been published yet. Hence, the growth method for $CeCo_xIr_{1-x}In_5$ samples had to be developed from scratch.

A powerful, yet simple method to grow high quality single crystal is the self flux growth. Excellent results were already obtained on the Ce115 family using this method [82; 83; 67; 68]. As the sample growth is not a mayor part of this thesis, only the principle of the growth and characterization techniques are described. The proceeding depicted here was done in close analogy and with the same equipment, i.e. in the same laboratory, as in [84].

The principle of flux growth is to solve an element A in the liquid of an other element B (the flux) below the melting point of A. This can be easily understood from the every day example of solving cooking salt in water. In case of the self flux, the flux metal is part of the later desired compound. The principle of growth process is depicted in the binary phase shown in Fig. 3.1. A is one or more elements in a fixed ratio, B is a single element (the flux). $A_{1-x}B_x$ is the desired compound. From the phase diagram one can see that a mixture $A_{1-x}B_x$ is incongruently melting, i.e. B becomes liquid first. Simply melting and cooling a stoichiometric $A_{1-x}B_x$ mixture would therefore result in a multiphase product with large amount of A, but not in the desired $A_{1-x}B_x$ crystals. To avoid this, excess B is added to avoid crystallization of A upon cooling. The amount of B should be small enough to avoid the also undesired crystallization of B. The growth procedure then follows these steps (the numbers correspond to the markings in Fig. 3.1):

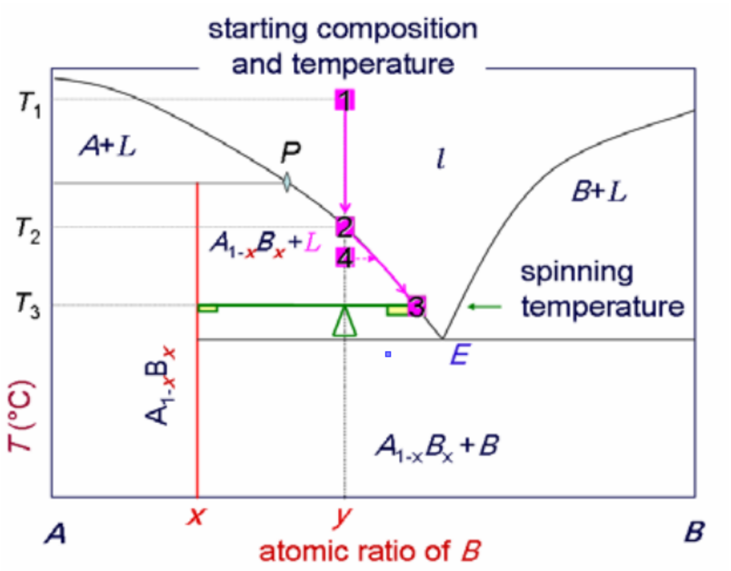

FIGURE 3.1: Schematic temperature - composition phase diagram for the arbitrary elements *A* and *B* [84]. The arrows describes a possible growth process (see text). The desired composition is marked with *x* and the starting composition with *y*. L is the saturated solution, coexisting with the indicated crystallized phase and l is the completely liquid (unsaturated) part of the phase diagram.

- $A_{1-y}B_y$ $(y > x)$ is melted by heating to (1)
- The melt is slowly cooled down. Growth of the $A_{1-x}B_x$ starts at (2)
- Further cooling to (4). The remaining liquid becomes more *B*-rich as more *A* than *B* is consumed by the $A_{1-x}B_x$.
- The remaining B is decanted at (3). The growth process finishes here.

To grow $\mathrm{CeCo}_x\mathrm{Ir}_{1-x}\mathrm{In}_5$, one chooses $A = \mathrm{CeCo}_x\mathrm{Ir}_{1-x}$ and $B = \mathrm{In}$.

The parameters for the initial growth attempt are described here. The parameters were then altered to find the optimized growth parameters. Starting materials in the desired ration with excess In, e.g. 1:0.5:0.5:25 (Ce:Co:Ir:In) (purity $>$ 99.99 %) are placed in an Al_2O_3 crucible (diameter 13 mm, hight 25 mm). The crucible is sealed in a quartz ampule with a protective argon atmosphere and quartz wool end cap, before it is put to the furnace. The temperature profile starts with heating to 1000°C, which is maintained for 24 hours. The melt is then cooled to 500°C with a cooling rate of 3°C/h. Afterwards, the excess In is decanted and spun off in a centrifuge. The ampule is then cooled to room temperature in water bath and subsequently cracked open. The crystals grown were removed from the crucible using tweezers, but also in some cases the crucible had to be cracked in a screw clamp. If In flux remained on the crystals, hydrochloric acid was used to remove it.

Well defined crystals were selected and polished in such way, that the side exposing the different layers could be investigated by scanning electron microscope (SEM) and dispersive X-ray spectroscopy (EDX). Selected crystals were investigated by X-ray diffraction. Furthermore, the specific heat of one sample was measured using a double relaxation method described in [85].

3.2 Neutron scattering

The physical properties of the neutron are summarized in Tab. 3.2.

charge	0
spin	$\frac{1}{2}$
mass	939,565 MeV/c^2
lifetime	882 s
magnetic moment μ_n	-0.96623 $\cdot$ $10^{-}26$ $\frac{\mathrm{J}}{\mathrm{T}}$
gyromagnetic ratio γ_n	-1.83247 $\cdot$ 10^8 $\frac{1}{\mathrm{sT}}$
Landé-factor g_n	3.82609

TABLE 3.2: Physical properties of the neutron [86]

Since the neutron carries a non zero spin, it possesses a magnetic moment. Thus, interaction with matter is possible via the magnetic dipole interaction. The potential associated with this interaction is given as $V = \vec{\mu_n} \cdot \vec{B}$, where $\vec{B} = \vec{B_S} + \vec{B_L}$ is the magnetic flux density generated by the spins ($\vec{B_S}$) and orbital motions ($\vec{B_L}$) of the electrons of an atom. The magnetic moment of an electron with spin $\vec{s}$ and position $\vec{R}$ relative to the nucleus is $\mu_e = -2\mu_B\vec{s}$ and therefore

$$\vec{B_S} = -\frac{2\mu_0\mu_B}{4\pi}\vec{\nabla} \times \frac{\vec{s} \times \hat{R}}{R^2} \tag{3.1}$$

$\vec{B_L}$ can be derived from Biot-Sarvat law

$$\vec{B_L} = -\frac{\mu_0 e}{4\pi R^2}\vec{v} \times \hat{R} \tag{3.2}$$

where $\vec{v}$ is the velocity of the electron.

Besides the magnetic dipole interaction, also the strong interaction with the nucleus is relevant for scattering [87]. In the Born approximation, the neutron-nucleus interaction can be expressed using Fermi's pseudo-potential

$$V = \frac{2\pi\hbar^2}{m_\mathrm{n}} b \tag{3.3}$$

where b is the scattering length associated with the respective atom.

The energy E of neutrons coming from the neutron source is $E < 1000$ meV, hence non relativistic description of the neutrons is applicable. The neutron energy may be expressed using $E = \frac{p^2}{2m_\mathrm{n}}$. Using $\vec{p} = \hbar\vec{k}$ and the de Broglie wavelength $\lambda = \frac{2\pi}{|\vec{k}|}$, the neutron energy is given as

$$E = \frac{p^2}{2m_\mathrm{n}} = \frac{\hbar^2 k^2}{2m_\mathrm{n}} = \frac{h^2}{2m_\mathrm{n}\lambda} \tag{3.4}$$

The scattering of neutrons from a sample is described using scattering cross-sections. In an experiment, the intensity I of neutrons scattered in a solid angle $d\Omega$ is measured with a detector. I can be expressed using the incident flux Φ and the double differential cross-section:

$$I = \Phi \int\int \frac{d^2\sigma}{dEd\Omega} dEd\Omega \tag{3.5}$$

The limits of integration are given by the instrument used, for example a diffractometer would integrate over all energies, while a triple axis spectrometer would only integrate over a narrow range of the energy transfer dE.

The double different cross-section is given in its general form by Fermi's golden rule [88]:

$$\frac{d^2\sigma}{dEd\Omega} = \frac{k_\mathrm{f}}{k_\mathrm{i}} \left(\frac{m_\mathrm{n}}{2\pi\hbar}\right)^2 \left|\langle \vec{k}_\mathrm{f}\lambda_\mathrm{f}|V|\vec{k}_\mathrm{i}\lambda_\mathrm{i}\rangle\right|^2 \delta(E + E_\mathrm{i} - E_\mathrm{f}) \tag{3.6}$$

$\vec{k}_\mathrm{f}$ ($\vec{k}_\mathrm{i}$) denotes the final (initial) wave vector of the neutron. The final (initial) state of the scattering target, i.e. the sample, is denoted by λ_f (λ_i).

In the experiments performed in this work, a sample with a periodic crystal lattice is placed in a well defined incident beam $|\vec{k}_\mathrm{i}|$. At any atom in the sample, neutrons are scattered. With the de Broglie wave character of the neutron, any atom can be imagined as an emitter of a neutron wave $|\vec{k}_\mathrm{f}|$. In a crystal lattice, interference of the waves of scattered neutrons from all atoms then leads to unique scattering patterns associated with the sample. The schematic setup of such an experiment is shown in Fig 3.2 (a). The incident beam $|\vec{k}_\mathrm{i}|$ is scattered by the sample in direction of the final wave vector $|\vec{k}_\mathrm{f}|$. The scattering angle 2θ is the angle between $|\vec{k}_\mathrm{i}|$ and $|\vec{k}_\mathrm{f}|$. ω is the sample rotation. $\vec{Q}$ is the scattering vector defined as

$$\vec{Q} = \vec{k}_\mathrm{i} - \vec{k}_\mathrm{f} \tag{3.7}$$

The scattering condition for the elastic scattering case, i.e. $|\vec{k}_\mathrm{i}| = |\vec{k}_\mathrm{f}|$, is given by the Laue condition $\vec{Q} = \vec{G}$, where $\vec{G}$ is the reciprocal lattice vector. In Fig. 3.2 (b), beam 1

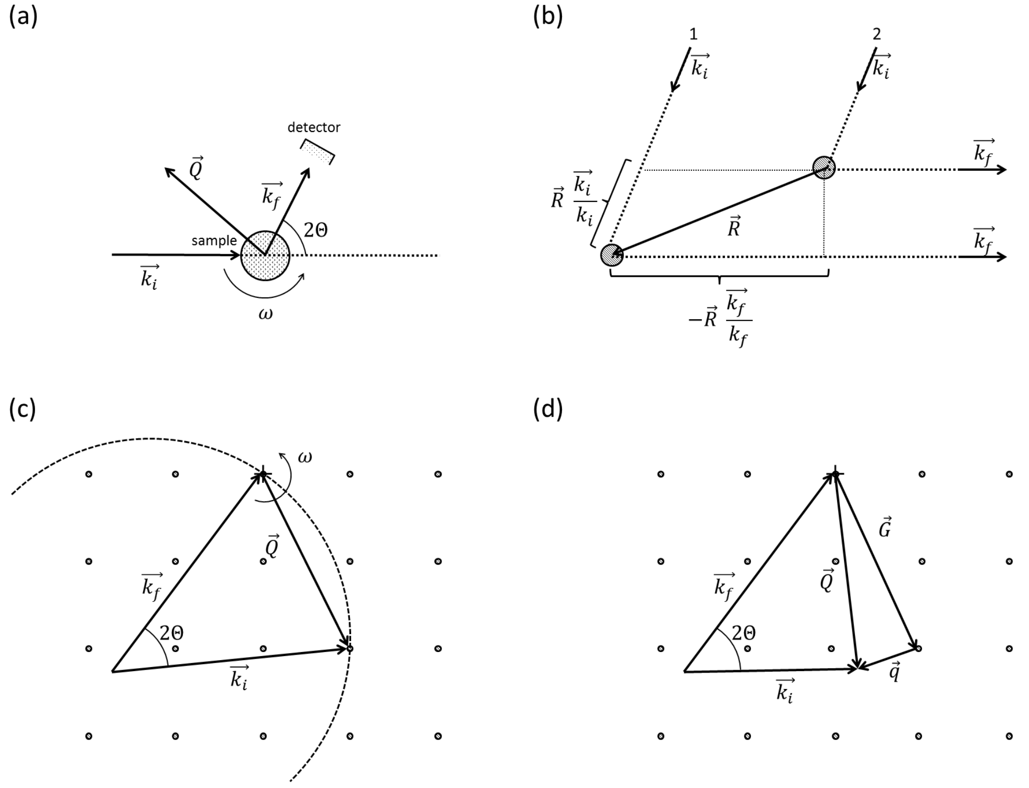

FIGURE 3.2: (a) schematics of a scattering experiment (b) Laue condition (c) scattering triangle in the elastic case (d) scattering triangle in the inelastic case (neutron looses energy)

has to travel an additional distance Δx:

$$\Delta x = \vec{R}\frac{\vec{k}_\mathrm{i}}{|\vec{k}_\mathrm{i}|} - \vec{R}\frac{\vec{k}_\mathrm{f}}{|\vec{k}_\mathrm{f}|} \tag{3.8}$$

For constructive interference, $\Delta x = \lambda n$ ($n \in \mathbb{N}$) has to be fulfilled. With $|\vec{k}_\mathrm{i}| = |\vec{k}_\mathrm{f}| = \frac{2\pi}{\lambda}$ this yields

$$\vec{R} \cdot \left(\vec{k}_\mathrm{i} - \vec{k}_\mathrm{f}\right) = 2\pi n \tag{3.9}$$

which is equivalent to

$$e^{i\vec{R}\cdot\left(\vec{k}_\mathrm{i} - \vec{k}_\mathrm{f}\right)} = 1 \tag{3.10}$$

Thus, the Laue condition $\vec{Q} = \vec{G}$ gives constructive interference. This can be illustrated with the scattering triangle in reciprocal space as shown in Fig. 3.2 (c). In the elastic case with $|\vec{k}| = |\vec{k}_\mathrm{i}| = |\vec{k}_\mathrm{f}|$, the origin of the coordinate system and $\vec{Q}$ both lie on a circle with radius $|\vec{k}|$, called Ewald's sphere. From this, one can also see, that the fulfillment of the Laue condition depends also on the sample rotation in the case of a single crystal sample as drawn here. Additional to the elastic case discussed above, energy can be also transfered to or gained from the sample. In this case $|\vec{k}_\mathrm{i}| \neq |\vec{k}_\mathrm{f}|$ and the Laue condition is replaced by $\vec{Q} = \vec{G} + \vec{q}$, which means an additional impulse $\vec{q}$ is transfered to (or from) the sample. The energy transfer can be easily calculated using Eq. 3.4:

$$\Delta E = E_\mathrm{i} - E_\mathrm{f} = \frac{\hbar^2}{2m_\mathrm{n}}\left(\vec{k}_\mathrm{i}^2 - \vec{k}_\mathrm{f}^2\right) \tag{3.11}$$

The corresponding scattering triangle in the case of neutron energy loss is shown in Fig. 3.2 (d).

In case of elastic scattering, it is convenient to use the well known Bragg's law, which is equivalent to the above Laue condition

$$n\lambda = 2d\sin(\theta) \tag{3.12}$$

as a condition for constructive interference, where d is the corresponding lattice spacing.

3.3 $\mathrm{CeCu_2Ge_2}$

3.3.1 Determination of magnetic structures

In order to determine the magnetic structures by neutron diffraction for the compound with known magnetic parent structure the following steps are carried out:

Step 1: indexing of the magnetic satellites

Step 2: diffraction experiment with unpolarized neutrons

Step 3: finding a model for the magnetic structure via representation analysis

Step 4: refinement of the magnetic structure

In this work, the diffraction pattern, i.e. the intensities of the magnetic satellites, was obtained with unpolarized as well as polarized neutrons. The refinement was limited to the unpolarized dataset, since the capability of existing refinement software is still limited for polarized neutrons.

Step 1: indexing of the magnetic satellites

As for $\mathrm{CeCu_2(Si_{0.55}Ge_{0.45})_2}$, possible lifting of the body centered symmetry may result in overlapping of the $(H \pm \tau_\mathrm{h}\ H \pm \tau_\mathrm{h}\ 2 + \tau_\mathrm{l})$ and $(H \pm \tau_\mathrm{h}\ H \pm \tau_\mathrm{h}\ 2 - \tau_\mathrm{l})$ magnetic satellites.

The resolution of diffractometers ($\Delta q \approx 0.02$ Å^{-1}) might be insufficient to distinguish between the two satellites. Instead, the cold triple axis spectrometer IN12 was used, which has an resolution of $\Delta q \approx 0.006$ Å^{-1} with the used setup.

instrument/facility	IN12/ILL
λ (Å)	5.2
scattering plane	[110]/[001]
T (K)	0.05
B (T)	0
data provided by	A. Schneidewind (JCNS)

TABLE 3.3: Information for the diffraction experiments with unpolarized neutrons.

In the [110]/[001] scattering plane, an area with H = 0.26 ... 0.31 and L = 1.40 ... 1.56 was mapped.

Step 2: diffraction experiment with unpolarized neutrons

For periodic arrangements of atoms, such as crystalline samples used in this work, the nuclear scattering cross-section becomes [89]:

$$\frac{d\sigma_{\mathrm{N}}}{d\Omega} = \frac{(2\pi)^3}{V}\mathcal{N}\sum_{H}\left|F_{\mathrm{N}}\left(\vec{Q}\right)\right|^2 \delta\left(\vec{Q}-\vec{G}\right) \tag{3.13}$$

$\mathcal{N}$ is the number of nuclear unit cells, V the volume of one nuclear unit cell and $\vec{G}$ is the reciprocal lattice vector. F_{N} is the nuclear structure factor [89]

$$F_{\mathrm{N}}\left(\vec{Q}\right) = \sum_{\nu} b_{\nu} e^{i\vec{Q}\cdot\vec{r}_{\nu}} \tag{3.14}$$

It can be interpreted as an periodic arrangement of scatterers with scattering length b, which is Fourier transformed to the reciprocal space.

In a similar way, the magnetic moments of atoms are arranged periodically if the sample possesses magnetic order. The arrangement of magnetic moments on the nuclear lattice are described by

$$\vec{\mu}_{n\nu} = \sum_{\vec{\tau}} \vec{m}_{\nu,\vec{\tau}} e^{-i\vec{\tau}\cdot\vec{r}_n} \tag{3.15}$$

where $\vec{\tau}$ is the propagation vector, which is perpendicular to the ferromagnetic planes of the magnetic structure. The crossection for magnetic scattering can be similarly expressed as for nuclear scattering [89]:

	AF1 magnetic structure	AF2 magnetic structure
instrument/facility	D23/ILL	E4/HZB
λ (Å)	2.4	2.4
scattering plane	[110]/[001]	[110]/[001]
number of peaks	116	10
T (K)	2	0.3
B (T)	0	11
B direction	-	$[1\bar{1}0]$
experimental team	P. Geselbracht (TUM), W. Simeth (TUM)	P. Geselbracht (TUM), A. Schneidewind (JCNS)
local contact	K. Schmalzl (JCNS)	K. Prokeš (HZB), F. Yokaichiya (HZB)

TABLE 3.4: Information of the diffraction experiments with unpolarized neutrons.

$$\frac{d\sigma_{\mathrm{M}}}{d\Omega} = \frac{(2\pi)^3}{V}\mathcal{N}\sum_{H}\sum_{\vec{\tau}}\left|\vec{F}_{\mathrm{M}\perp}\left(\vec{Q}\right)\right|^2 \delta\left(\vec{Q}-\vec{G}-\vec{\tau}\right) \tag{3.16}$$

where $\vec{F}_{\mathrm{M}\perp}$ is the perpendicular component of the magnetic structure factor[1] $\vec{F}_{\mathrm{M}}$ to $\vec{Q}$. It is given as [89]

$$\vec{F}_{\mathrm{M}}\left(\vec{Q}=\vec{G}+\vec{\tau}\right) = p\sum_{\nu} f_{\nu}\left(\vec{Q}\right)\vec{m}_{\nu,\vec{\tau}}e^{i\vec{Q}\cdot\vec{r}_{\nu}} \tag{3.17}$$

very similar in its form to the nuclear structure factor, but the scattering length is replaced by the magnetic form factor and the fourier components $\vec{m}_{\nu,\vec{\tau}}$ that describe the magnetic structure. As $\vec{m}_{\nu,\vec{\tau}}$ is a vector, hence also $\vec{F}_{\mathrm{M}}$ becomes a vector.

The experimental parameters for the diffraction experiments to determine the magnetic structure of the zero field AF1 phase and the field induced AF2 phase are shown in Tab. 3.4.

The D23 diffractometer uses a single detector. Rocking scans, i.e. scans of the sample rotation, over the magnetic satellites were performed. The scans were fitted using two Gaussians and a constant background. The additional peak which is present corresponds to a grain rotated by $\approx 1°$. The integrated intensity was derived only from the main peak, i.e. the shaded area in Fig. 3.3.

On the E4 diffractometer, an area detector was used (distance to sample 795 mm; hight and width 200 mm). The detector images were corrected for the detector efficiency.

---

[1] Note than in literature some times only the term “structure factor” is used, which refers to the nuclear structure factor. In these cases, if also magnetic scattering is discussed, it is directly refereed to Eq. 3.17 inserted in Eq. 3.16 or an equivalent formulation. To avoid confusion, in this work, the term “nuclear structure factor” or “magnetic structure factor” respectively is used to distinguish.

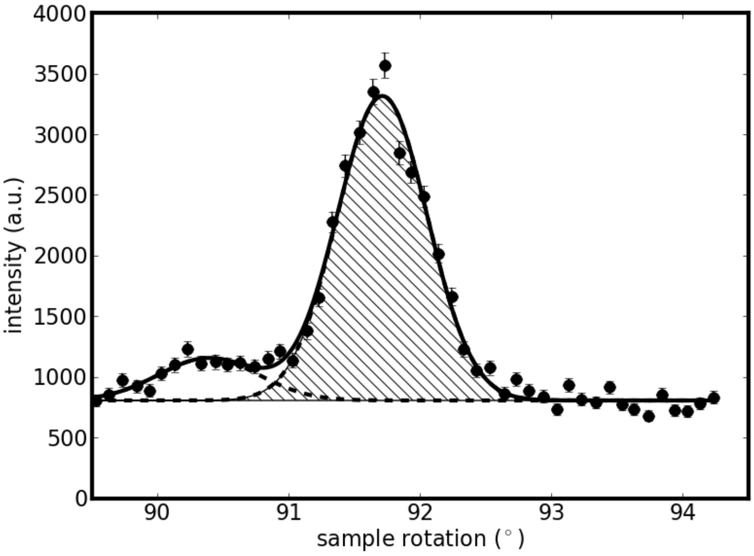

FIGURE 3.3: Representative ((1.284 1.285 4.544) magnetic satellite) fit of the rocking scan to obtain the integrated intensity (shaded area).

Rocking scans with stepsize $\Delta\omega$ = 0.2° were performed and then summed up. The intensity in an appropriate rectangular area around the peak was then summed (see Fig. 3.3). The scattering angle 2Θ as well as the lifting angle ν were calculated from the detector distance and size.

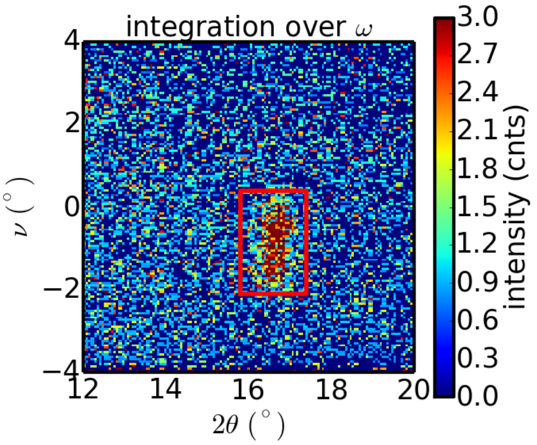

FIGURE 3.4: Obtaining the integrated intensity at E4: maps for one ω are summed, afterwards the intensity in the red box is summed.

Before relating the integrated intensities to the magnetic structure factor, the Lorentz correction [90]

$$I \propto \frac{|F|^2}{\sin(2\theta)} \tag{3.18}$$

was applied on the data of both experiments. It takes into account the 2θ dependent amount of reciprocal space that is crossed in the rocking scans. No correction for beam polarization or absorption was applied. The ordered moment was derived from comparing the intensities of the magnetic satellites to the nuclear Bragg peaks.

Step 3: finding a model for the magnetic structure via representation analysis

Starting with the general expression for a magnetic moment at atom j (Eq. 3.15), one has to find all Fourier components $m_{j,\vec{\tau}}$ to determine the magnetic structure. In general, m_j is a complex quantity. In case of one propagation vector and one magnetic site, still six free parameters (real and complex value for all three space directions) remain. These free parameters can be significantly limited by analyzing the symmetry. Within the Landau theory of second order phase transitions, the presence of magnetic order is associated with lowering of the symmetry of the nuclear parent structure. However, a major number of symmetries may remain in place. The remaining symmetry operations must leave the magnetic structure invariant. The fundamental approach of a representation analysis is to find these remaining symmetries [91; 92; 93].

The resulting model will have a significantly lower number of free parameters that need to be refined. Strictly speaking, the results of a representation analysis are only valid if the phase transition is second order.

Input parameters for the representation analysis are the nuclear parent structure, i.e. symmetry and Wyckoff positions, and the propagation vector. The nuclear structure of $CeCu_2Ge_2$ is known from [21; 35] and the propagation vector can be straightforwardly derived from the indexing of the magnetic satellites. It is assumed only the Ce ion is carrying a magnetic moment.

As the propagation vector indicates an incommensurate structure, the symmetry analysis is based on the irreproducible representations of the propagation vector group [94]. Tabulation [95] of the irreducible representations of the I4/mmm space group were accessed via the ISODISTORT software [96].

Step 4: refinement of magnetic structures

As the structure factor in both Eq. 3.13 and Eq. 3.16 are squared up, there is no way of just “back transforming” the measured intensities and obtain the nuclear or magnetic structure. Instead a model has to be proposed. The free parameters of the model are refined to fit the measured intensities. This is done using the JANA2006 [97] software suit.

As quality indicator of the fit, the “R-value” [98] is used. It is defined as

$$R = \frac{\sum ||F_{\text{obs}}| - |F_{\text{calc}}||}{\sum |F_{\text{obs}}|} \tag{3.19}$$

F_{obs} is the observed structure factor and F_{calc} is calculated from the model.

3.3.2 Diffraction experiment with polarized neutrons

An additional way to get information on magnetic structure structure is the application of a polarized neutron beam. It can either be used to separate nuclear and magnetic scattering or to yield additional information on the direction of $\vec{F}_M$. This is especially useful in cases were the squaring in Eq. 3.16 makes the distinction between certain magnetic structures impossible. Polarization analysis can also be used for inelastic scattering very similar as for elastic scattering [99]. In this work here, it has been used only for elastic scattering, so the depiction will be limited to the elastic case only.

In case of an polarized beam Eq. 3.6 has to be modified

$$\left|\langle\vec{k}_f\lambda_f|V|\vec{k}_i\lambda_i\rangle\right|^2 \longrightarrow \sum_{\sigma_i\sigma_f} p_\sigma \left|\langle\sigma_f|\,\langle\vec{k}_f\lambda_f|V|\vec{k}_i\lambda_i\rangle\,|\sigma_i\rangle\right|^2 \tag{3.20}$$

where σ represents the spin state and p_σ the probability that the neutron is in the incident state σ. The resulting expression was evaluated by several authors [100; 101; 102; 103; 104] using the theoretical framework given in [105]. For clarity, only the results for the experimental setup used here will be given.

A diffraction experiment with polarized neutrons was performed on the time-of-flight spectrometer DNS without using the chopper (Fig. 3.5). The aim of the experiment was twofold: firstly, the determination of the direction of the magnetic form factor and secondly to measure the temperature dependence of the magnetic satellites. The experimental parameters are summarized in Tab. 3.5. The polarization P of the incident beam is given as

$$P = \frac{F-1}{F+1} \tag{3.21}$$

where $F = \frac{I_{parasitic}}{I_{non-parasitic}}$ is the flipping ratio, i.e. the ratio of the parasitic and non-parasitic intensities. The parasitic and non-parasitic intensity was measured on the (004) nuclear peak.

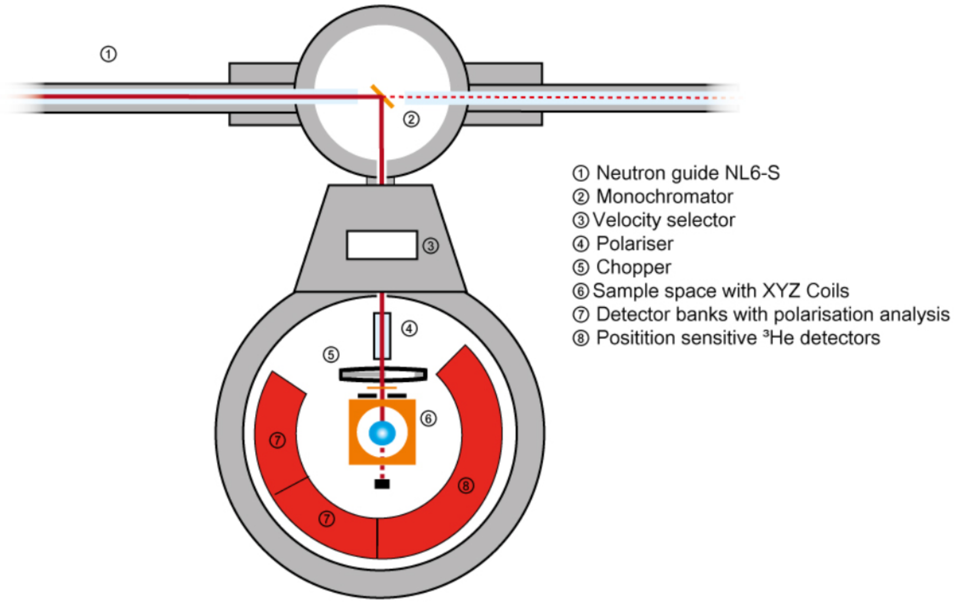

FIGURE 3.5: Schematic drawing of the diffuse scattering neutron time-of-flight spectrometer DNS [106] at Maier-Leibnitz Zentrum.

instrument/facility	DNS/MLZ
λ (Å)	4.2
polarization	96 %
scattering plane	[110]/[001]
T (K)	0.6 - 6
experimental team	P. Geselbracht (TUM)
local contact	K. Nemkovski (JCNS)

TABLE 3.5: Information of the diffraction experiment with polarized neutrons.

By mapping around the (τ_h τ_h 2+τ_l) and (τ_h τ_h 2-τ_l) magnetic satellites with polarization approximately along the scattering vector $\vec{Q}$ in the spin-flip channel, the temperature dependence upon cooling as well as upon heating was measured.

These maps cover also the (004) position, that was used for normalization of the intensity as well as to rule out anomalies in the nuclear structure. The peak position and integrated intensity were obtained from two-dimensional Gaussian fits. First, it was measured upon heating then upon cooling. Between both measurements, the sample was heated to $T \geq 6$ K, well above T_N.

To determine the direction of the magnetic form factor, elastic intensity maps have been obtained using the detector banks with polarization analysis in spin-flip (sf) as well as in non spin-flip (nsf) mode for x-polarization at 6 K, 2.6 K, 2 K and 0.6 K. For z-polarization, maps at 3 K and 0.6 K were obtained.

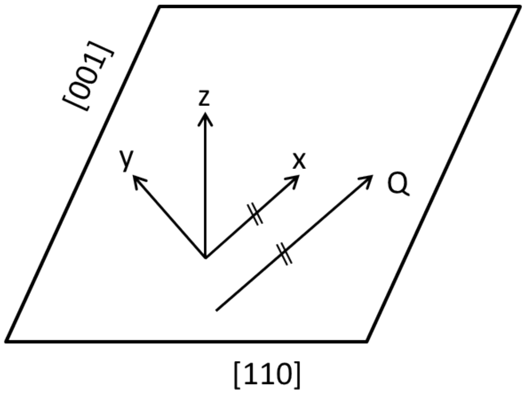

$x \parallel Q\,; \quad x \in scattering\ plane$
$y \perp Q\,; \quad y \in scattering\ plane$
$z \perp scattering\ plane$

FIGURE 3.6: The x,y,z-coordinate system from DNS with respect to the [110]/[001] scattering plane.

DNS uses the xyz-polarization analysis established in [107; 108]. The polarization of the incident beam can be chosen along the directions $\vec{x}$, $\vec{y}$ or $\vec{z}$. As it is defined relative to the scattering vector $\vec{Q}$ and the used scattering plane, it has to be transformed to a sample related coordinate system to allow a meaningful interpretation. By definition, $\vec{x}$ is along $\vec{Q}$, $\vec{y}$ is perpendicular to $\vec{Q}$ and in the scattering plane and $\vec{z}$ is perpendicular to the scattering plane (see Fig. 3.6).

The scattering intensities are given as [99]:

$$I_x^{\mathrm{sf}} = I_{\mathrm{mag}}^{z} + I_{\mathrm{mag}}^{y} + \frac{2}{3} I_{\mathrm{inc}}^{\mathrm{mag}} \tag{3.22}$$

$$I_x^{\mathrm{nsf}} = I_{\mathrm{nuc}} + \frac{1}{3} I_{\mathrm{inc}}^{\mathrm{mag}} \tag{3.23}$$

$$I_y^{\mathrm{sf}} = I_{\mathrm{mag}}^{z} + \frac{2}{3} I_{\mathrm{inc}}^{\mathrm{spin}} \tag{3.24}$$

$$I_y^{\mathrm{nsf}} = I_{\mathrm{nuc}} + I_{\mathrm{mag}}^{y} + \frac{1}{3} I_{\mathrm{inc}}^{\mathrm{mag}} \tag{3.25}$$

$$I_z^{\mathrm{sf}} = I_{\mathrm{mag}}^{y} + \frac{2}{3} I_{\mathrm{inc}}^{\mathrm{mag}} \tag{3.26}$$

$$I_z^{\mathrm{nsf}} = I_{\mathrm{nuc}} + I_{\mathrm{mag}}^{z} + \frac{1}{3} I_{\mathrm{inc}}^{\mathrm{mag}} \tag{3.27}$$

I_mag corresponds to the component of the magnetic structure factor (Eq. 3.17) in the indicated direction ($\vec{x}$, $\vec{y}$ or $\vec{z}$) and $I_\mathrm{inc}^\mathrm{mag}$ to incoherent magnetic scattering.

Note that due to the detector banks, the polarization along $\vec{Q}$ is only an approximation that can not be realized for all detectors at the same time. The same is true for $\vec{y}$, but polarization along $\vec{z}$ is realized for all detectors.

As the [110]/[001] scattering plane was used in the experiment, $\vec{z}$ || $[1\bar{1}0]$ is always. No measurement with polarization in $\vec{y}$ direction was made, therefore I_y^sf and I_y^sf can be omitted. The above equations can be rewritten as:

$$I_x^\mathrm{sf} = I_\mathrm{mag}^z + I_\mathrm{mag}^y + \frac{2}{3} I_\mathrm{inc}^\mathrm{mag} \tag{3.28}$$

$$I_x^\mathrm{nsf} = I_\mathrm{nuc} + \frac{1}{3} I_\mathrm{inc}^\mathrm{mag} \tag{3.29}$$

$$I_z^\mathrm{sf} = I_\mathrm{mag}^{non[1\bar{1}0]} + \frac{2}{3} I_\mathrm{inc}^\mathrm{mag} \tag{3.30}$$

$$I_z^\mathrm{nsf} = I_\mathrm{nuc} + I_\mathrm{mag}^{[1\bar{1}0]} + \frac{1}{3} I_\mathrm{inc}^\mathrm{mag} \tag{3.31}$$

Therefore, if the magnetic satellites only appear in I_z^nsf, the magnetic structure factor is in the $[1\bar{1}0]$ direction.

3.3.3 Determination of the T-B phase diagram

To determine the phase boundaries in the phase diagram of $\mathrm{CeCu_2Ge_2}$, magnetic satellites were tracked over temperature and magnetic field dependent scans. In the PANDA experiment, the AF1 to AF2 transition was investigated by mapping around the ($\vec{\tau}_\mathrm{h}$ $\vec{\tau}_\mathrm{h}$ 2-$\vec{\tau}_\mathrm{l}$) at 7.5 T, 7.7 T, 7.8 T and 8.0 T. The temperature was kept constant at 0.05 K.

The field dependence of the magnetic order at low temperature was further investigated in the diffraction experiment at D23. The evolution of the same magnetic Bragg peak with magnetic field was tracked by performing scans over H and L, respectively. To check for field induced changes in the nuclear structure or magnetic contributions on the positions of the nuclear Bragg peaks, rocking scans over the (004), (006), (110) and (222) nuclear Bragg peaks were performed. These rocking scans for each magnetic field were fitted using one Gaussian, except for the (110) peak, where two Gaussians were used to account for the presence of a small grain. In a similar way, the H and L scans over the magnetic Bragg peak were fitted with one Gaussian. At 12.6 T, rocking scans were performed over a large part of the Q-space to search for further magnetic order. Since only rocking scans were performed, small deviations from the [110]/[001] scattering plane occurred. However, these are smaller than the resolution for the setup used.

	AF1 to AF2 transition	field dependence of the magnetic order at low temperature	field and temperature dependence of the magnetic order at high temperature
instrument/facility	PANDA/MLZ	D23/ILL	E4/HZB
λ (Å)	4.8	2.4	2.4
scattering plane	[110]/[001]	[110]/[001]	[110]/[001]
T (K)	0.05	0.03	0.3 - 4
B (T)	7.5 - 8.0	0 - 12.6	0 - 12.6
B direction	$[1\bar{1}0]$	$[1\bar{1}0]$	$[1\bar{1}0]$
data provided by	A. Schneidewind (JCNS)		
experimental team		P. Geselbracht (TUM), A. Schneidewind (JCNS)	P. Geselbracht (TUM), A. Schneidewind (JCNS)
local contact		K. Schmalzl (JCNS)	K. Prokeš (HZB), F. Yokaichiya (HZB)

TABLE 3.6: Information of the diffraction experiments to determine the T-B phase diagram.

The phase diagram was further explored in the range of $B < 13$ T and 0.3 K $< \mathrm{T} < T_\mathrm{N}$ in a diffraction experiment at E4 diffractometer. Magnetic satellites of the 002 and 110 Bragg peaks were measured, covering different domains. Scans over the sample rotation ω were performed. As the E4-diffractometer comes with an area detector, the peak positions could be unambiguously determined by projecting the area detector data on the respective coordinate in the instrument coordinate system (2Θ, ω, ν) [2].

The phase diagram was systematically mapped by sweeping either magnetic field with constant temperature or temperature with constant field. Due to limited beam time, (T, B) was moved directly to the first point of the next sweep after one sweep was finished, i.e. no systematic heating or ramping of the field between the sweeps was done.

---

[2] 2Θ: scattering angle; ω: sample rotation; ν: out of horizontal plane component

	short range order in $CeCu_2Ge_2$
instrument/facility	RESI (MLZ)
λ (Å)	1.05
scattering plane	[110]/[001]
T (K)	5 K
experimental team	P. Geselbracht (TUM)
local contact	B. Pedersen (TUM)

TABLE 3.7: Information of the diffraction experiment at RESI.

3.3.4 Search for short range order

Possible short range order was investigated in an experiment on the RESI diffractometer. The initial goal was to find a possible competing short range order corresponding to the unknown magnetic order. The $CeCu_2Ge_2$ single crystal was cooled to 3 K, where presence of the expected AF1 order with propagation vector $\vec{\tau} \approx (0.28\ 0.28\ 0.55)$ was confirmed. No magnetic field was applied. The sample was then heated to 5 K, slightly above the Néel temperature T_N. Scans over the sample rotation in the scattering plane were performed cutting through positions corresponding to the AF1 and AF2 phase, i.e $\vec{Q}_\mathrm{AF1} = (0.28\ 0.28\ 1.46)$ and $\vec{Q}_\mathrm{AF2} \approx (0.31\ 0.31\ 1.47)$. A further scan along (0.9...1.8 0 0) was made.

3.3.5 Investigation of spin dynamics

For the investigation of the spin dynamics of a system, inelastic scattering experiments, i.e. with energy transfer $E \neq 0$, were performed on triple-axis spectrometers. It is convenient to express the double differential scattering cross section as

$$\frac{d^2\sigma}{d\Omega dE} = \frac{k_f}{k_i}\vec{F}_M(\vec{Q})S(\vec{Q},E) \tag{3.32}$$

where $S(\vec{Q},E)$ is the scattering function, sometimes called dynamic structure factor [88]. The inelastic responds of the sample under investigation then can be conveniently modeled by an appropriate choice of $S(\vec{Q},E)$, which only depends on E and $\vec{Q}$.

With triple axis spectrometers as used in this work for inelastic scattering, the intensity is subject to the instrument specific resolution function $R(\vec{Q},E)$. In case of the here used constant Q-scans, the measured intensity is a convolution of $S(\vec{Q},E)$ with $R(\vec{Q},E)$.

$$I\left(\vec{Q}_0, E_0\right) = \iint_{d\vec{Q},dE} R\left(\vec{Q}-\vec{Q}_0, E-E_0\right) S\left(\vec{Q},E\right) d\vec{Q}dE \tag{3.33}$$

The shape of $R(\vec{Q}, E)$ is typically of a four dimensional Gaussian ($\vec{Q}$, E-space). A simple method for approximating $R(\vec{Q}, E)$ is to model the elastic scattering in $S(\vec{Q}, E)$ by a delta function. The broadening in energy of this delta function then is the direct result of the convolution with $R(\vec{Q}, E)$, which is called the elastic line. Hence, if this elastic line can be fitted, the resolution of the instrument is known at the specific $\vec{Q}$-point of the elastic line.

To find an an appropriate model for $S(\vec{Q}, E)$, the interest in this work is in the magnetic fluctuations. Therefore, $S(\vec{Q}, E)$ can be expressed in terms of the dynamic susceptibility χ'':

$$S(\vec{Q}, E) = (n+1)\chi''(\vec{Q}, E) = \frac{1}{1 - e^{-E/k_B T}}\chi''(\vec{Q}, E) \tag{3.34}$$

where n is the bose distribution. The temperature term stems from the principle of detailed balance. It accounts for the temperature dependent occupation of excited states which alters the probability of the occurrence of a scattering event. It leads to the relation

$$S(-\vec{Q}, -E) = e^{-E/k_B T} S(\vec{Q}, E) \tag{3.35}$$

Therefore, at very low temperature, the intensity of the neutron energy gain virtually vanishes and meaningful information on the excitation spectrum only can be obtained for neutron energy loss. The neutron energy gain side can be used to determine the instrument related background.

χ'' is related to the static susceptibility χ' by the Kramers–Kronig relation. χ'' can be expressed in the general from

$$\chi''(\vec{Q}, E) = \chi'(\vec{Q}, 0) E F(\vec{Q}, E) \tag{3.36}$$

with the spectral weight function $F(\vec{Q}, E)$. Eq. 3.34 then becomes

$$S(\vec{Q}, E) = \frac{1}{1 - e^{-E/k_B T}}\chi'(\vec{Q}, 0) E F(\vec{Q}, E) \tag{3.37}$$

Therefore, the description of the excitation spectrum is narrowed to an appropriate choice of the excitation spectrum.

In the following the most common spectral weight functions and their applications are discussed. Fluctuations that are not long range correlated, but restricted to a single site have no characteristic excitation energy and thus $F(\vec{Q}, E)$ function is centered at $E = 0$. If coupled to their environment, they decay exponentially, so $F(\vec{Q}, E)$ takes the simple form of the Lorentz distribution:

$$F(\vec{Q}, E) = \frac{1}{\pi}\frac{\Gamma}{E^2 + \Gamma^2} \tag{3.38}$$

This type of excitation is often called quasi elastic. In heavy fermion systems as investigated here, such type of fluctuations arise from the Kondo effect [11].

For inter site fluctuations, such as spin waves or paramagneons, damped harmonic oscillator (DHO) and over damped harmonic oscillator (ODHO) models are sufficient in most cases. For the over damped harmonic oscillator, $F(\vec{Q}, E)$ has a Lorentzian shape as the quasi elastic, but its center is shifted by the excitation energy E_0:

$$F(\vec{Q}, E) = \frac{1}{\pi}\left(\frac{E\Gamma}{(E - E_0)^2 + \Gamma^2} + \frac{E\Gamma}{(E + E_0)^2 + \Gamma^2}\right) \tag{3.39}$$

In case of the DHO we have

$$F(\vec{Q}, E) = \frac{1}{\pi}\frac{2\Gamma E_0^2}{(E^2 - E_0^2) + (2\Gamma E)^2} \tag{3.40}$$

The two Lorentzian terms for the ODHO are needed to reproduce the response for neutron energy gain and loss. In case of the DHO, this is not needed due to the E^2 term. It should be noted that the ODHO is symmetric in respect to E_0, while the DHO is not. The DHO has more weight at small energies.

Similar as in the previously described diffraction experiment, a single wave length is selected from the white beam coming from the source and then is scattered by the sample. But instead of directly placing the detector after the sample, the analyzer is placed there. It selects a single wave vector from the scattered beam by Bragg scattering in a similar way as the monochromator. This results in the ”W”-shaped path of the beam which can be clearly seen in Fig. 3.7. Afterwards, the detector is placed to count the neutrons coming from the analyzer. As with this setup, the incident wave vector as well as final wave vector is known, the energy transfer is also known in addition to the momentum transfer.

The dispersion and the temperature dependence of the spin waves were probed in the IN12 experiment. In two experiments on PANDA with similar experimental conditions,

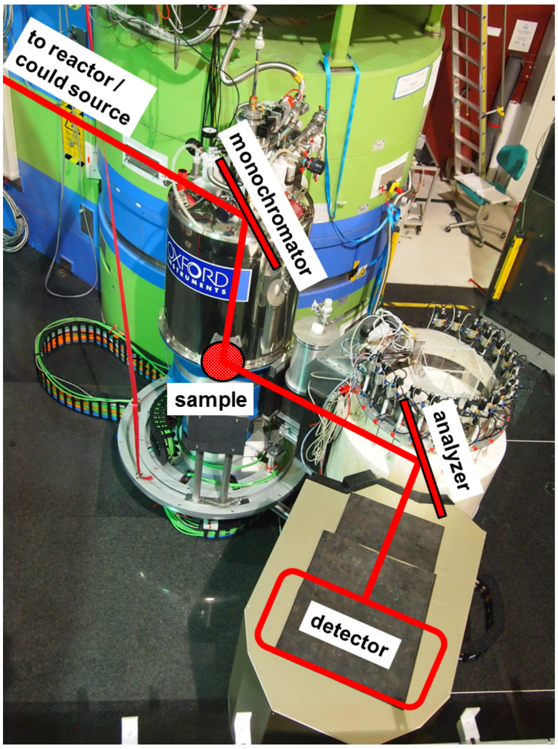

FIGURE 3.7: Picture of the cold three axes spectrometer PANDA [109] at the Maier-Leibnitz Zentrum. The red line shows the path of the neutron beam.

also the dispersion and the field dependence of the spin waves up to 11.5 T were measured. In the V2 FLEXX experiment, the excitation spectrum at 13.5 T was investigated. Exclusively, constant-$\vec{Q}$ scans over the energy transfer were performed. For the measurement of the field and temperature dependence, the scans were recorded at the Γ-point of the magnetic unit cell, i.e. $\vec{Q} = \vec{Q}_{\mathrm{AF}} = (\tau_{\mathrm{h}}\ \tau_{\mathrm{h}}\ 2\text{-}\tau_{\mathrm{l}})$. The dispersion was measured with $\vec{Q} = (\mathrm{H}\ \mathrm{H}\ 2\text{-}\tau_{\mathrm{l}})$ and $\vec{Q} = (\tau_{\mathrm{h}}\ \tau_{\mathrm{h}}\ \mathrm{L})$. In the V2 FLEXX experiment at 13.5 T, where the Γ-point of the magnetic unit cell was not known, the measurement was made at $\vec{Q} = \vec{Q}_{\mathrm{AF2}} \approx (0.314\ 0.314\ 1.444)$.

The data was normalized on the monitor placed right after the monochromator. The elastic line at the Γ-point of the magnetic unit cell was fitted using a total of three Gaussians. These correspond to the coherent as well as incoherent elastic line and and a broader tail that is not uncommon in triple axis data [110], especially for strong elastic lines. Note that for the IN12 data at Q_{AF} an additional Gaussian had been added at 0.25 meV (FWHM 0.25 meV) to account for additional 20 cnts (0.4 K). This is most likely an artifact corresponding to the instrument resolution in combination with a magnetic Bragg peak more than 1000 times stronger than the inelastic signal. Away from $\vec{Q}_{\mathrm{AF}}$, a single Gaussian sufficiently describes the data. The width of the coherent elastic line at PANDA with $k_{\mathrm{f}} = 1.3$ Å^{-1} is 40 μeV in agreement with calculations based on [111], assuming $\approx 1^{\circ}$ sample mosaicity. For the coherent elastic line in the IN12 data with $k_{\mathrm{f}} =$

1.2 $Å^{-1}$, an only slightly larger width of 50 μeV was obtained. Therefore, Eq. 3.33 may be approximated to $I(\vec{Q}, E) \propto S(\vec{Q}, E)$. A constant background was estimated from the neutron energy gain side.

Unfortunately V2 FLEXX has lower Q-space resolution, limiting the usefulness of those data. The elastic line was fitted using only one single Gaussian as it consisted only of incoherent scattering. A constant background of 5.5 counts was assumed. The remaining inelastic spectrum was fitted using two Gaussians.

	dispersion and temperature dependence of spin waves	dispersion and field dependence of spin waves	excitation spectrum at 13.5 T
instrument/facility	IN12/ILL	PANDA/MLZ	V2 FLEXX/HZB
k_f (Å^{-1})	1.2 (fixed)	1.3 (fixed)	1.3 (fixed)
energy resolution	50	40	120
energy range (meV)	0 - 3.5	0 - 3.5	0 - 3.5
scattering plane	[110]/[001]	[110]/[001]	[110]/[001]
T (K)	0.4 - 4.1	0.04 - 0.5	0.3 - 4
B (T)	0	0 - 11.5	13.5
B direction	-	$[1\bar{1}0]$	$[1\bar{1}0]$
data provided by	A. Schneidewind (JCNS)	A. Schneidewind (JCNS) (field dependence)	
experimental team		P. Geselbracht (TUM)	P. Geselbracht (TUM), K. Schmalzl (JCNS), A. Schneidewind (JCNS)
local contact		A. Schneidewind (JCNS) (dispersion)	D. Quintero Castro (HZB)

TABLE 3.8: Information of the inelastic experiments.

3.4 $\mathbf{CeCu_2(Si_{0.55}Ge_{0.45})_2}$

3.4.1 Determination of the T-B phase diagram

Neutron diffraction was performed on the focusing powder diffractometer E6. Rocking scans (rotating the sample with constant scattering angle) were performed on the (τ_h τ_h 2-τ_h) magnetic satellite for various magnetic fields and temperatures. From these scans, the integrated intensity was obtained by fitting one Gaussian to the data and subtracting a constant background. Data for $T < T_L$ = 2.1 K had to be fitted with two Gaussians, because in this phase the Brillouin zone is reduced and additional magnetic satellites slightly overlap each other from previously forbidden Bragg reflections [66].

Because of the area detector of the E6 diffractometer, the integrated intensity is not affected by small temperature or magnetic field dependencies of the propagation vector. The integrated intensity was normalized on the (110) nuclear Bragg peak.

To complement the neutron scattering data, specific heat raw data with [1$\bar{1}$0] field direction were provided by J. Arndt (CPfS). The data were measure using the compensated heat-pulse technique. The principle is that a defined amount of heat is transferred to the sample and the increase in temperature is measured. Heat losses are compensated using constant background heating. A detailed description is given in [112]. The setup was mounted in an Oxford dilution cryomagnet to achieve temperatures down to 50 mK and magnetic fields up to 8 T. Temperature sensing was done using a RuO_2 thermometer calibrated against a Ge-thermometer close to the mixing chamber outside the magnetic field.

instrument/facility	E6/HZB
λ (Å)	2.4
scattering plane	[110]/[001]
T (K)	0.5 K - 3.5
B (T)	0 - 6.5
B direction	[1$\bar{1}$0]
data provided by	A. Schneidewind (JCNS)

TABLE 3.9: Parameters of the diffraction experiment at E6.

Chapter 4

Magnetic properties of $CeCu_2Ge_2$

4.1 Zero field magnetic structure

In this chapter, the experiments on the magnetic structure of $CeCu_2Ge_2$ is presented. It is so far the first investigation based on single crystal data. First, the indexing of magnetic satellites from [36] with propagation vector $\vec{\tau}_{AF1}$ = (0.284 0.284 0.544) is confirmed with high-$\vec{Q}$ resolution. Then, the results of the representation analysis are presented. Followed by the discussion of the temperature dependence of the magnetic order below T_N. The evaluation of xyz-analysis shows that the magnetic structure factor has solely a component in the $[1\bar{1}0]$ direction. Complementary, the magnetic structure is also refined for a set of unpolarized data, yielding two possible magnetic structures: spin density waves with either one or two directions of the amplitude modulation. The respective ordered moments are $\mu_{ord}^{1\text{-k}} = 1.0\mu_B$ (1-k structure) and $\mu_{ord}^{2\text{-k}} = 0.7\mu_B$ (2-k structure). From the neutron scattering alone, these two structures are indistinguishable. Considering the saturated magnetization for field along [001] is $\mu_s = 1\mu_B$, the 1-k structure is favored. No hints for a change of the magnetic structure below T_N was detected.

4.1.1 Propagation vector

So far, only the magnetic structure of $CeCu_2(Si_{0.55}Ge_{0.45})_2$ has been rigorously solved as a cycloidal structure [66; 26]. A special feature of this magnetic structure is that in the low temperature phase, the I4/mmm symmetry from the nuclear parent structure no longer applies to the magnetic structure as the moment of the central Ce atom is not described by symmetry operations of the body centered I4/mmm parent structure and

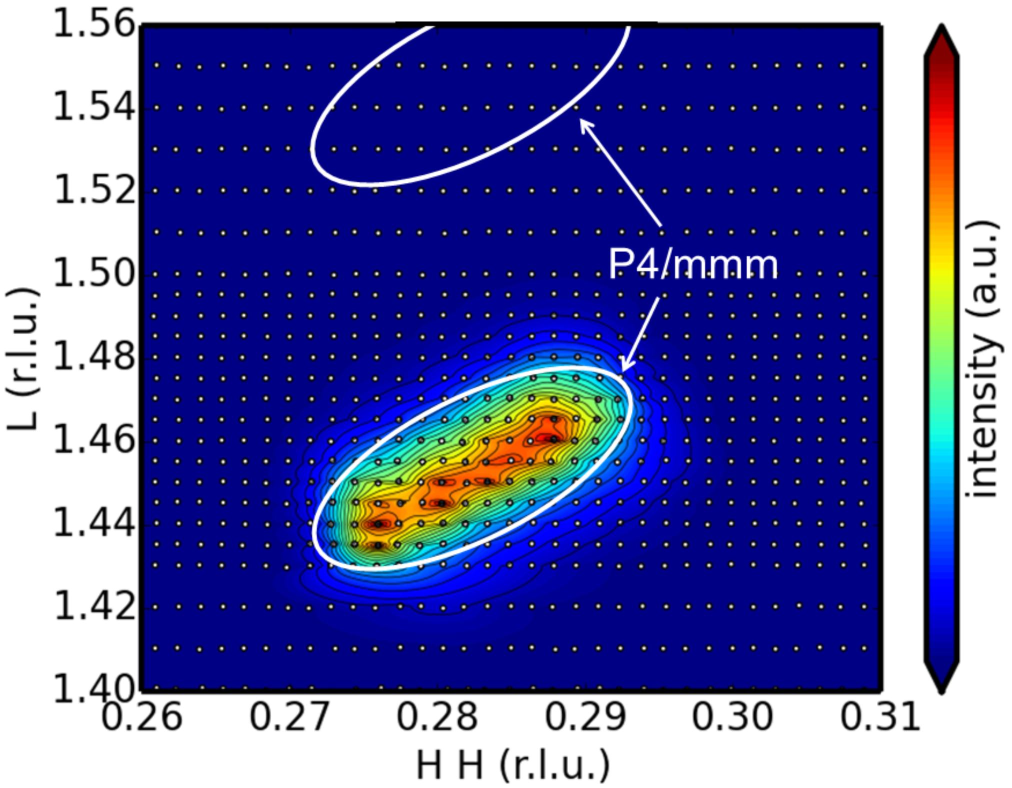

FIGURE 4.1: Intensity map in reciprocal (hhl) plane around (τ_h τ_h 2-τ_l) magnetic satellite at T = 50 mK.

the space group becomes P4/mmm. The centered atom is then described by an additional Wyckoff position (1/2,1/2,1/2) with multiplicity 1 and Wyckoff letter d. Therefore, magnetic satellites corresponding to otherwise forbidden peaks occur. As the τ_l component of the propagation vector in $CeCu_2(Si_{0.55}Ge_{0.45})_2$ is very close to the Brillouin zone boundary ($\tau_l \approx 0.49$), instruments with high $\vec{Q}$-resolution are required to separate the different satellites.

For a P4/mmm symmetry, the magnetic satellites (τ_h τ_h 1+τ_l) (1+$\tau_l \approx$ 1.45) as well as (τ_h τ_h 2-τ_l) (2-$\tau_l \approx$ 1.55) would arise in Fig. 4.1. This is obviously not the case here, as the 1+$\tau_l \approx$ 1.45 satellite is missing. This confirms the I4/mmm symmetry. The observed magnetic satellite is the (τ_h τ_h 2-τ_l) satellite. Thus this investigation yields a propagation vector $\vec{\tau}_{AF1}$ = (0.284 0.284 0.544), similar to the propagation vector established in [36].

4.1.2 Magnetic structure model

For the parent structure information from [21] and the above found propagation vector $\vec{\tau}_{AF1}$ = (0.284 0.284 0.544), two irreducible representations A1 and A2 are available. Both resulting structures are spin-density-waves. For A1 this direction is fixed to [1$\bar{1}$0],

k-point label	τ
SM	(a 0 0)
LD	(0 0 g)
DT	(a a 0)
Q	(1/2 b 1/2)
W	(1/2 1/2 g)
Y	(a -a+1 0)
A	(a a g)
B	(a 0 g)
C	(a b 0)
GP	(a b g)

TABLE 4.1: k-point labels (Kovalev notation [113]) for the I4/mmm space group and the corresponding type of propagation vector (a a g). The components a, b, g of the propagation vector have to fulfill the relation $|a| \neq |b| \neq |g|$. For clarity, only k-point labels that may result in incommensurate magnetic structures are listed. Taken from the tabulation in [95].

while in case of A2, components of the moment along [110] as well as [001] are possible. The moment $\vec{\mu}$ on site n can be expressed as

$$\vec{\mu}_n = \vec{\mu}_1 \cos\left(\vec{\tau} \cdot \vec{r}_n\right) + \vec{\mu}_2 \sin\left(\vec{\tau} \cdot \vec{r}_n\right) \tag{4.1}$$

in accordance with Eq. 3.15. For both A1 and A2 $\mu_2 = 0$ holds. For A1 the ordered moment is $\vec{\mu}_1 = \mu \vec{e}_{[1\bar{1}0]}$ and for A2 it is $\vec{\mu}_1 = \mu_a \vec{e}_{[110]} + \mu_c \vec{e}_{[001]}$.

As magnetic satellites are present at (±H ±H ±L), a total of four domains (90° and 270° rotation around [001] and 180° rotation around [010]) are necessary for the above structures. As an alternative approach, one may think of assigning an individual propagation vector to all types of magnetic satellites (+H +H +L), (+H +H -L), (+H -H +L), (-H +H +L). This is called a multi-k structure [92]. In this case, one would end up without any domains and four propagation vectors (+0.284 +0.284 +0.544), (+0.284 +0.284 -0.544), (+0.284 -0.284 +0.544), (-0.284 +0.284 +0.544). In Tab. 4.1, the k-point label along with the respective type of propagation vector are listed. The latter two proposed propagation vectors do not fit k-point label A as h = -k. GP can be also ruled out as $|a| \neq |b|$ is required. Hence, the latter two proposed propagation vectors can not be found for any k-point label, i.e. these types of propagation may not exist within the I4/mmm space group. The first two of the proposed propagation vectors correspond to k-point label A, as for one propagation vector. Therefore, a 2-k model with τ_1 = (+0.284 +0.284 +0.544) and τ_2 = (+0.284 +0.284 -0.544) can be used. To account for the (+H -H +L), (-H +H +L) peaks, a total of two domains (180° rotation around [010]) is assumed.

For each propagation vector the two irreproducible representations A1 and A2 are found as for the 1-k case. In the case of the 2-k model, these irreproducible representations can be superposed together. The superposition can be done in different ways, depending on a phase shift of the modulated order corresponding to the irreproducible representations. This phase shift may break additional symmetries. A detailed explanation is given in [93]. As long as there is no sign of an additional breaking of symmetry, except the two propagation vectors, the superposition is done in such a way that the highest symmetry is maintained. The resulting combinations A1A1, A1A2 and A2A2 give the moment $\vec{\mu}_n$ for Ce atom n at position $\vec{r}_n$ as follows[1]:

$$\vec{\mu}_{n,A1A1} = \begin{pmatrix} a \\ -a \\ 0 \end{pmatrix} \cos\left(\vec{\tau}_1 \cdot \vec{r}_n\right) + \begin{pmatrix} -a \\ a \\ 0 \end{pmatrix} \cos\left(\vec{\tau}_2 \cdot \vec{r}_n\right) \tag{4.2}$$

$$\vec{\mu}_{n,A1A2} = \begin{pmatrix} a \\ b \\ c \end{pmatrix} \cos\left(\vec{\tau}_1 \cdot \vec{r}_n\right) + \begin{pmatrix} a \\ -b \\ -c \end{pmatrix} \cos\left(\vec{\tau}_2 \cdot \vec{r}_n\right) \tag{4.3}$$

$$\vec{\mu}_{n,A1A2} = \begin{pmatrix} a \\ a \\ c \end{pmatrix} \cos\left(\vec{\tau}_1 \cdot \vec{r}_n\right) + \begin{pmatrix} a \\ a \\ -c \end{pmatrix} \cos\left(\vec{\tau}_2 \cdot \vec{r}_n\right) \tag{4.4}$$

Except for A1 and A1A1, the moment directions are not restricted to a specific direction, i.e. the direction is a parameter for refinement. Thus, at first, the obtained models will be refined for the unpolarized neutron diffraction data and then the resulting structures will be discussed in regard to moment direction indicated by the polarized data.

4.1.3 Diffraction experiment with polarized neutrons

4.1.3.1 Temperatur dependence of the magnetic order below T_N

No variation of the lattice parameters was observed, as well as no hysteresis for the propagation vector. The integrated intensity does show a slight decrease in intensity upon cooling. The reason may be a slightly changed domain population. The two measured domains appear to be much more uniformly populated after the cooling measurement.

---

[1] For the moment directions a basis $\mu = a\vec{e}_{[100]} + b\vec{e}_{[010]} + a\vec{e}_{[001]}$, i.e. along the lattice was chosen.

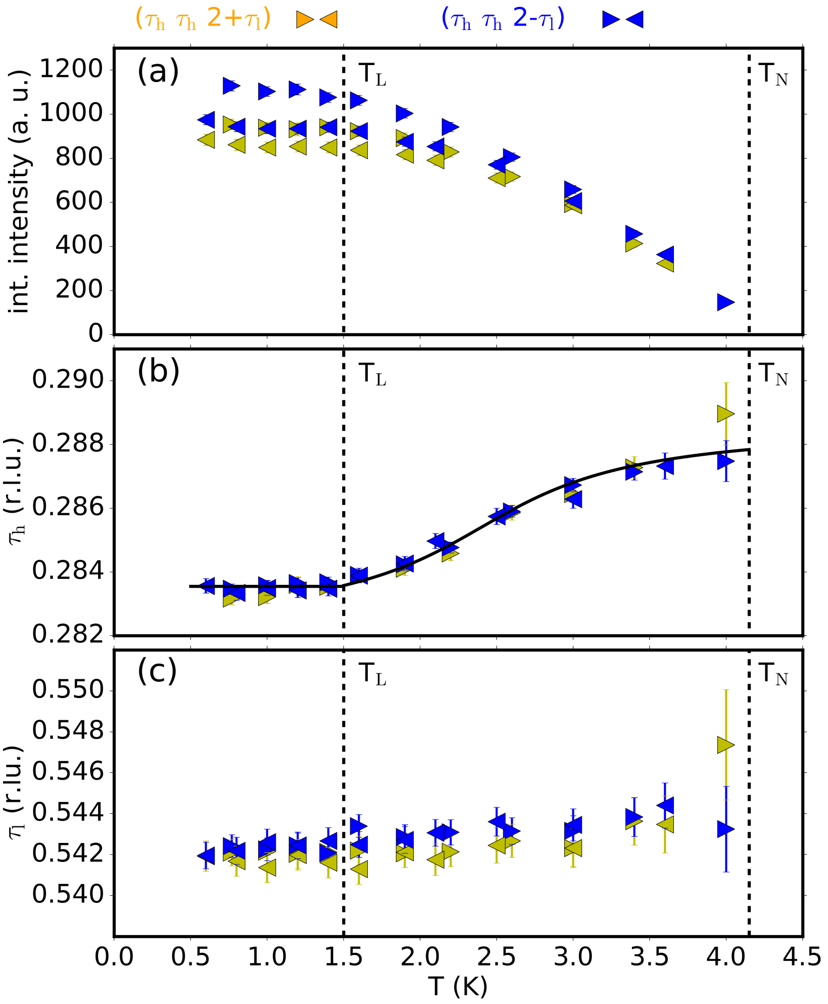

FIGURE 4.2: Temperature dependence of the integrated intensity (a), the τ_h (b) and τ_l (c) component of the propagation vector. T_L and T_N are described in the text. The integrated intensity was normalized on the (004) nuclear peak. The solid line is guides for the eye. Measurement up on heating is marked by (▷) and cooling (◁)

We turn now to the different temperature ranges. The Néel-Temperature T_N = 4.15 K is consistent with previous works [35; 36; 34]. For the whole temperature range, no anomaly the integrated intensity is present. Fitting the empiric formula $I \propto [1-(T/T_c)^{\alpha}]^{2\beta}$ gave the results shown in Tab. 4.2. The obtained value β matches the reported value in [36] as well as the mean field value β = 0.5. The empirical correction α is consistent with α = 2.7 for CePd$_2$Si$_2$ [114].

The $\vec{\tau}_\mathrm{h}$ component of the propagation vector shows a rather strong temperature dependence compared to the $\vec{\tau}_\mathrm{l}$ component. Over the whole temperature range, the $\vec{\tau}_\mathrm{l}$ component has only a slight linear temperature dependence. At T_L = 1.5 K, a lock-in

	I_0	α	2β
(τ_h τ_h 2+τ_l) heating	980 ± 20	2.4 ± 0.3	0.83 ± 0.06
(τ_h τ_h 2-τ_l) heating	1160 ± 20	2.2 ± 0.2	0.85 ± 0.04
(τ_h τ_h 2+τ_l) cooling	867 ± 4	3.6 ± 0.2	1.08 ± 0.05
(τ_h τ_h 2-τ_l) cooling	962 ± 8	3.0 ± 0.2	0.94 ± 0.05

TABLE 4.2: Fit result of the temperature dependence to $I \propto [1 - (T/T_c)^{\alpha}]^{2\beta}$.

transition, i.e. the propagation vector locks-in to a constant value, happens as suggested [36] for the range of 0.5 K ... 1.5 K. It was further suggested, that this is a transition to a commensurate magnetic structure with τ = (2/7 2/7 7/13). From this observations, no fundamental change in the magnetic structure with temperature is expected. This is consistent with specific heat measurements [42].

4.1.3.2 xyz-polarization analysis

From the $\vec{x}$-polarization (Fig. 4.3), one can see that for $T < T_N$, the incommensurate magnetic satellites appear at all (±H ±H ±L) positions. No signs for higher harmonic satellites or a multi-k structure with $|\vec{\tau}_1| \neq |\vec{\tau}_2|$ are present. Therefore, squaring up of the magnetic structure even at low temperature can be ruled out. As expected, at 6 K $> T_N$, no magnetic intensity is present on the incommensurate positions. For the $\vec{z}$-polarization (Fig. 4.4), the magnetic satellites only show up for the nsf and not in the sf channel. This means that no component of the magnetic structure factor is in the [110]/[001] scattering plane, but only a component perpendicular, i.e. in the [1$\bar{1}$0] direction, is present. Therefore, structure A2 from the previously presented representation analysis, can be ruled out as its magnetic moments are confined to the [110]/[001] scattering plane.

There is no change upon entering the lock-in phase, which is consistent with the temperature dependence of intensity and propagation vector shown above.

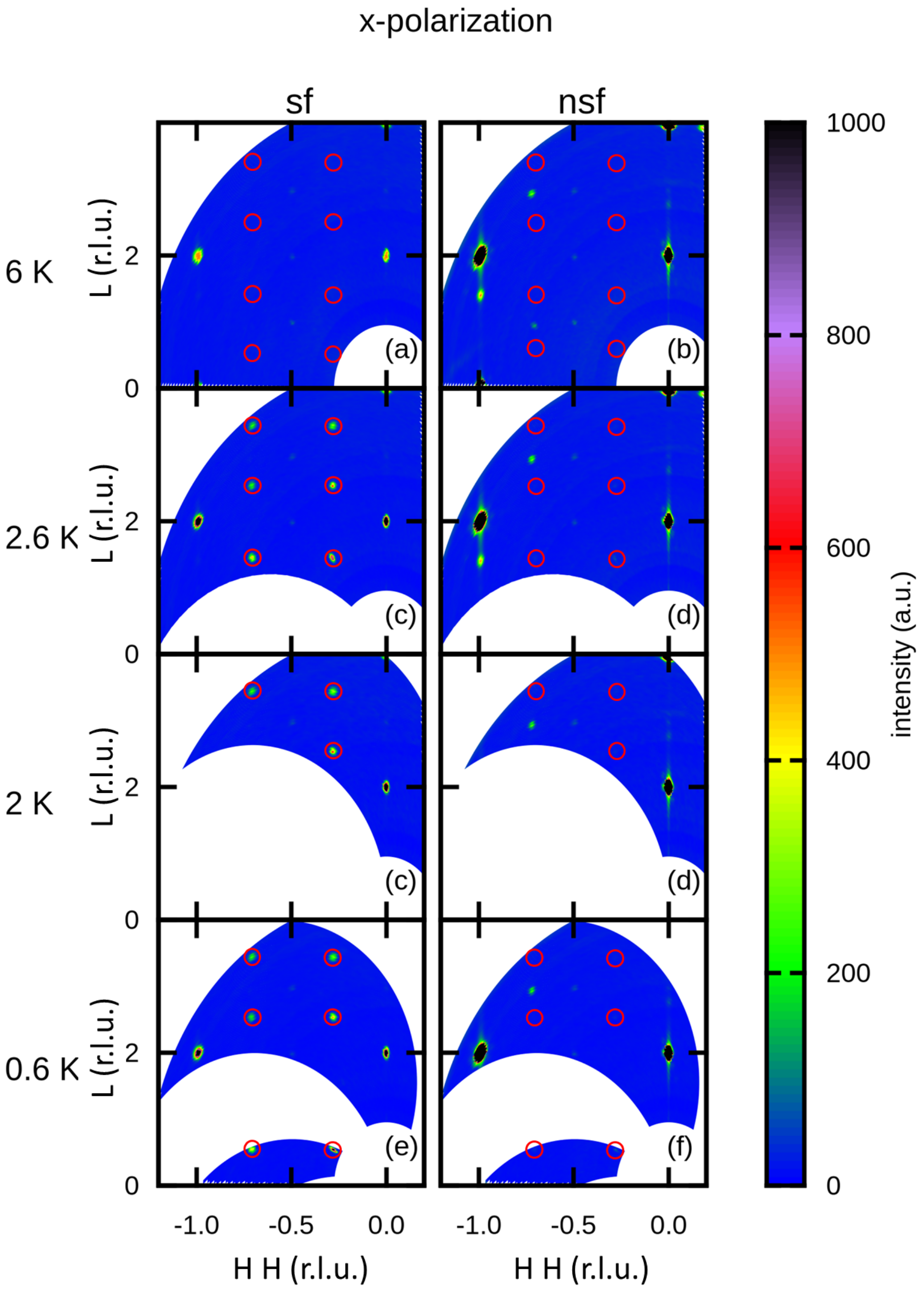

FIGURE 4.3: Elastic intensity maps in both spin-flip (left column) and non spin-flip (right column) mode with x-polarization for 6 K (a + b), 2.6 K (c + d), 2 K (e + f) and 0.6 (g + h). The red circles mark the position of the magnetic satellites.

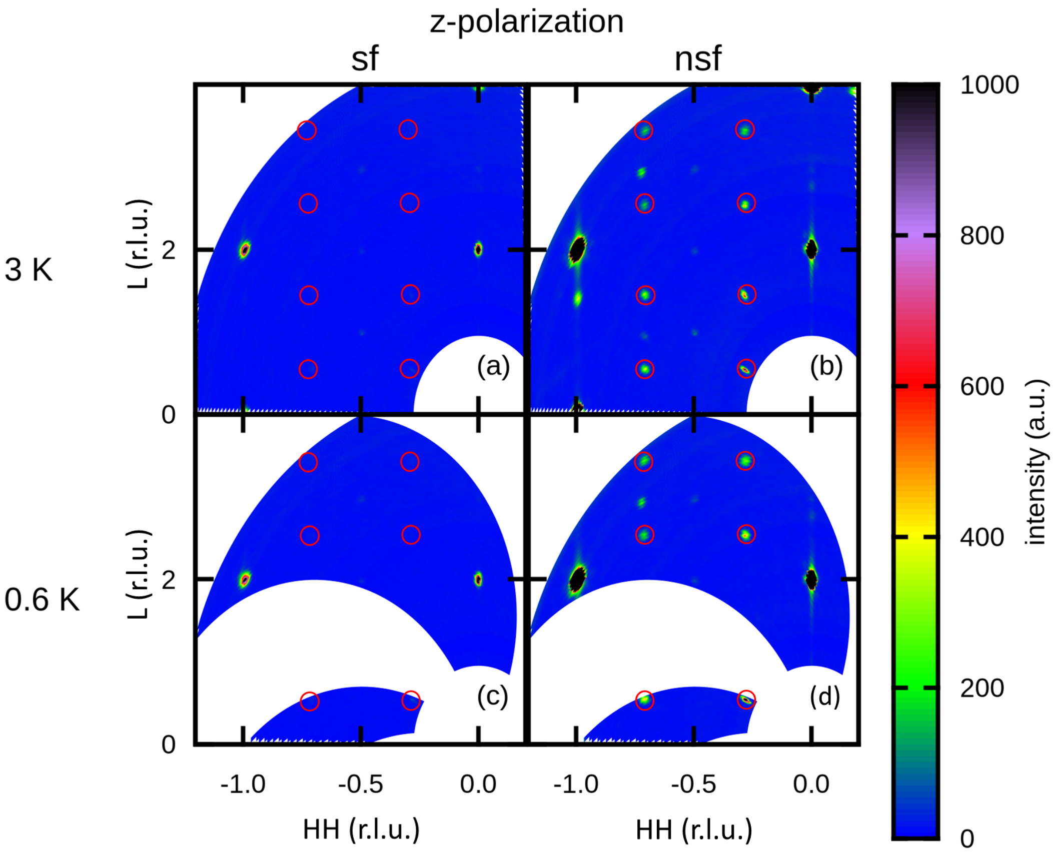

FIGURE 4.4: Elastic intensity maps in both spin-flip (left column) and non spin-flip (right column) mode with z-polarization for 3 K (a + b) and 0.6 K (c + d). The red circles mark the position of the magnetic satellites.

4.1.4 Refinement of the magnetic structure

Model A1 results in a significant better fit (R = 8.44%, see Fig. 4.5) of the observed intensities compared to model A2 (R = 38.77%). This is in agreement with the xyz-polarization analysis, as model A2 yielded no magnetic component in [1$\bar{1}$0] direction, but in the [110]/[001] plane with an angle of (50±12)° to the [001] direction. The ordered moment for model A1 is $\mu_{\mathrm{ord}}^{\mathrm{1\text{-}k}}$ = (1.0±1)μ_{B}. To reproduce magnetic satellites at all (±H ±H ±L) positions, a total of four domains have to be assumed: a 180° rotation around [010] as well as rotations of 90° and 270° around [001] (see Fig. 4.7 (top)).

The results of the refinement of the 2-k models are depicted in Fig. 4.6.

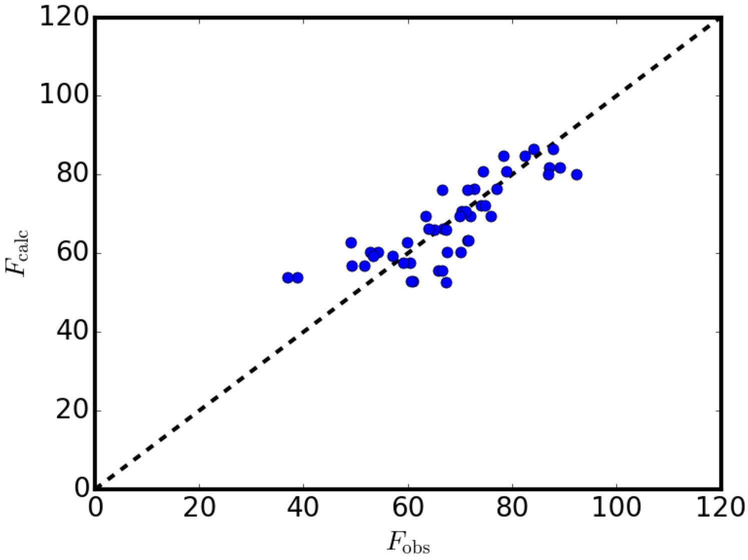

FIGURE 4.5: Plot of the calculated and observed magnetic structure factors for the 1-k model A1.

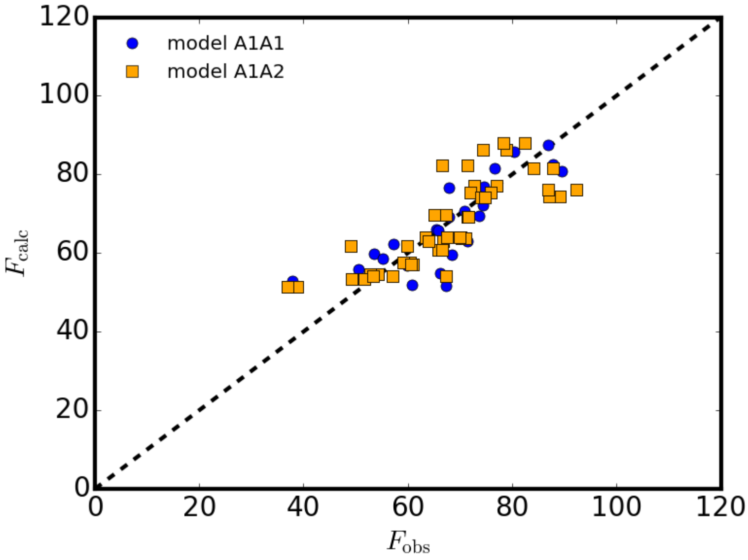

FIGURE 4.6: Plot of the calculated and observed magnetic structure factors for both 2-k models A1A1 and A1A2.

Model A2A2 can be ruled out as it gives an unsatisfying R value (37.70%) and is also in contrast to the polarized measurements as it gives a direction of magnetic components similar to 1-k model A2. The remaining models A1A1 and A1A2 give all satisfying R values (8.34% and 8.41%, see Fig. 4.6), similar to 1-k model A1. The refined free parameters for Model A1A2 yielded a Fourier component that does not point along [1-10]. Thus, A1A2 contradicts the polarized data as observable intensity should be in the sf mode for z-polarization.

The remaining model A1A1 yields an ordered moment of $\mu_{\mathrm{ord}}^{\text{2-k}}$ = (0.6$\pm$1) μ_{B} in the [1$\bar{1}$0] direction. The calculated intensities for peaks at positions $m\vec{\tau}_1 + n\vec{\tau}_2$ ($m, n \in \mathbb{N}$) were found to be $< 10^{-4} \cdot I_{\vec{\tau}_{i=1,2}}$, rendering these peaks unobservable small, in agreement with the measurements.

To compare the remaining models that satisfactorily describe the diffraction pattern (1-k model A1, 2-k model A1A1), the magnetic structure factors are evaluated in the following. To do this, Eq. 4.1 for model A1 is rewritten in such a way that the Fourier components can be directly read off:

$$\vec{\mu}_n = \frac{\vec{\mu}_{1-k}}{2} e^{i(+\vec{\tau})\cdot\vec{r}_n} + \frac{\vec{\mu}_{1-k}}{2} e^{i(-\vec{\tau})\cdot\vec{r}_n} \tag{4.5}$$

The Fourier components are $\vec{m}_{+\vec{\tau}} = \vec{m}_{(-\vec{\tau})} = \frac{\vec{\mu}_{1-k}}{2}$. The magnetic structure factor (Eq. 3.17) becomes

$$\vec{F}_{M,1-k}\left(\vec{Q} = \vec{H} + \vec{\tau}\right) = p f_{\mathrm{Ce}^{3+}}\left(\vec{Q}\right) \frac{\vec{\mu}_{1-k}}{2} \left(1 + e^{\pi i(H+K+L)}\right) \tag{4.6}$$

Similarly for model A1A1 we have

$$\vec{\mu}_n = \frac{\mu_{2-k}}{2} e^{i(+\vec{\tau})\cdot\vec{r}_n} + \frac{\mu_{2-k}}{2} e^{i(-\vec{\tau})\cdot\vec{r}_n} - \frac{\mu_{2-k}}{2} e^{i(+\vec{\tau})\cdot\vec{r}_n} - \frac{\mu_{2-k}}{2} e^{i(-\vec{\tau})\cdot\vec{r}_n} \tag{4.7}$$

Therefore, the Fourier components are $\vec{m}_{+\vec{\tau}_1} = \vec{m}_{-\vec{\tau}_1} = -\vec{m}_{+\vec{\tau}_2} = -\vec{m}_{-\vec{\tau}_2} = \frac{\vec{\mu}_{2-k}}{2}$. The magnetic structure factor becomes

$$\vec{F}_{M,2-k}\left(\vec{Q} = \vec{H} + \vec{\tau}\right) = p f_{\mathrm{Ce}^{3+}}\left(\vec{Q}\right) \frac{\vec{\mu}_{2-k}}{2} \left(1 + e^{\pi i(H+K+L)}\right) \tag{4.8}$$

It is equivalent to the structure factor for the 1-k structure factor, except the size of the moment. To further discuss the size of the ordered moment, the domains for the 2-k structure have to be known.

To produce magnetic satellites at all (±H ±H ±L) positions, domains do not necessarily need to exist for multi-k structures. In the case of A1A1, where the model consists of the superposition of the same two irreducibles, the magnetic structure does not change under the 180° rotation around [010]. Therefore, only two domains corresponding to a 90° rotation around [001] are present (see Fig. 4.7 (bottom)). The magnetic satellites of only one of these domains lie in the scattering plane.

Coming back to the size of the ordered moment, one has to consider that the scattering volume is half the size for the 1-k model, compared to the 2-k model, as twice the

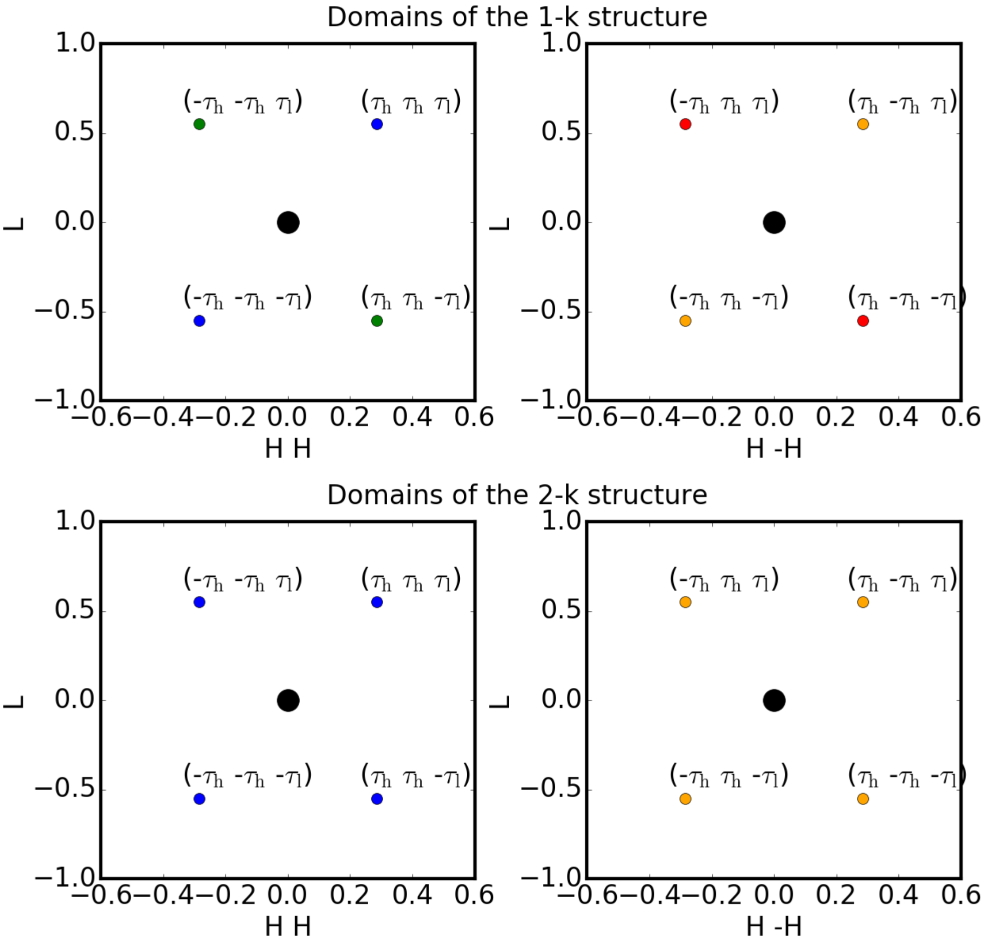

FIGURE 4.7: Magnetic satellites around (000). The colors represent the domains in case of the 1-k structure (top) and the 2-k structure (bottom). All experiments have been carried out in the [110]/[001] scattering plane (left column).

number of domains are present. Thus, the relation $\mu_{\text{ord}}^{\text{1-k}} = \sqrt{2}\mu_{\text{ord}}^{\text{2-k}}$ should be fulfilled. This is, within the uncertainty, the case. Hence, the resulting diffraction patterns are indistinguishable.

For both cases, the zero field phase is collinear with moments along the $[1\bar{1}0]$ direction. For the 1-k structure (model A1), the amplitude of the moment is modulated along a single direction $\vec{\tau}$, resulting in a stripe like pattern (Fig. 4.8). The 2-k structure (model A1A1) has its modulation along two directions: $\vec{\tau}_1$ and $\vec{\tau}_2$ (Fig. 4.9).

In both models, the confinement of the moments to the basal plane is in line with the susceptibility reported in [34]. If magnetic field is applied along [001], the moments rotate in the field directions resulting in a saturated moment of $\mu_s = 1\mu_B$ [63], resembling the ordered moment of the 1-k structure. Therefore, the 1-k structure is preferred over the 2-k structure.

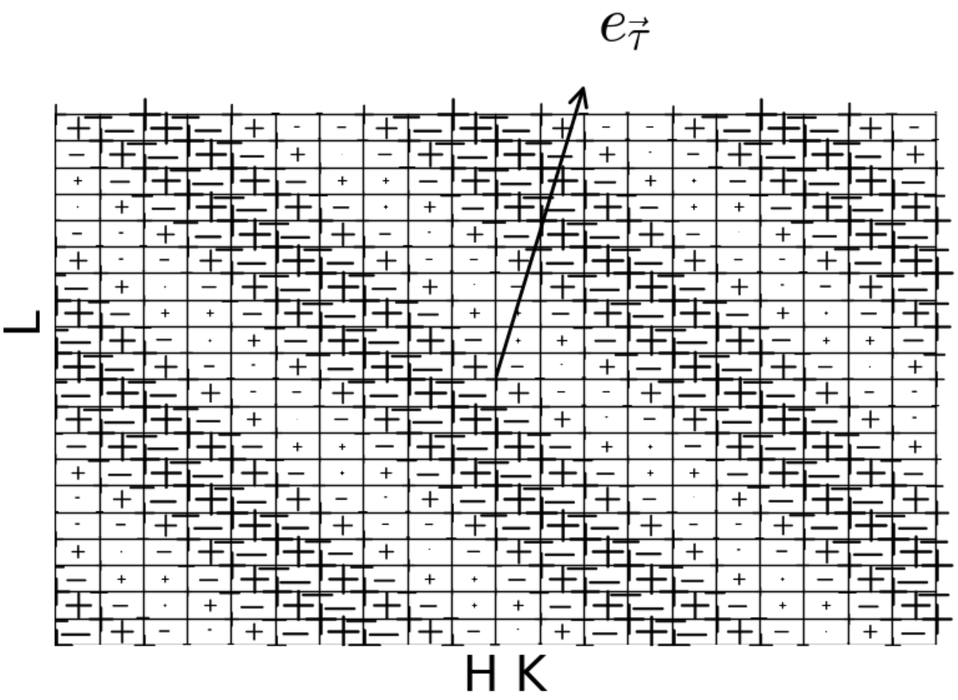

FIGURE 4.8: Drawing of the magnetic structure (model A1) in the plane spanned by [110]/[001]. The moments point out of the plane of projection. Their directions are indicated by '+' or '-' and the moment size is represented by the size of the symbols.

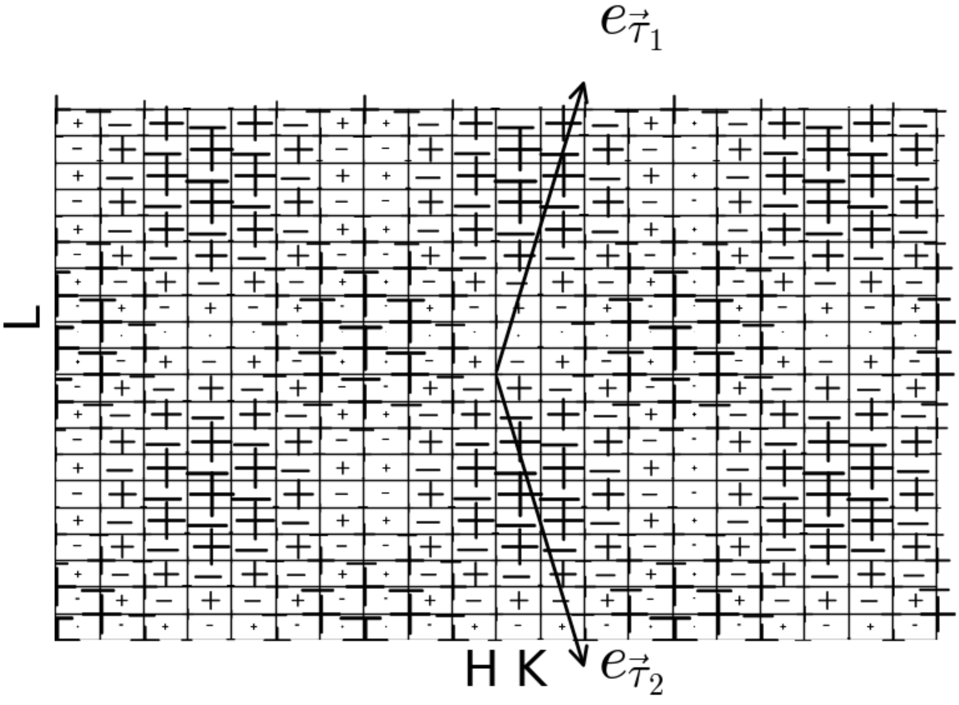

FIGURE 4.9: Drawing of the magnetic structure (model A1A1) in the plane spanned by [110]/[001]. The moments point out of the plane of projection. Their direction are indicated by '+' or '-' and the moment size is represented by the size of the symbols.

4.1.5 Summary

For the zero field magnetic order, the body centered symmetry was confirmed with the propagation vector $\vec{\tau}_{\mathrm{AF1}}$ = (0.284 0.284 0.544). Polarization analysis revealed that the magnetic structure factor has solely a component in the $[1\bar{1}0]$ direction. The representation analysis and subsequent refinement yields a spin density wave with either one or two directions of the amplitude modulation. The respective ordered moments are $\mu_{\mathrm{ord}}^{\mathrm{1\text{-}k}}$ = $1.0\mu_{\mathrm{B}}$ (1-k structure) and $\mu_{\mathrm{ord}}^{\mathrm{2\text{-}k}}$ = $0.7\mu_{\mathrm{B}}$ (2-k structure). From the neutron scattering alone, these two structures are indistinguishable. Considering the saturated magnetization for field along [001] is μ_{s} = $1\mu_{\mathrm{B}}$, the 1-k structure is favored. No hints for a change of the magnetic structure below T_{N} was detected.

4.2 Magnetic phase diagram

At first the results at low temperature (T = 0.05 K) are presented. Three characteristic anomalies are found at B_1 = 7.8 T, $B_2 \approx$ 10 T and B_3 = 12.6 T. At B_1 and a change of the propagation vector is observed and at B_3 the magnetic satellites in the [110][001] scattering plane vanish. Afterwards, the remaining phase diagram for 0.3 K $< T <$ 4 K was determined. The propagation vector of the newly discovered AF2 phase was accurately determined as $\vec{\tau}_{\mathrm{AF2}}$ = (0.34 0.27 0.55) and the magnetic structure was found to be an elliptical helix with $|\vec{\mu}_1|$ = (1 ± 0.1) μ_B ($\vec{\mu}_1$ || [1$\bar{1}$0]) and $|\vec{\mu}_2|$ = (0.7 ± 0.1) μ_B ($\vec{\mu}_2$|| [001]). Finally, evidence for short range correlations corresponding to the AF1 and AF2 phases at 5 K in zero field are reported.

4.2.1 Field dependence of the magnetic propagation vector

In Fig. 4.10, intensity maps around the (H H L) magnetic Bragg peak are shown. At 7.5 T, the corresponding propagation vector is $\vec{\tau}_1 \approx$ (0.285 0.285 0.543), still very close to its zero field position given in Ref. [36]. At 7.7 T, a second peak starts to rise at a position corresponding to a propagation vector of $\vec{\tau}_2 \approx$ (0.310 0.310 0.543). At 7.8 T, both peaks coexist with roughly the same intensity and at 8 T the peak corresponding to $\vec{\tau}_1$ has vanished. This is clear evidence that a first-order phase transition is occuring at B_1 = 7.8 T. The zero field antiferromagnetic structure AF1 with propagation vector $\vec{\tau}_1$ jumps by a first-oder transition to a high magnetic field antiferromagnetic structure AF2 with propagation vector $\vec{\tau}_2$.

The evolution in magnetic field of the integrated intensity, as well as the τ_{h} = H and τ_{l} = 2-L component of the propagation vector is displayed in Fig. 4.11. Below 6 T, no major change of the AF2 structure is observed. Approaching B_1, the integrated intensity related to the AF1 phase starts to drop, accompanied by an increase of the L component, while no change in the H component is observed.

At B_1, one can see the change from the AF1 to the AF2 phase as it is also clearly visible in the contour maps that were presented in Fig. 4.10. The propagation vector jumps to $\vec{\tau}_2 \approx$ (0.310 0.310 0.550). The integrated intensity in the AF2 phase is approximately 3 times lower than in the AF2 phase.

At $B_2 \approx$ 10 T, an increase of the integrated intensity of the magnetic Bragg peak together with a shift of 0.005 r.l.u. in H and 0.012 r.l.u. in 2-L is observed. This coincides with an anomaly in the magnetostriction data from [65]. At 12 T, the integrated intensity starts to decline.

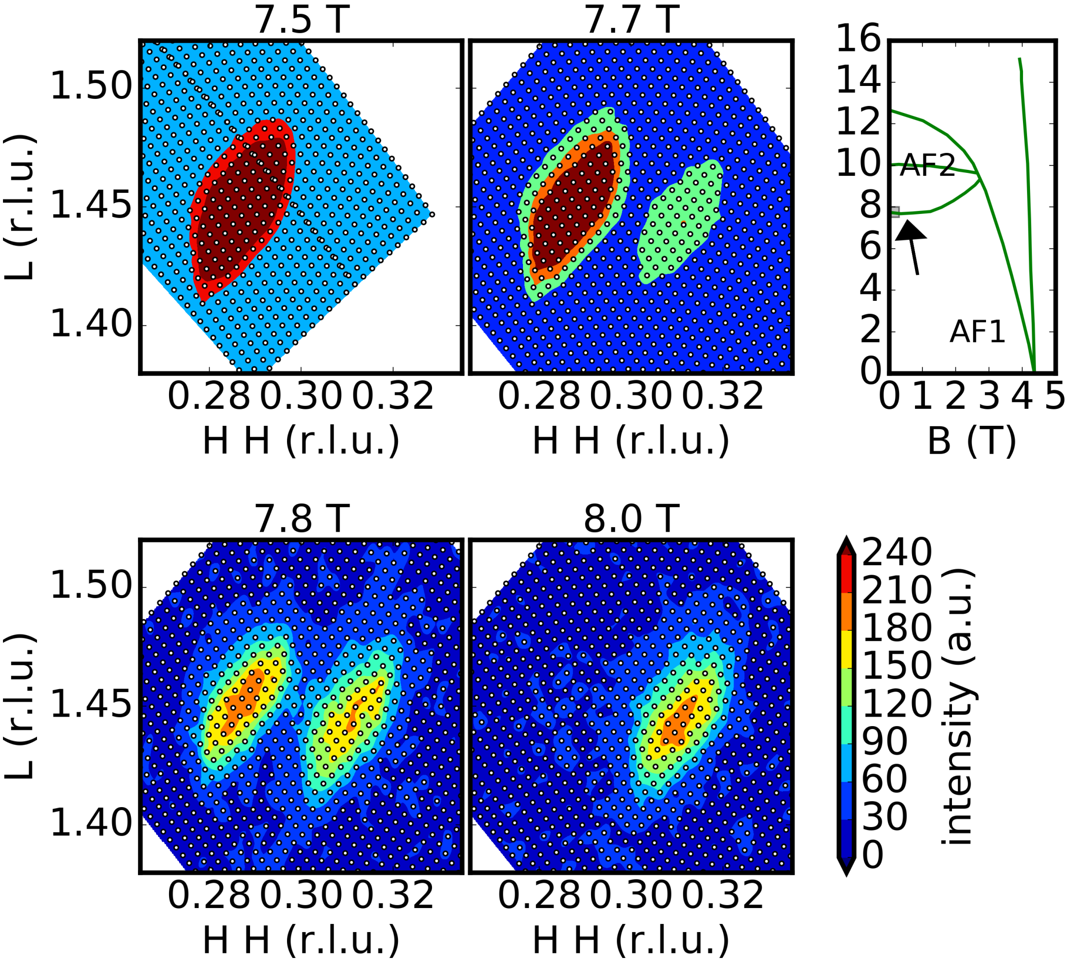

FIGURE 4.10: Magnetic field dependence of the magnetic Bragg peak at (H H L) in a narrow field range around the phase transition at B_1 = 7.8 T (T = 0.05 K). The position in the phase diagram is displayed in the top right with the transition lines from [65]. Data taken on PANDA.

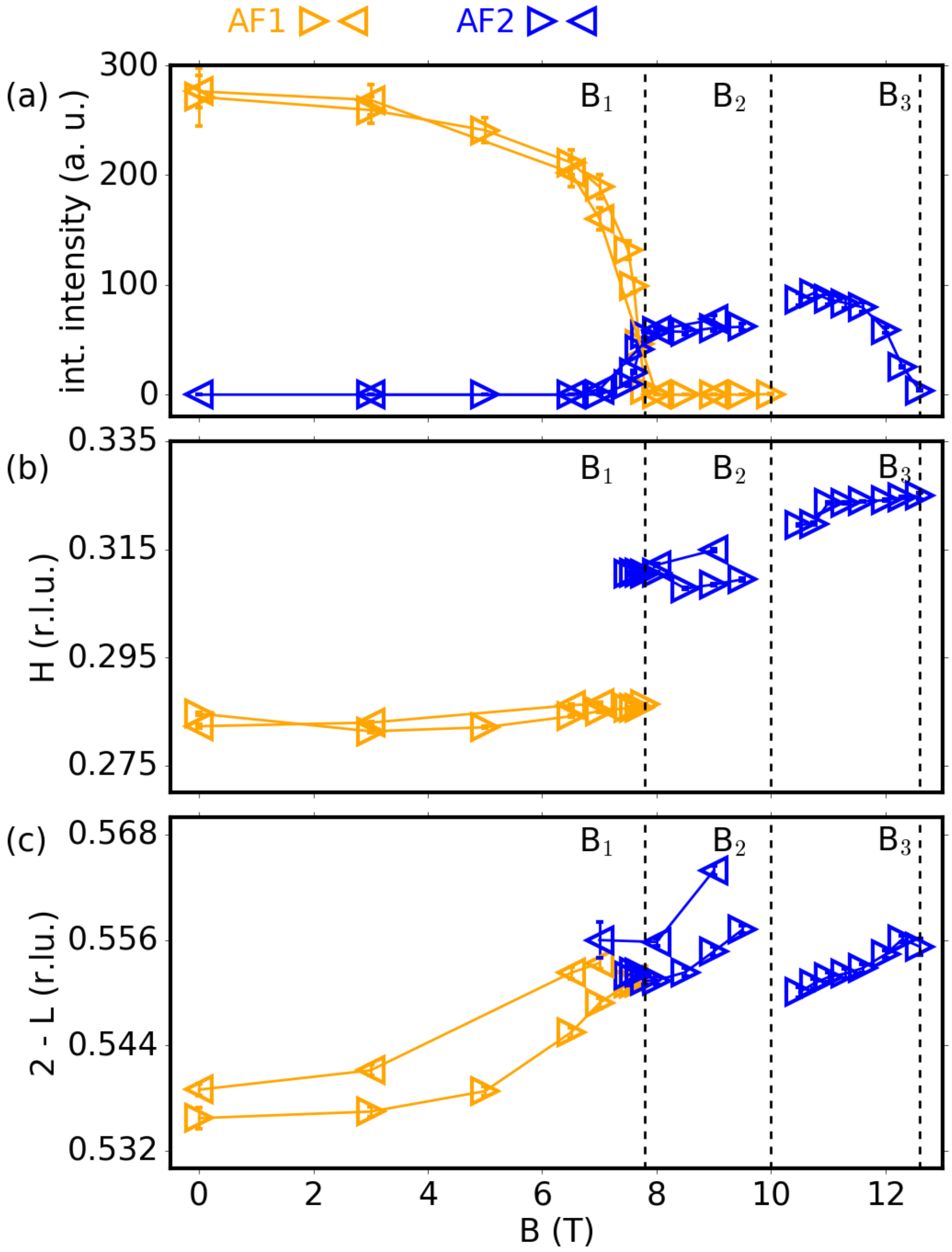

FIGURE 4.11: Magnetic field dependence of the (H H L) magnetic Bragg peak of the AF1 phase and AF2 phase measured with increasing (▹) and decreasing field (◃). Indicated are also the positions of the magnetic transition fields B_1, B_2 and B_3. The region between B_1 and B_3 may be divided into a low-field region with AF2 and a region with a modified AF2 from B_2 and B_3. Data taken on D23. T = 0.03 K.

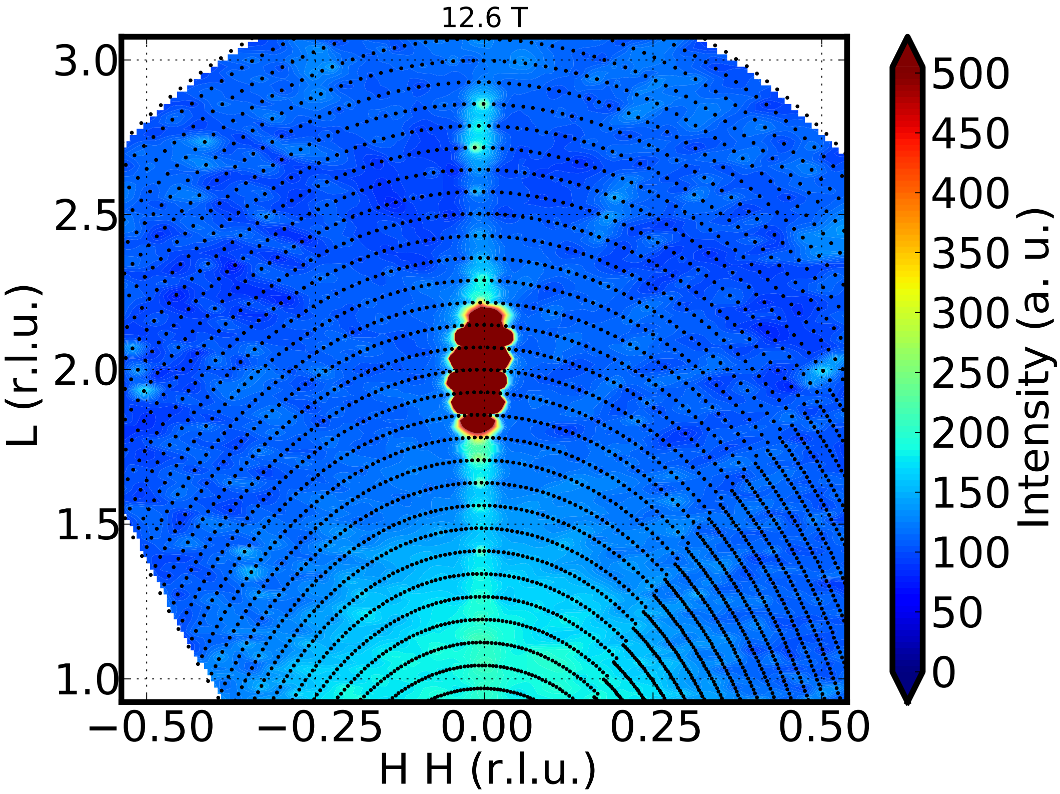

FIGURE 4.12: Intensity map at 12.6 T obtained from rocking scans. Data taken on D23.

At B_3 = 12.6 T the integrated intensity related to the incommensurate structure AF2 has vanished completely. Fig. 4.12 shows the intensity map at 12.6 T covering the entire Brillouin zone in the [110]/[001] scattering plane. One can see that no sign of magnetic satellites are recognizable at 12.6 T. The very weak intensity at (0 0 2.78) does not correspond to magnetic order as it is of nuclear origin.

This demonstrates that above B_3 there is no magnetic order with a propagation vector of the type (h h l). The absence of magnetic satellites can be interpreted in different ways. A change to a propagation vector that is not of the type (τ_h τ_h τ_l) is possible as well as the depopulation of the domains producing the magnetic satellites in the [110]/[001] scattering plane. Another, yet unlike possibility, is that the structure is collinear with moments in [001] direction as this would produce zero intensity on the L axis.

The magnetic field dependence of the integrated intensity and sample rotation ω of the nuclear Bragg peaks is shown in Fig. 4.13. Compared to the uncertainty of the measurement, a small but systematic increase in the integrated intensity with rising magnetic field is observed for all four investigated nuclear Bragg peaks. This increase is compatible with a ferromagnetic component of μ_{FM} = 0.3 μ_B, in agreement with the magnetization data.

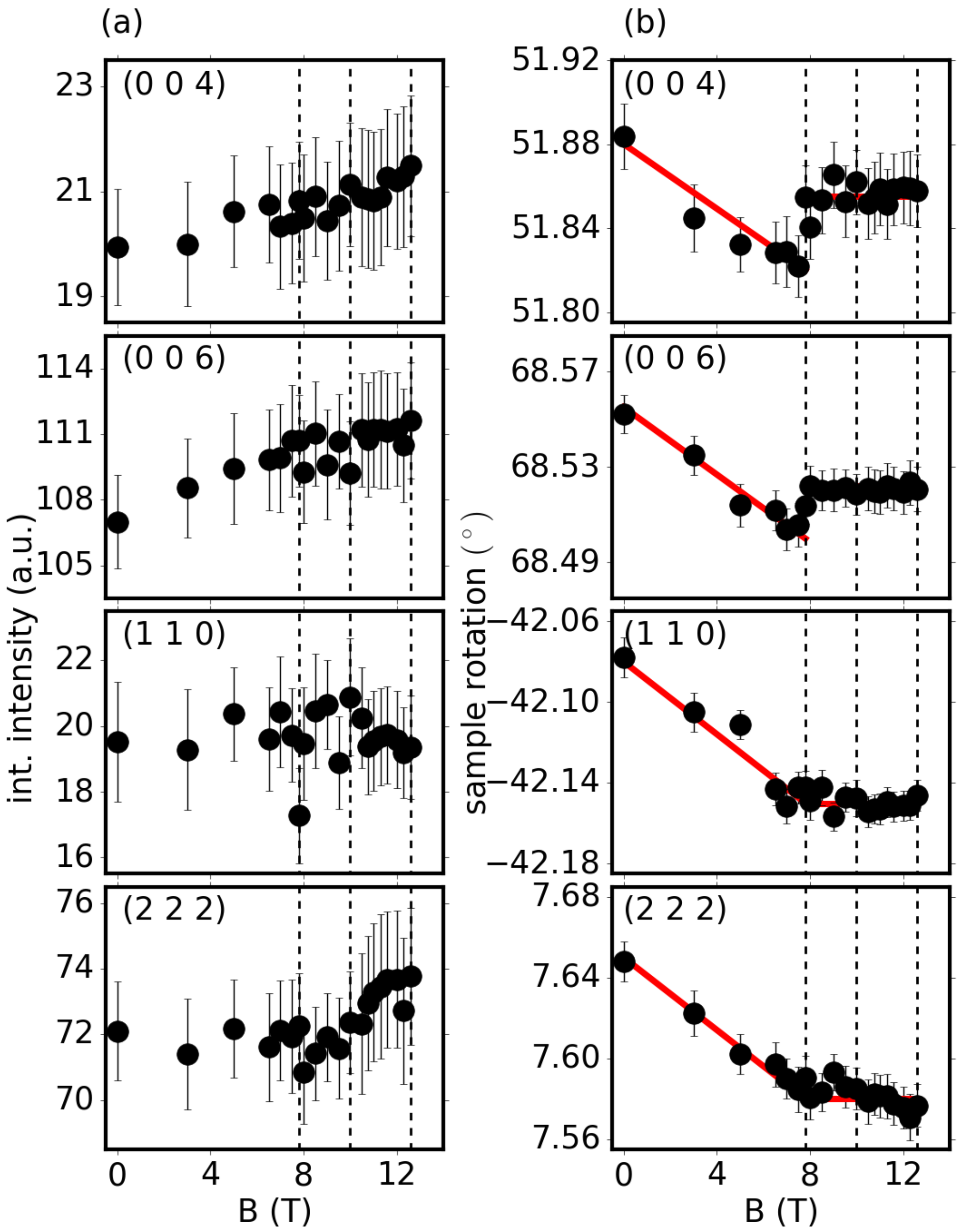

FIGURE 4.13: Magnetic field dependence of the (004), (006), (110) and (222) nuclear Bragg peaks measured at D23. a) integrated intensities, b) sample rotation angles. The dashed lines represent B_1, B_2 and B_3. T = 0.03 K.

A linear shift in ω occurs from zero field up until B_1 = 7.8 T. From there on, up to the highest magnetic field at 12.6 T, ω stays constant. For (004) as well as (006) a jump in ω is present at B_1 while for (110) and (222) one observes a kink. The change in rotation angle is practically the same in value and direction for all four nuclear Bragg peaks in the AF1 phase and may therefore be an artifact of the experiment (rotation of the sample rod due to magnetic forces?). However, there is no sample rotation in the AF2 phase. At the moment, it is not possible to give an unambiguous explanation of this behavior. The magnitude of the change in position corresponds to approximately 0.013 r.l.u..

4.2.2 Mapping of the phase diagram

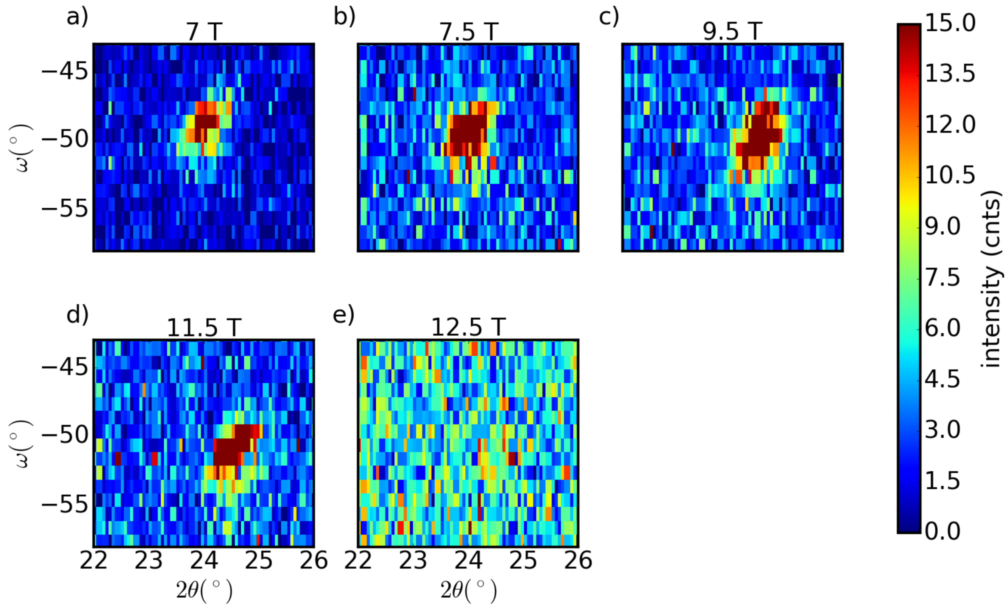

FIGURE 4.14: Field dependence of the ($-\tau_h$ $-\tau_h$ $2-\tau_l$) magnetic satellite (projected in 2Θ-ω space) at T = 0.3 K close to B_1, B_2 and B_3. No normalization of the data was applied.

The data obtained at 0.3 K, were projected in the 2Θ-ω plane (Fig. 4.14). At 7 T and 7.5 T, the peak is still close to its zero field position (2Θ, ω) = (23.9°, -48.5°) (Q $\approx$ (-0.28 -0.28 1.45)). The peak appears to be broadened at 7.5 T compared to 7 T, which points towards coexistence of AF1 and AF2 . Then at 9 T, an abrupt change to (2Θ, ω) = (24.1°, -50.8°) (Q $\approx$ (-0.31 -0.31 1.44)) is present. The positions remains virtually unchanged (see 11.5 T), until it has vanished at 12.5 T. The results are in accordance with the low temperature experiment, except here the modification of the propagation vector at B_2 is not observed. This discrepancy becomes more clear when considering

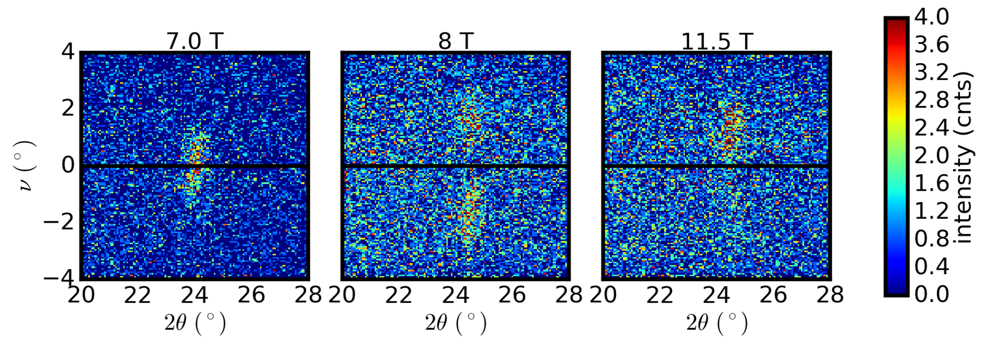

FIGURE 4.15: (-τ_h -τ_h 2-τ_l) magnetic satellite projected in 2Θ-ν space at T = 0.3 K and a) B = 7 T, b) B = 8 T, c) B = 11.5 T. Data from E4. The horizontal line marks the scattering plane.

scattering outside the scattering plane (Fig. 4.15). For 7 T, the peak is clearly confined to the scattering plane (ν = 0). At 8 T, the peak splits to $\nu \approx \pm 1.5°$. The lower peak then disappears for $B \geq$ 10.5 T.

Under concideration of the component out of the [110]/[001] scattering plane, the position of the peak in reciprocal space is calculated (Tab. 4.3). For comparison, also the position with ν = 0 is included. From the depicted positions, the deduced propagation vector is $\vec{\tau}_{\mathrm{AF2}}$ = (0.34 0.27 0.55). Given the symmetry of the nuclear parent structure, the upper and lower peak can be interpreted as magnetic satellites from different domains (mirroring at the (1$\bar{1}$0)-plane). For clarity, the domains corresponding to the (-27 -0.34 1.45) and (-0.34 -0.27 1.45) magnetic satellites will be called the 'upper' and 'lower' domain in the following. Upon increasing field, populating the 'upper' domain is in favor of the 'lower' domain.

2Θ(°)	ω(°)	ν(°)	H	K	L
24.5	-50.8	0	-0.31	-0.31	1.45
24.5	-50.8	1.5	-0.27	-0.34	1.45
24.5	-50.8	-1.5	-0.34	-0.27	1.45

TABLE 4.3: Conversion of the (-τ_h -τ_h 2-τ_l) magnetic satellite position at (0.3 K, 9.5 T) from the instrument coordinate system (2Θ, ω, ν) to reciprocal space.

The temperature and magnetic field dependence of the integrated intensity and the propagation vector was estimated from the (-τ_h -τ_h 2-τ_l) magnetic satellite (Fig. 4.16, Fig. 4.17 and Fig. 4.18. The position in (2Θ, ω, ν)-space is fitted from projections on the respective variable and then transformed to reciprocal space. At low temperature ($T <$ 2 K), in the AF1 phase as well as in the AF2 phase, no field or temperature dependence of the propagation vector is recognizable within the uncertainty. For 1 K, the decrease of the intensity to the AF2 'lower' peak at B_3 in favor of the 'upper' peak weakens. For $T >$ 1 K it is not observed.

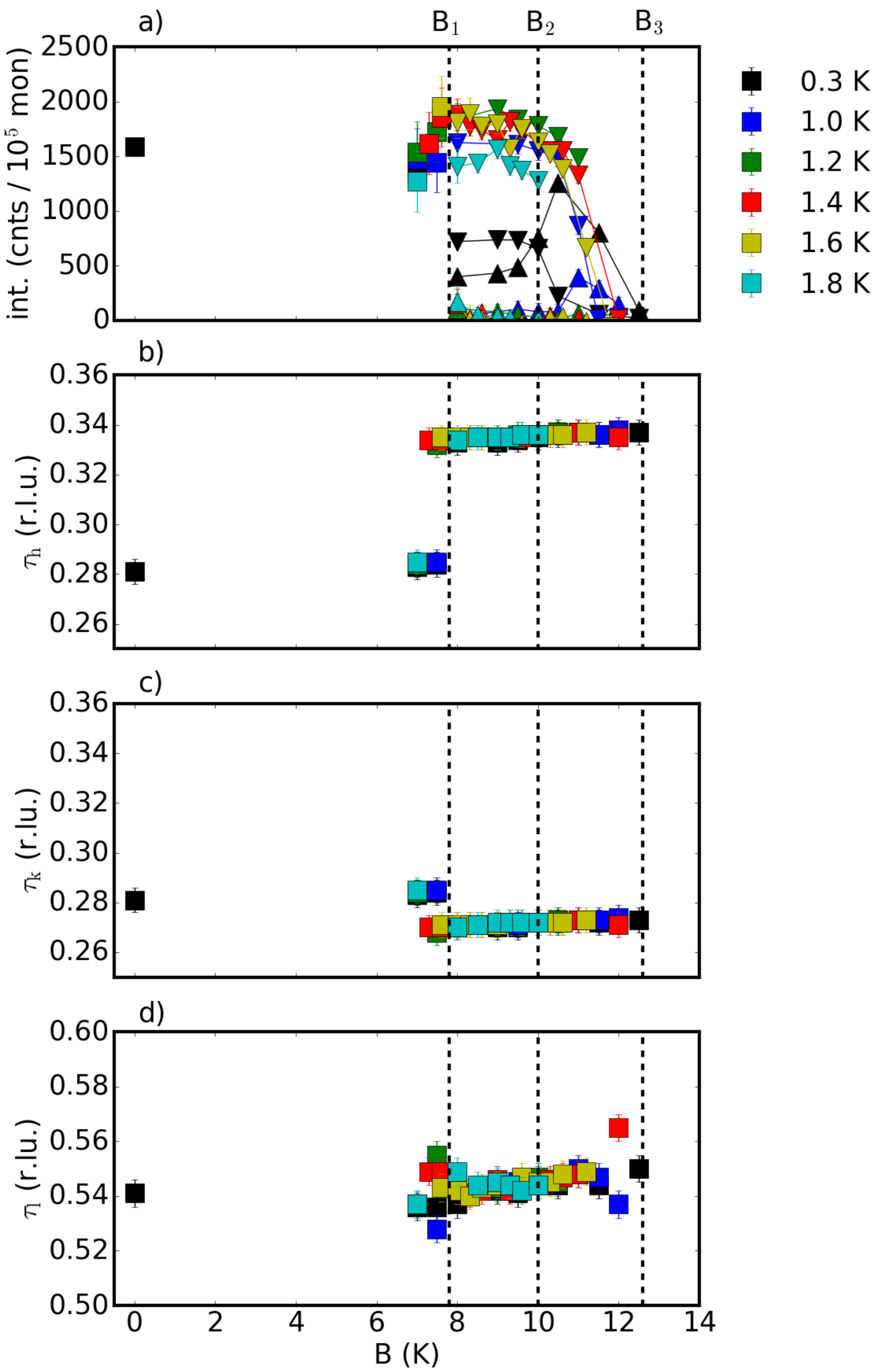

FIGURE 4.16: Magnetic field dependence of the integrated intensity of the (-τ_h -τ_h 2-τ_l) magnetic Bragg peak and the propagation vector at low temperature ($T < 2$ K). In the intensity plot, squares (■) mark the peak in the AF1 phase and up (▲) and down (▼) triangles the AF2 'upper' and 'lower' peak.

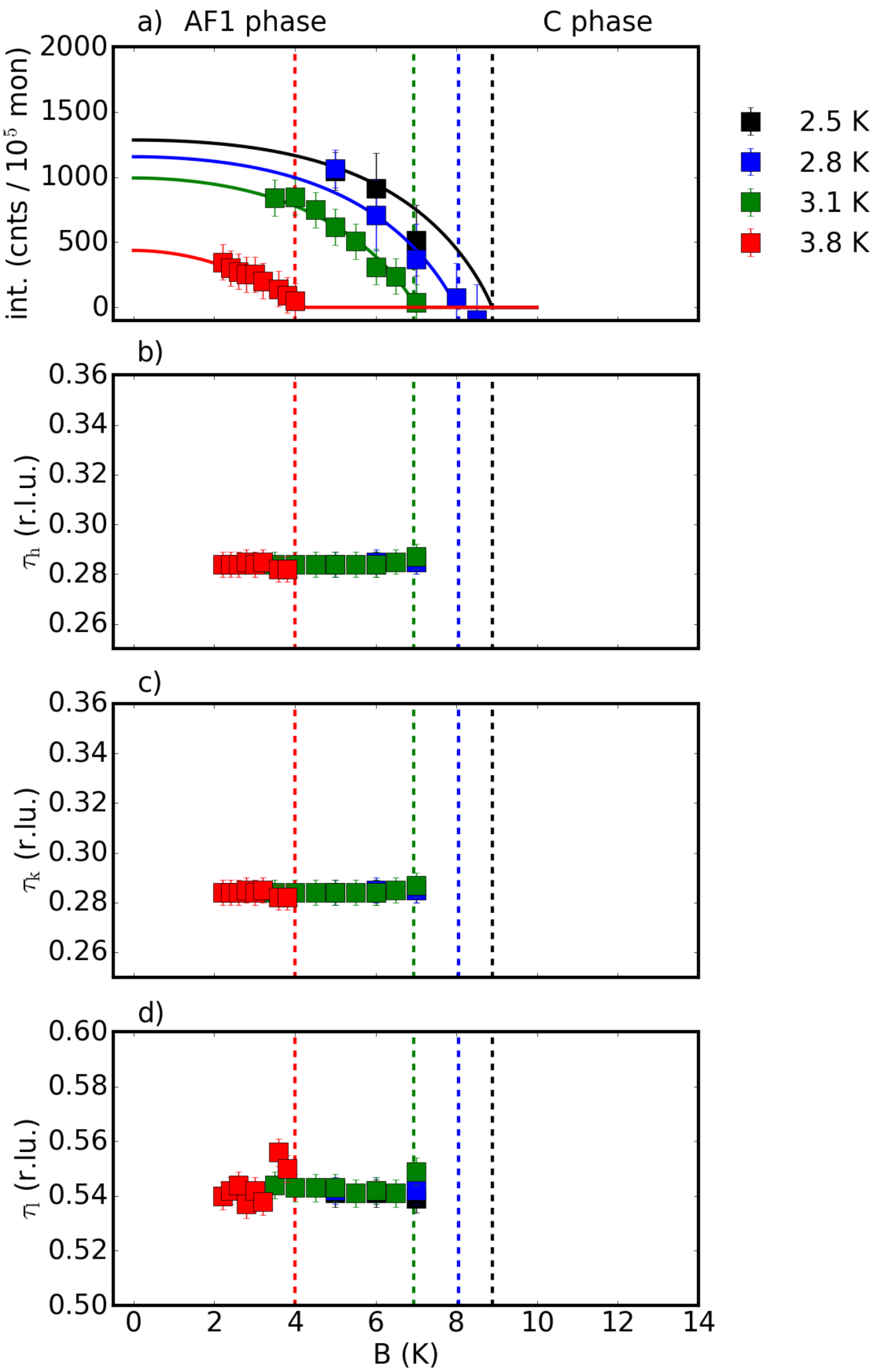

FIGURE 4.17: Magnetic field dependence of the integrated intensity of the ($-\tau_h$ $-\tau_h$ $2-\tau_l$) magnetic Bragg peak and the propagation vector at high temperature ($T > 2$ K). The lines describing the intensity corresponds to Eq. 4.9 with the parameters given in the text. B_C is indicated by the dashed lines.

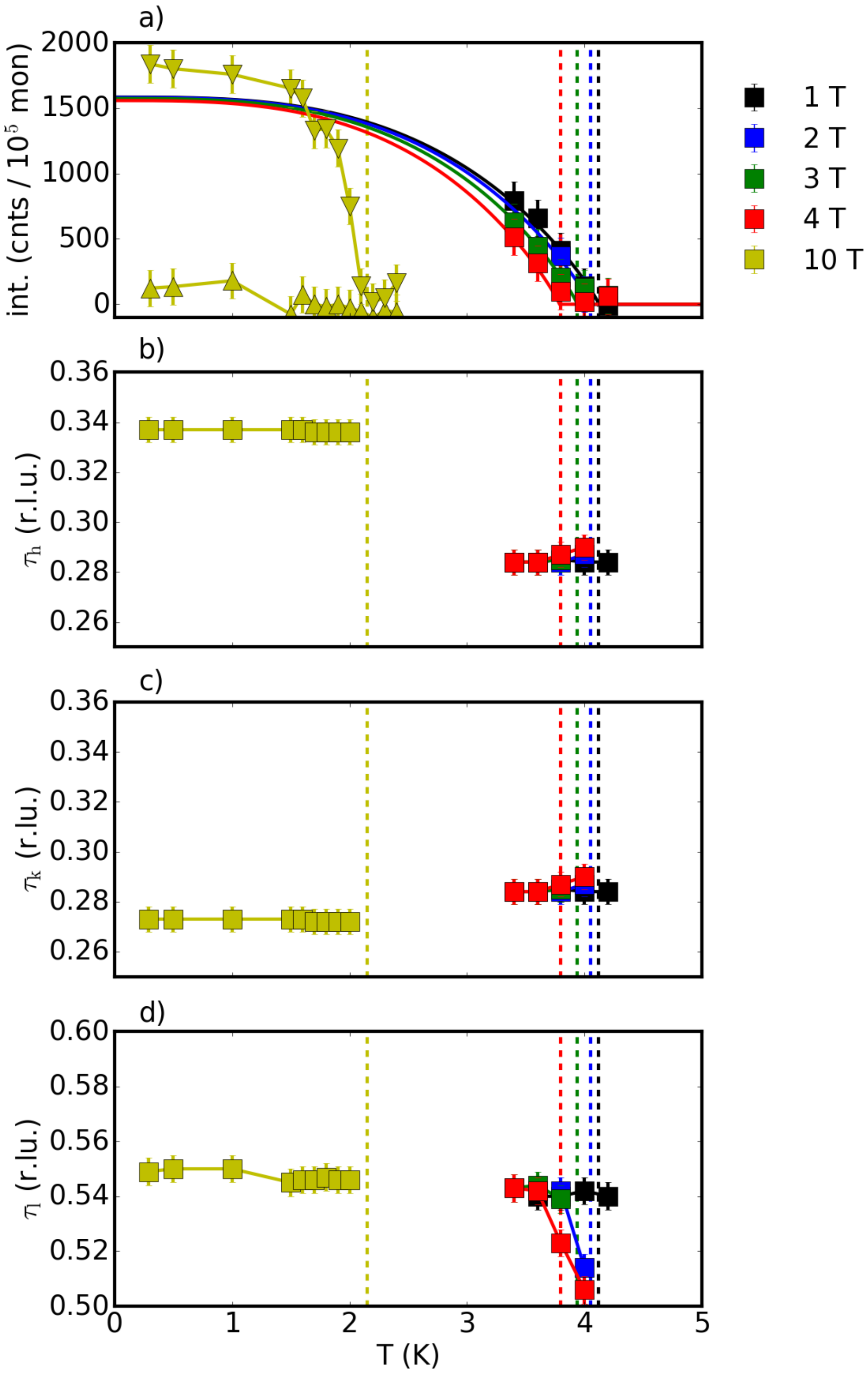

FIGURE 4.18: Temperature dependence of the integrated intensity of the (-τ_h -τ_h 2-τ_l) magnetic Bragg peak and the propagation vector. The lines describing the intensity corresponds to Eq. 4.9 with the parameters given in the text. T_{AF1} is indicated by the dashed lines. In the intensity plot, squares (■) mark the peak in the AF1 phase and up (▲) and down (▼) triangles the AF2 'upper' and 'lower' peak.

Close to T_N in AF1, the τ_l component decreases, approaching the commensurate value 1/2 at T_N. For the propagation vector in the AF2 phase, no temperature dependence is present.

While at low temperature the phase transition at B_1 is considered of first order, the situation for low field and high temperature is not so obvious. The decline of the intensity started already somewhat away from the phase boundary. This would point towards a 2nd order transition. If the transition is of 2nd order, a power law should give a well description of the intensity. Therefore, it was attempted to fit

$$I = I_0[1 - (T/T_{\mathrm{AF1}})^{\alpha_T}]^{2\beta_T}[1 - (B/B_C)^{\alpha_B}]^{2\beta_B} \tag{4.9}$$

where the relations

$$T_{\mathrm{AF1}}(B) = T_{\mathrm{AF1}}(B = 0T) - aB^n \tag{4.10}$$

$$B_C(T) = \left(\frac{T_{\mathrm{AF1}}(B = 0T)}{a}\right)^{1/n} \tag{4.11}$$

were assumed. Fixing $\alpha := \alpha_T = \alpha_B$ and $\beta := \beta_B = \beta_T$ results in $\alpha = 3 \pm 1$ and $\beta = 0.5 \pm 0.1$. These values are similar to the zero field values. The large uncertainty in α is most likely due to the fact that no data at low field and temperature was included. Thus, the AF1/C transition can be considered as 2nd order, while the AF2/C transition is 1st order.

From the presented data, a phase diagram was constructed (Fig. 4.19. The position in reciprocal space was used to distinguish between AF1 and AF2. At each measured (T, B)-coordinate, the colored dots indicate the presence of AF1- (blue), AF2-satellites (red/yellow) or neither of them (white). The presence of the 'up' and 'down' peaks are separately marked. Coexistence is marked by half filled dots. Solid lines correspond to first order transitions, while dashed line correspond to 2nd order transitions. The transition lines are adopted from [65].

To fit the phase boundaries, the curvature of the AF2/C transition line was increased. The existence of a modified AF2 phase (called AF2mod in [65]) above B_2 was not confirmed. A critical end point at ≈ (3.5 K, 4 T) as suggested in [64] for the phase diagram with B||[100] was not observed. The first order nature of AF1/AF2 and AF2/C contradicts the presence of a QCP at 7.8 T or 12.6 T. In view of the B||[100] phase diagram from [65], if a field quantum critical point is present, it is expected at $B_{\mathrm{QCP}} \approx 30$ T .

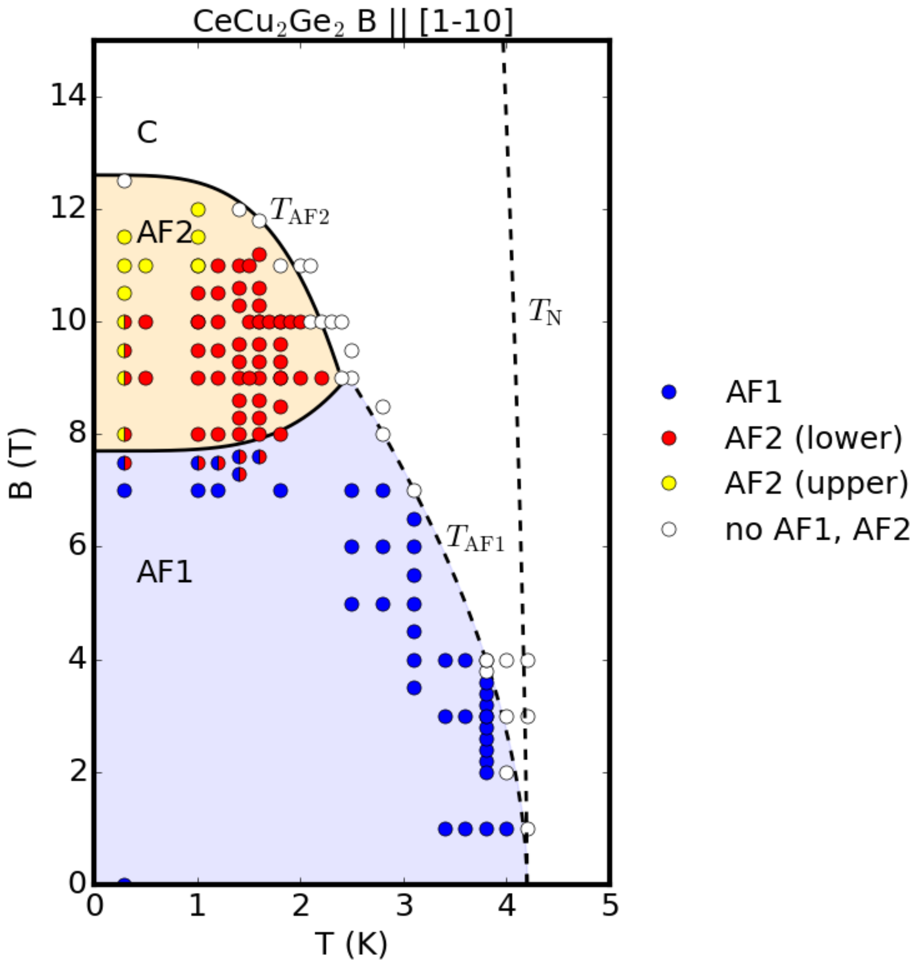

FIGURE 4.19: Phase diagram of $CeCu_2Ge_2$ with magnetic field in $[1\bar{1}0]$ direction constructed from neutron data.

The shape of the AF1 and AF2 phases is similar to what is expected for a spin-flop transition, i.e. extrapolating T_{AF2} gives T_{AF2}(B = 0 T) $\approx$ 3 K $<$ T_{AF1}(B = 0 T) and B_1 is just below the B_{C}, where $T_{\mathrm{AF1}} = T_{\mathrm{AF2}}$. This points toward competition between the AF1 phase and AF2 phase.

4.2.3 AF2 structure

The integrated intensity of the smallest nuclear Bragg peak, i.e. (004), was used to estimate the ferromagnetic component induced by the magnetic field. It was assumed that no ferromagnetic component is present in zero field and that the ferromagnetic moments are equally distributed on the Ce sites. Jana2006 was used to simulate the additional magnetic intensity for a ferromagnetic moment of $1\mu_B$ in field direction. Using the proportionality $I_{mag} \propto \sqrt{\mu}$, the experimentally observed additional intensity was related to the magnetization. The uncertainty is still relatively large despite the long

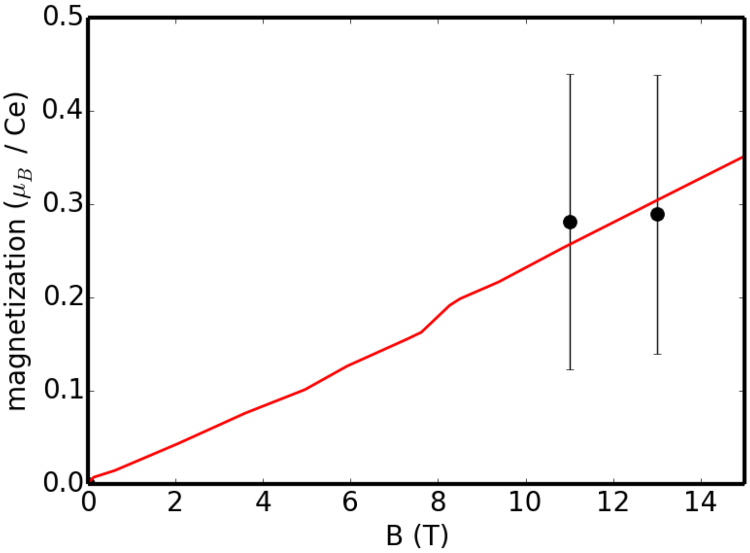

FIGURE 4.20: Magnetization of $CeCu_2Ge_2$ in magnetic field (B $||[1\bar{1}0]$) extracted from the (004) magnetic intensity (black dots) and from [63] (red line).

counting time ($\approx$ 1 h), because the nuclear contribution is much stronger ($I_{mag}/I_{nuc} \approx$ 3 %). At 11 T, a ferromagnetic component μ_{fm} = 0.28 μ_B is present. The values are in agreement with the magnetization measured in [63].

The best fit (R = 10.28 %) was obtained using model A1 from the zero field structure. The ordered moment was found to be $\mu_{ord}^{AF2, SDW} = (1.6 \pm 0.7)\ \mu_B$. This appears, even with the relatively large uncertainty, to be too large compared to $\mu_{ord}^{1\text{-}k}$ 1.0 μ_B for the zero field structure, the saturation value of the magnetization in [63] and $\mu_{CEF} = 1.55\ \mu_B$ expected from the crystal electric field. The R-value is worse than for the AF1 structure, but on the same order of magnitude. This hints, that the A1 model is close to the real magnetic structure, but something is still missing. To accound for the too large moment, an additional component for the magnetic moments is added. In its most general form the magnetic structure is described by

$$\vec{\mu}_n = \vec{\mu}_1 \cos\left(\vec{\tau} \cdot \vec{r}_n\right) + \vec{\mu}_2 \sin\left(\vec{\tau} \cdot \vec{r}_n\right) \tag{4.12}$$

$\vec{\mu}_1$ was fixed in the $[1\bar{1}0]$ direction, therefore maintaining one component from the A1 model. No restriction for $\vec{\mu}_2$ was applied. The fitting yielded a reasonable R = 8.35 % with $|\vec{\mu}_2| = (0.7 \pm 0.1)\mu_B$ and $\vec{\mu}_2 \parallel [001]$. Also the obtained value $|\vec{\mu}_1| = (1.0 \pm 0.1)\mu_B$ resembles the value of the zero field structure. As $|\vec{\mu}_1| \neq |\vec{\mu}_2|$, the helix is of the elliptical type. The refined AF2 structure is pictured in Fig. 4.22 in a similar way as for the AF1 structure. Note that the propagation vector was approximated to the in-scattering plane value (0.31 0.31 0.55) for clarity in this drawing.

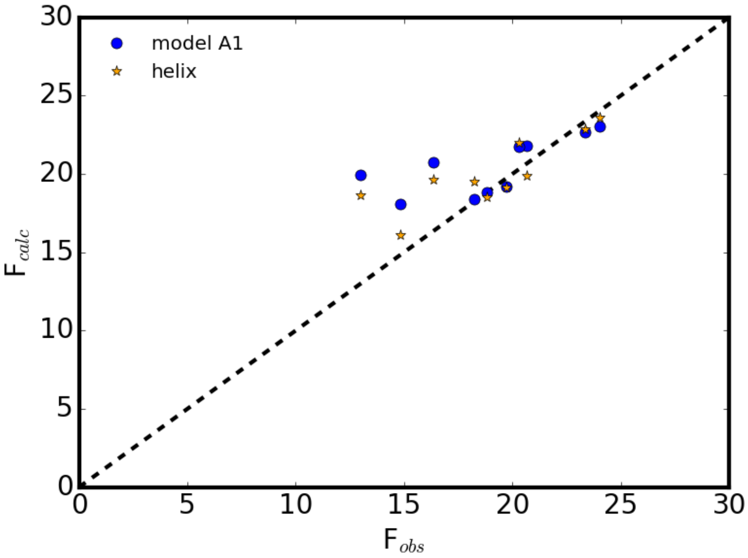

FIGURE 4.21: Plot of the calculated and observed magnetic structure factors for both 1-k models A1 (R = 10.28 %) as well as for a helical model (R = 8.35 %).

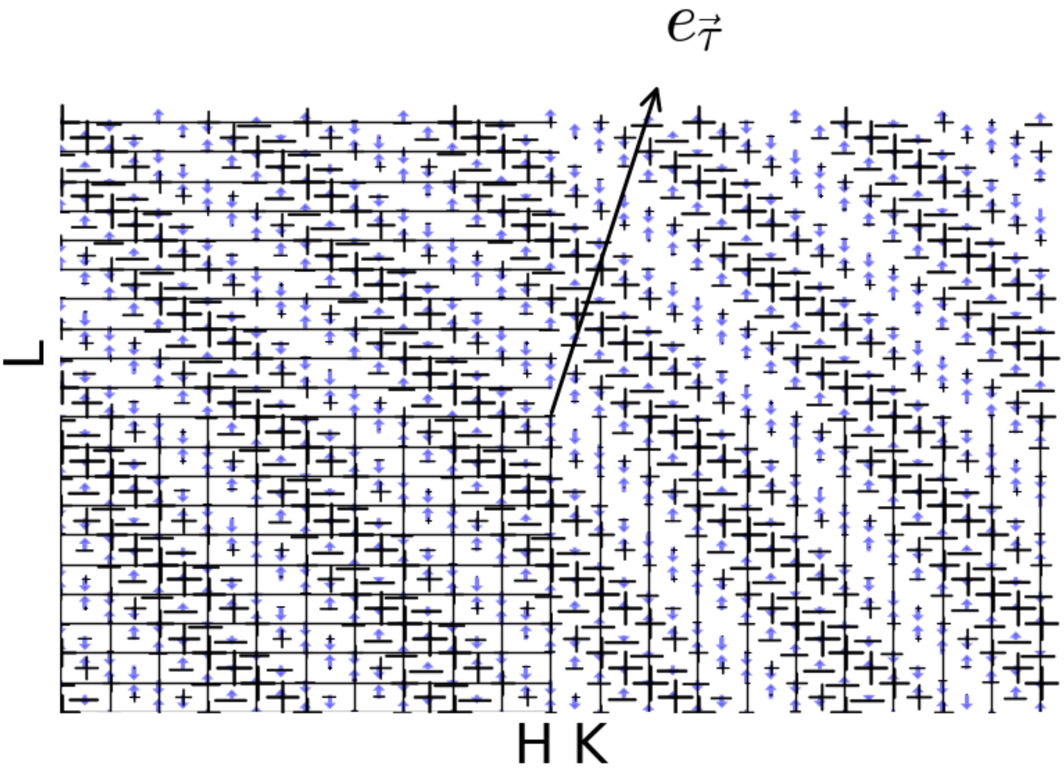

FIGURE 4.22: Drawing of the magnetic structure (model A1A1) in the plane spanned by [110]/[001]. The $\vec{\mu_1}$ components point out of the plane of projection. Their directions are indicated by '+' or '-' and the moment size is represented by the size of the symbols. $\vec{\mu_2}$ is represented by the blue arrows.

4.2.4 Competition of the AF1 and AF2 phase

The initial goal was to find competing short range order corresponding to the unknown magnetic order of the C-phase. The $CeCu_2Ge_2$ single crystal was cooled down to 3 K. The presence of the expected AF1 order with $\tau_1 \approx$ (0.28 0.28 0.55) was confirmed. The sample was then heated to 5 K slightly above the Néel temperature T_N. Scans over the in plane sample rotation were performed cutting through positions corresponding to the AF1 and AF2 phase, i.e $\vec{Q}_1$ = (0.28 0.28 1.46) and $\vec{Q}_2 \approx$ (0.31 0.31 1.47). Both scans are shown in Fig 4.23. At both positions, a signal well above the background is present. The intensity is three orders of magnitude smaller than the intensity from the magnetic satellite of AF1 at 3 K. Both signal are equally strong as the integrated intensities are I_1 = (270 $\pm$ 30) cnts/33 min and I_2 = (240 $\pm$ 40) cnts/33 min. Further mapping along (0.9 ... 1.8 0 0) did not reveal any further short range order.

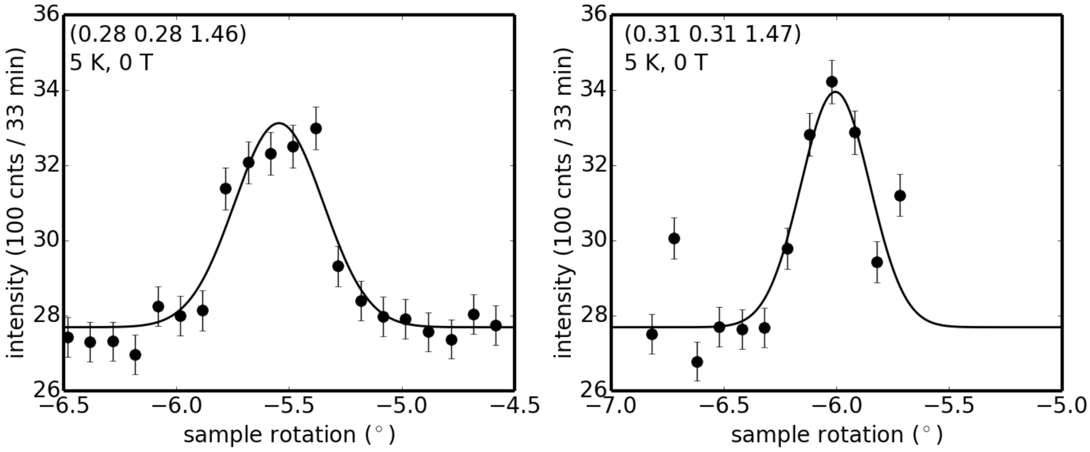

FIGURE 4.23: Scans over the in plane sample rotation at $\vec{Q}_1$ = (0.28 0.28 1.46) (left) and $\vec{Q}_2$ = (0.31 0.31 1.47) (right) slight above T_N (5 K). The black line is a Gaussian shaped fit.

The excistence of short range order can be interpreted as competition between the two different magnetic ordered states AF1 and AF2 before magnetic order of one type is established. Modulated magnetic structures, such as spin-density-waves as in AF1 or helices as in AF2 are known to be formed by nesting of the Fermi surface [19]. For $CeCu_2Ge_2$, band structure calculations revealed a nesting vector of the Fermi surface in line with the AF1 propagation vector [43]. Further exploration of possible nesting with $\vec{\tau}_{AF2}$ = (0.34 0.27 0.55) by calculation or measurement of the electronic band structure would be highly desirable.

4.2.5 Summary

At low temperature, the zero field phase AF1 undergoes a first order phase transition to the AF2 phase. In this phase, splitting of the magnetic satellites out of the [110]/[001] plane is observed. The corresponding new propagation vector is $\vec{\tau}_{\mathrm{AF2}}$ = (0.34 0.27 0.55). The magnetic order in AF2 is best described by an elliptical helix with $|\vec{\mu}_1|$ = $(1 \pm 0.1)\mu_B$ ($\vec{\mu}_1$ || [1$\bar{1}$0]) and $|\vec{\mu}_2|$ = $(0.7 \pm 0.1)\mu_B$ ($\vec{\mu}_2$|| [001]). At 12.6 T, all accessible AF2 satellites eventually vanish. No new magnetic satellites could be detected. The nature of this phase remains therefore unknown. At high temperature (T $>$ 2 K), the satellites of the AF1 phase vanish in a second order phase transition. Here, the AF1 phase is not succeeded by AF2. The occurrence of AF1 and AF2 magnetic satellites as well as their respective absence was illustrated in a phase diagram. The transition lines agree well with macroscopic measurements. The phase diagram as well as the existence of short range correlations at the positions corresponding to AF1 and also AF2 at T $>$ T_{N} indicate competition of the AF1 and AF2 phases.

4.3 Magnetic excitations

In this section, the results on the magnetic excitations in $CeCu_2Ge_2$ are presented. First the model, based on a single site interaction for the Kondo effect and an inter-site interaction for the RKKY interaction is described . Based on this model the spin wave dispersion is fitted, yielding the next nearest neighbor RKKY interactions $2SJ_1$ = (-0.042 ± 0.007) meV (basal plane) and $2SJ_2$ = (-0.18 ± 0.01) meV (body diagonal). This results are then used for a comparison to the superconducting $CeCu_2Si_2$ and the paramagnetic $CeNi_2Ge_2$. It was found that the interaction in the basal plane increase with the hybridization. Afterwards, the temperature dependence of the excitation spectrum is given, which is consistent with a 2nd order phase transition at T_N. Finally, the magnetic field dependence of the excitation spectrum is reported. In magnetic field, Zeeman splitting of the spin-wave excitation is observed. The effective Landé factors due to the RKKY character of the excitation $g^{\mathrm{eff}} = 0.36$ in AF1 and $g^{\mathrm{eff}} = 0.525$ in AF2 are obtained.

4.3.1 Model for the magnetic excitations

To model the magnetic excitation spectrum, a quasi elastic contribution for local fluctuations due to Kondo effect and a spin wave excitation for inter-site interaction is assumed. This approach was previously successfully employed for other HF systems [115; 116; 114; 117]. Using Eq. 3.38 in Eq. 3.37, the scattering function for the quasi elastic becomes

$$S_{qe}(\vec{Q}, E) = \frac{1}{1 - e^{-E/k_B T}} \chi_{\mathrm{qe}} E \frac{1}{\pi} \frac{\Gamma_{\mathrm{qe}}}{E^2 + \Gamma_{\mathrm{qe}}^2} \tag{4.13}$$

χ_{qe} is the static susceptibility given in arbitrary units and Γ_{qe} is the FWHM related to the local fluctuations. A particular problem arises as these two types of excitations are on a similar energy scale. Near Q_{AF}, the quasi-elastic intensity was covered by the much stronger intensity of the spin wave excitation. To overcome this, the sample was rotated away from $\vec{Q}_{\mathrm{AF}}$ to $\vec{Q}$ = (0.1 0.1 1.7) while keeping the scattering angle approximately constant. Even here, two features are observable (Fig. 4.24). The narrow feature corresponds to spin wave modes. As magnetic Bragg peaks exists at all $\vec{Q}_{\mathrm{AF}} = (G_h \pm \tau_h\ G_k \pm \tau_h\ G_l \pm \tau_l)$ ($\vec{G} = (G_h\ G_k\ G_l)$ is the nuclear zone center), spin wave modes originate at all those $\vec{Q}$s. At $\vec{Q}$ far away from those $\vec{Q}$s, the spin wave modes overlap in a single excitation. The position is consistent with the previous powder results [35] and the results on the spin wave dispersion obtained in this work. The broad feature on the

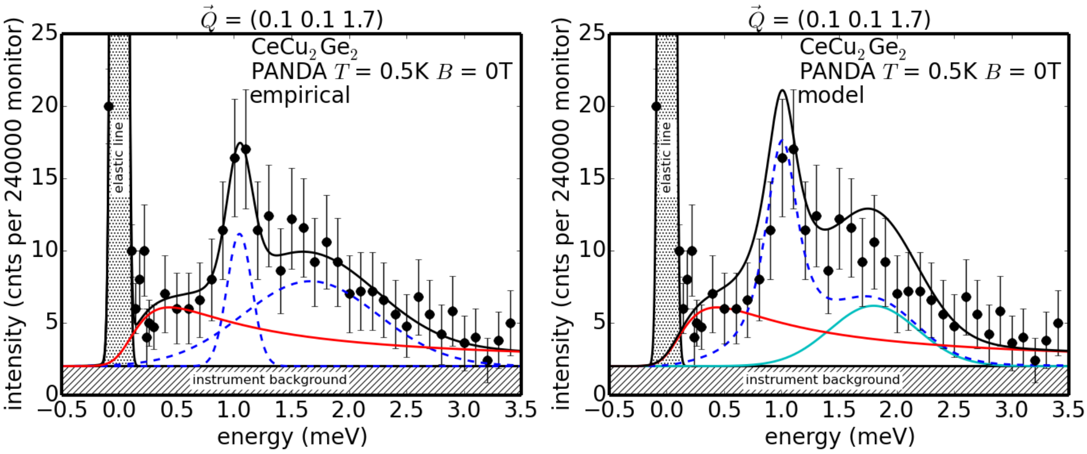

FIGURE 4.24: Constant-$\vec{Q}$ = (0.1 0.1 1.7) scan with approximately same scattering angle as $\vec{Q}_{AF}$ to determine background. The red line is the quasi elastic contribution, while the dashed blue lines correspond to the spin wave excitations, fitted with an empiric approach using two gaussians (left) and the spin wave model (right). The cyan line is the constant gaussian at 1.8 meV with FWHM 0.9 meV.

other hand can not be explained in terms of spin wave modes: the energy scale of the center and FWHM exceeds the order of magnitude of the intersite interactions set by the the Néel-temperature. It is further independent of $\vec{Q}$ and decreases upon heating (see temperature dependence). It can not be ruled out that this feature corresponds to magnetic scattering of an impurity phase. Therefore, a constant gaussian is added to each measured spectrum at 1.8 meV with FWHM 0.9 meV.

As most of the high energy tail of the quasi elastic is covered, the width was set to Γ_{qe} = k_B T_K with T_K = 5.1 K from [40]. The scale of the quasi elastic was left as a free parameter and the fit yielded $\chi_{qe} = 27 \pm 13$. To fit the remaining data, the parameters for the quasi elastic were then kept constant, if not stated otherwise.

Choosing an adequate model for the spin-wave is not so obvious. A well established framework is linear spin wave theory [118; 119; 120; 121; 122]. However, rigorous application to incommensurate magnetic structures as for $CeCu_2Ge_2$ is a highly non trivial task [123]. Therefore, the magnetic structure is approximated using a simple two sublattice model with spins of the sublattices pointing in opposite directions. Approximating the infinite number of sublattices of the incommensurate structure just by two sublattices may appear too crude on a first glance. However, the spins still maintain their collinear alignment as well as the either parallel or anti parallel application of external magnetic field along [1$\bar{1}$0]. The two sublattice model was also successfully used for the isostructural $CePd_2Si_2$ [114].

The Hamiltonian for such a system is given as

$$H = -J \sum_{j,j'}^{N/2} \hat{\vec{S}}_j \cdot \hat{\vec{S}}_{j'} + g\mu_\mathrm{B} B \sum_{j}^{N/2} \hat{S}_j^z - g\mu_\mathrm{B} B \sum_{j'}^{N/2} \hat{S}_{j'}^z \tag{4.14}$$

The first term represents the interaction between two sites i, j with $J < 0$ since the system is antiferromagnetic. The second and third term represent the magnetic field acting on the two sublattices. The field $B = B_\mathrm{m} + B_\mathrm{ext}$ is composed of the internal molecular field B_m and the external applied field B_ext.

Using linear spin wave theory results in the dispersion [124; 125]

$$E_q(\vec{q}) = \sqrt{[g\mu_\mathrm{B} B - 2SJ(0)]^2 - \left[2SJ(\vec{q})\right]^2} \tag{4.15}$$

where $J(\vec{q})$ is the next nearest neighbor interaction

$$J(\vec{q}) = \sum_{\vec{r}} J(\vec{r}) e^{-i\vec{q}\cdot\vec{r}} \tag{4.16}$$

$$= 2J_1 \left[\cos(2\pi q_x) + \cos(2\pi q_y)\right] \tag{4.17}$$

$$+ 4J_2 \cos\left[\pi(q_x + q_y)\right] \cos(\pi q_z) \tag{4.18}$$

and $\vec{q} = (q_x, q_y, q_z) = \vec{Q} - \vec{G} - \vec{\tau}$ is the position in reciprocal space given in reduced wavevector ($\vec{G}$ is the center of the nuclear Brillouin zone). Including also next nearest neighbors is necessary since with only nearest neighbors there would be no interaction in L direction that would result in a flat dispersion in this direction, which is obviously not the case. Note that for $\mathrm{CeCu_2Ge_2}$ the centered atom is slightly nearer to the edge atom than the atom on the opposite edge in the basal plane.

As a spectral weight function, a damped harmonic oscillator (DHO) is assumed. An over-damped harmonic oscillator as spectral weight function would result in a strong overestimation of the intensity towards higher energy. The excitation energy E_q is corrected according to [126] and the resulting spectral weight function reads as

$$F(\vec{q}, E) = \frac{1}{\pi} \frac{2\Gamma_0 (E_\mathrm{q}^2 + \Gamma_0^2)}{\left[(E - E_\mathrm{q})^2 + \Gamma_0^2\right]\left[(E + E_\mathrm{q})^2 + \Gamma_0^2\right]} \tag{4.19}$$

Therefore, the scattering function (see Eq. 3.37) becomes

$$S_{SW}(\vec{Q},E) = \frac{1}{1-e^{-E/k_B T}} E\chi_q \frac{1}{\pi} \frac{2\Gamma_0(E_q^2+\Gamma_0^2)}{\left[(E-E_q)^2+\Gamma_0^2\right]\left[(E+E_q)^2+\Gamma_0^2\right]} \tag{4.20}$$

where Γ_0 is the half-width-half-maximum of the DHO that is fixed to a constant value and the $\vec{q}$-dependent scale of the spin wave χ_q is given by the mean field expression [127]

$$\chi_q = \frac{\chi_{afm}}{1 + D\left[1 - \frac{J(\vec{q})}{J(\vec{0})}\right]} \tag{4.21}$$

D is an additional parameter to scale the $J(\vec{q})$ dependence.

The dispersion, temperature and magnetic field dependence of the excitation spectrum is then parameterized from the outlined model.

4.3.2 Spin wave dispersion

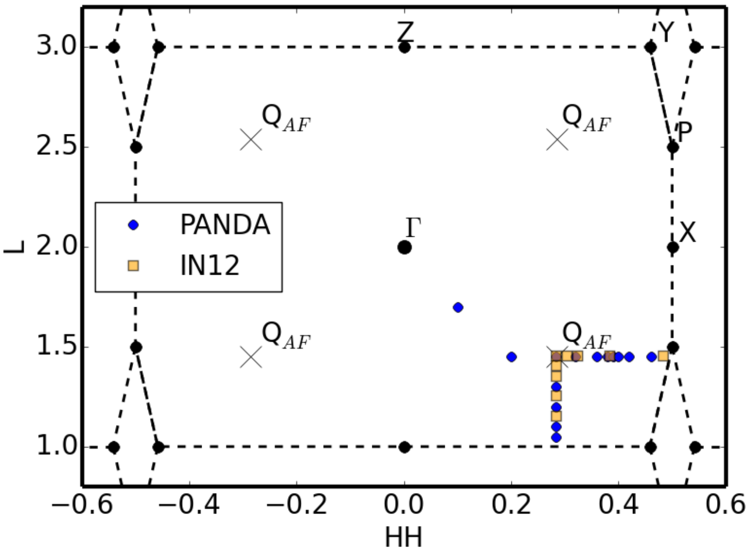

FIGURE 4.25: [110]/[001] scattering plane in reciprocal space around the (002) nuclear Bragg peak. The dashed lines mark the Brillouin zone. The magnet satellites at Q_{AF} are marked by crosses. Energy scans were performed at the position marked with blue dots (PANDA) and orange squares (IN12).

The dispersion of the spin wave was measured with constant-$\vec{Q}$ scans along HH and L direction with the sample oriented in the [110]/[001] scattering plain. The measurements were made at constant temperature (0.5 K PANDA, 0.4 K IN12) in the Brillouin zone around the (002) nuclear Bragg peak. An overview is given in Fig. 4.25. To fit the dispersion with the above developed model, the elastic part was eliminated by cutting the scans at 0.28 meV. The model was then simultaneously fitted to all remaining 421 data points of the constant-$\vec{Q}$ scans from PANDA (Fig. 4.26, 4.27 and Fig. 4.28). Since the data set from IN12 was smaller, i.e. only 211 data points, this data was not fitted. Instead, the model was simply plotted along the data with the parameters from the PANDA data (Fig. 4.29 and Fig. 4.30).

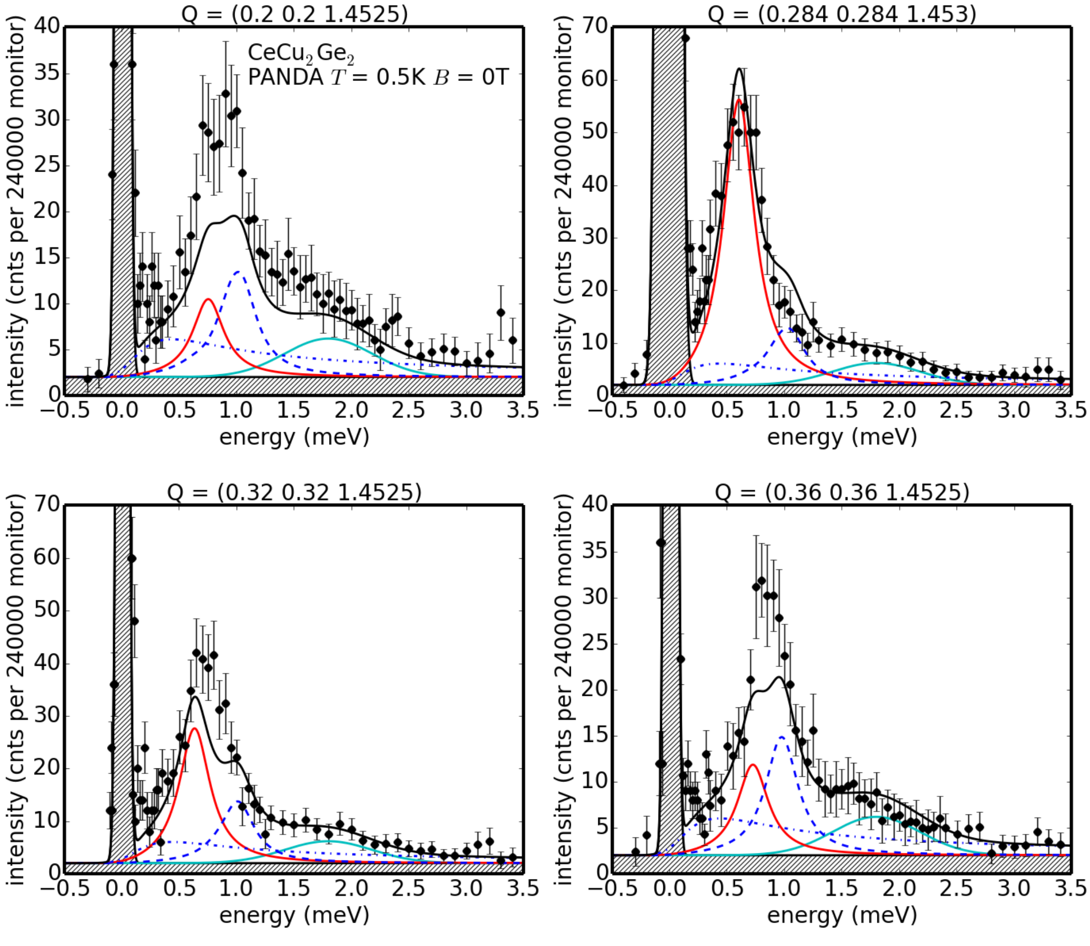

FIGURE 4.26: Constant-$\vec{Q}$ = (H H 1.45) scans (PANDA). The black line corresponds to the fitted model. The red line represents the domination spin wave excitation, while the dashed blue line corresponds to the spin wave background. The blue dash dotted line is the fixed quasi elastic. The shaded region indicates the constant background and the elastic line. The typical counting time per point is 10-20 min.

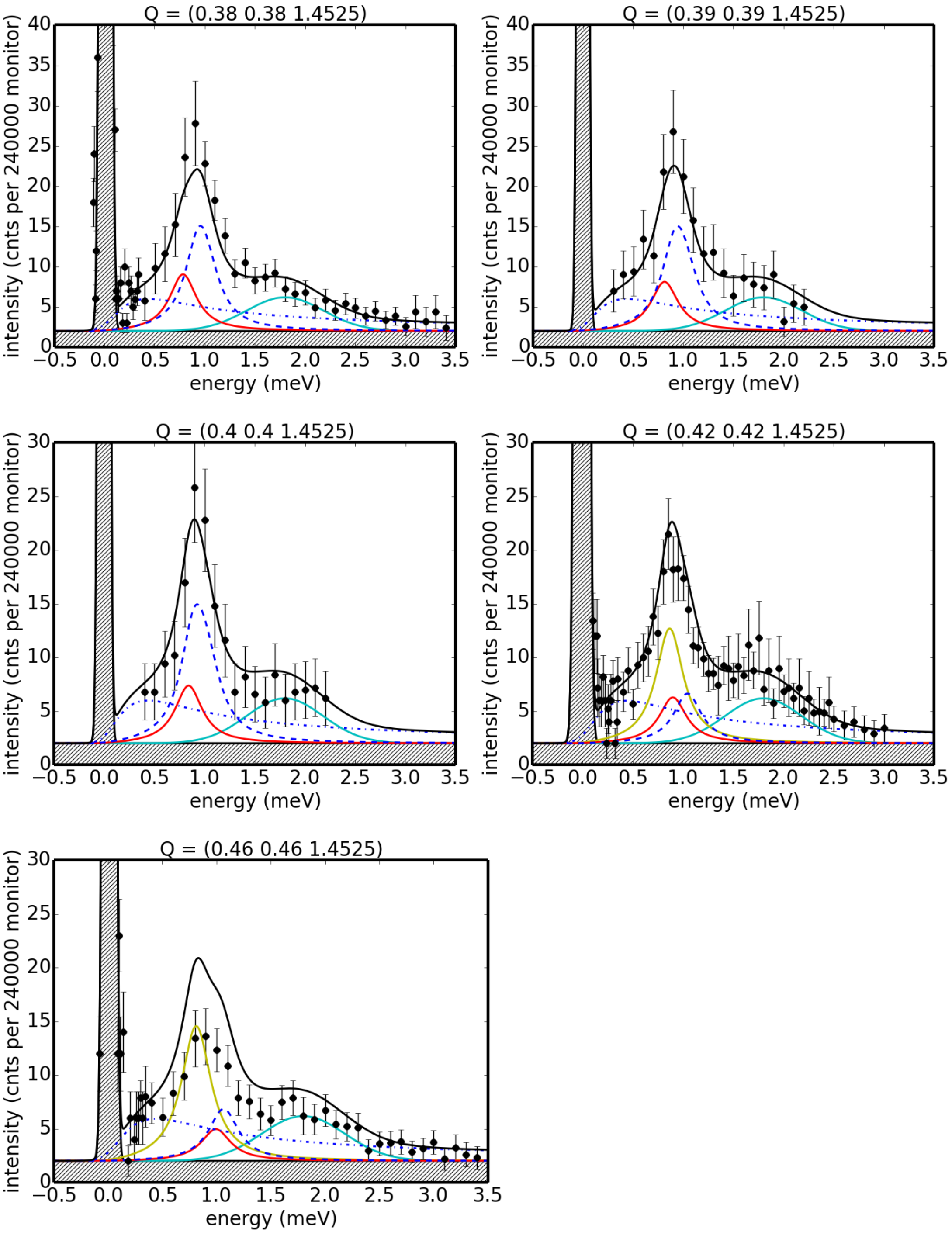

FIGURE 4.27: Constant-$\vec{Q}$ = (H H 1.45) scans (PANDA) (continued). The black line corresponds to the fitted model. The red line represents the domination spin wave excitation, while the dashed blue line corresponds to the spin wave background. The blue dash dotted line is the fixed quasi elastic. The shaded region indicates the constant background and the elastic line. The typical counting time per point is 10-20 min.

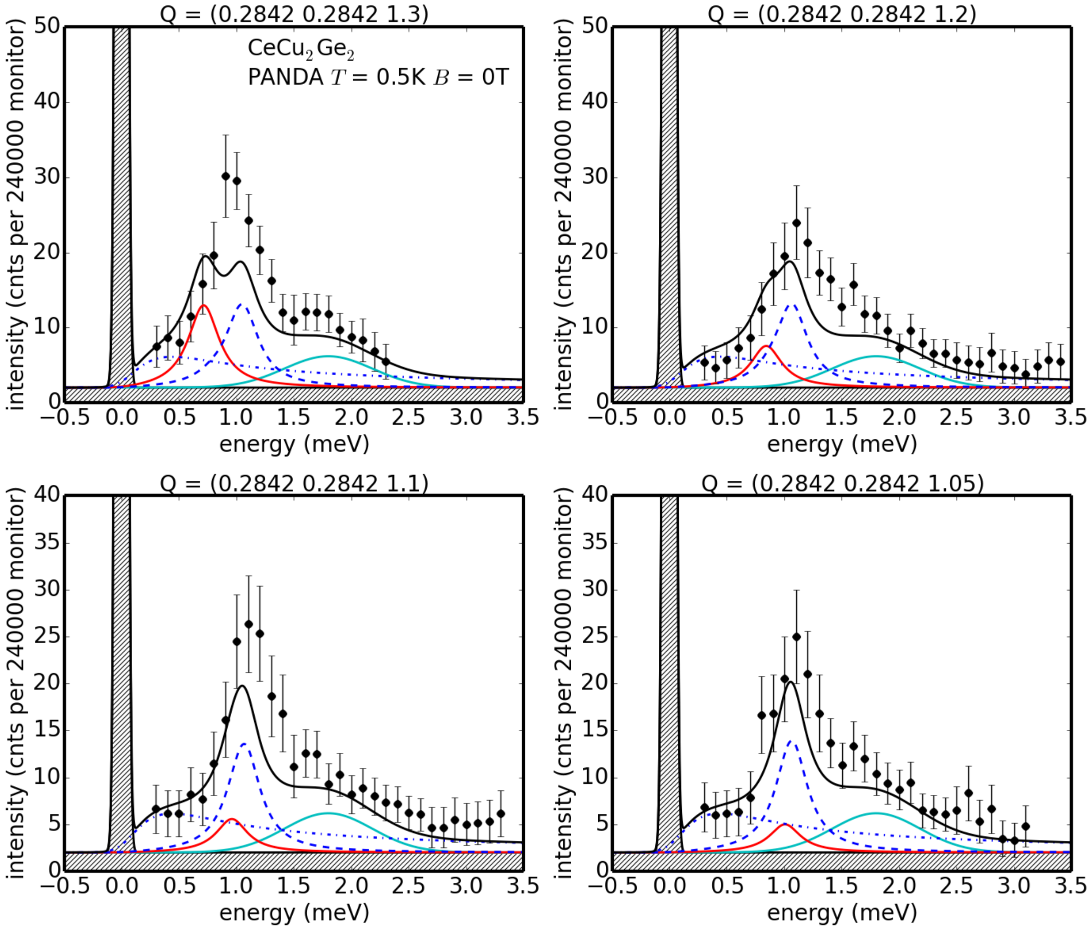

FIGURE 4.28: Constant-$\vec{Q}$ = (0.284 0.284 L) scans (PANDA). The black line corresponds to the fitted model. The red line represents the domination spin wave excitation, while the dashed blue line corresponds to the spin wave background. The blue dash dotted line is the fixed quasi elastic. The shaded region indicates the constant background and the elastic line. The typical counting time per point is 10-20 min.

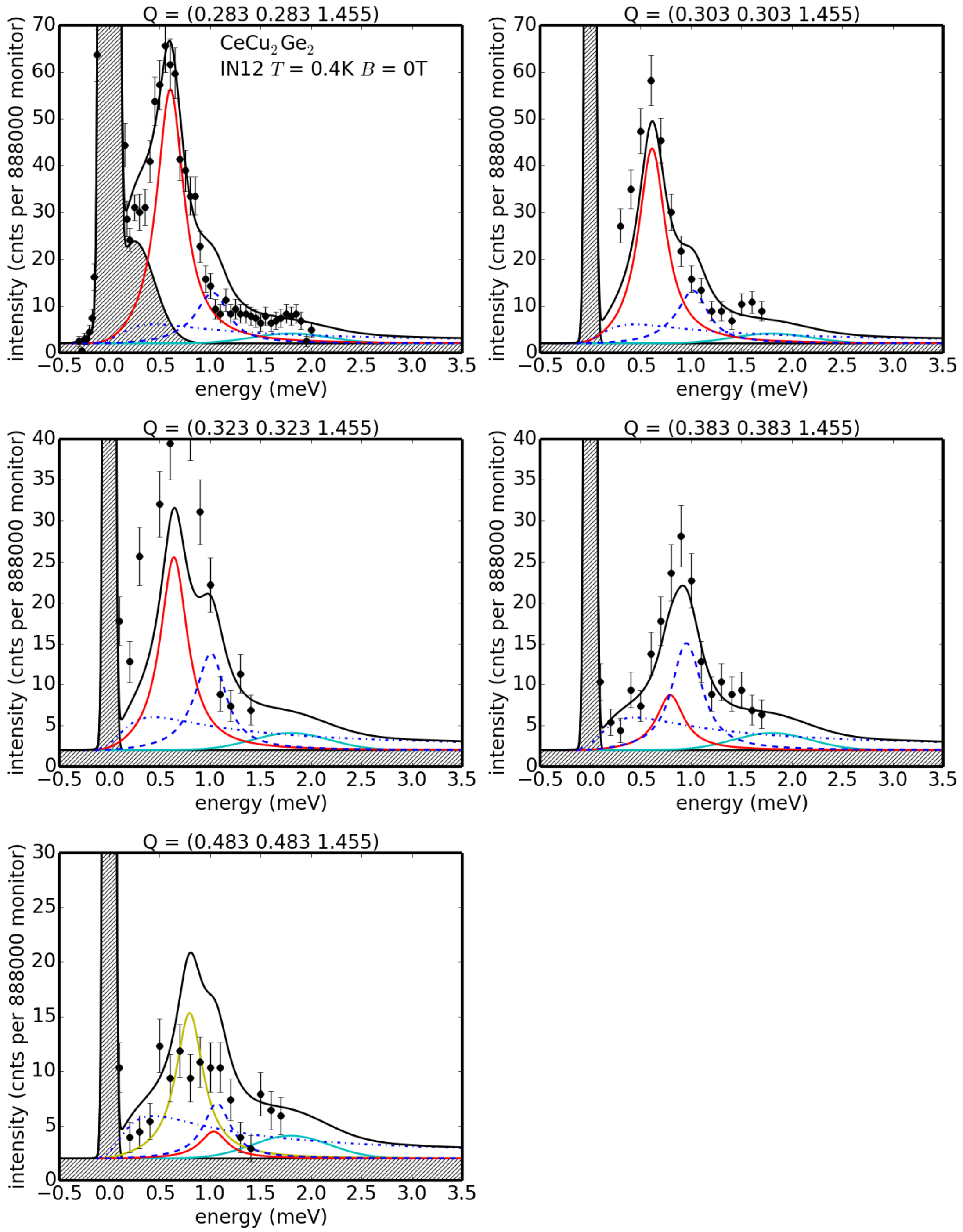

FIGURE 4.29: Constant-$\vec{Q}$ = (H H 1.455) scans (IN12). The black line corresponds to the fitted model. The red line represents the domination spin wave excitation, while the dashed blue line corresponds to the spin wave background. The blue dash dotted line is the fixed quasi elastic. The shaded region indicates the constant background and the elastic line. The typical counting time per point is 5 min.

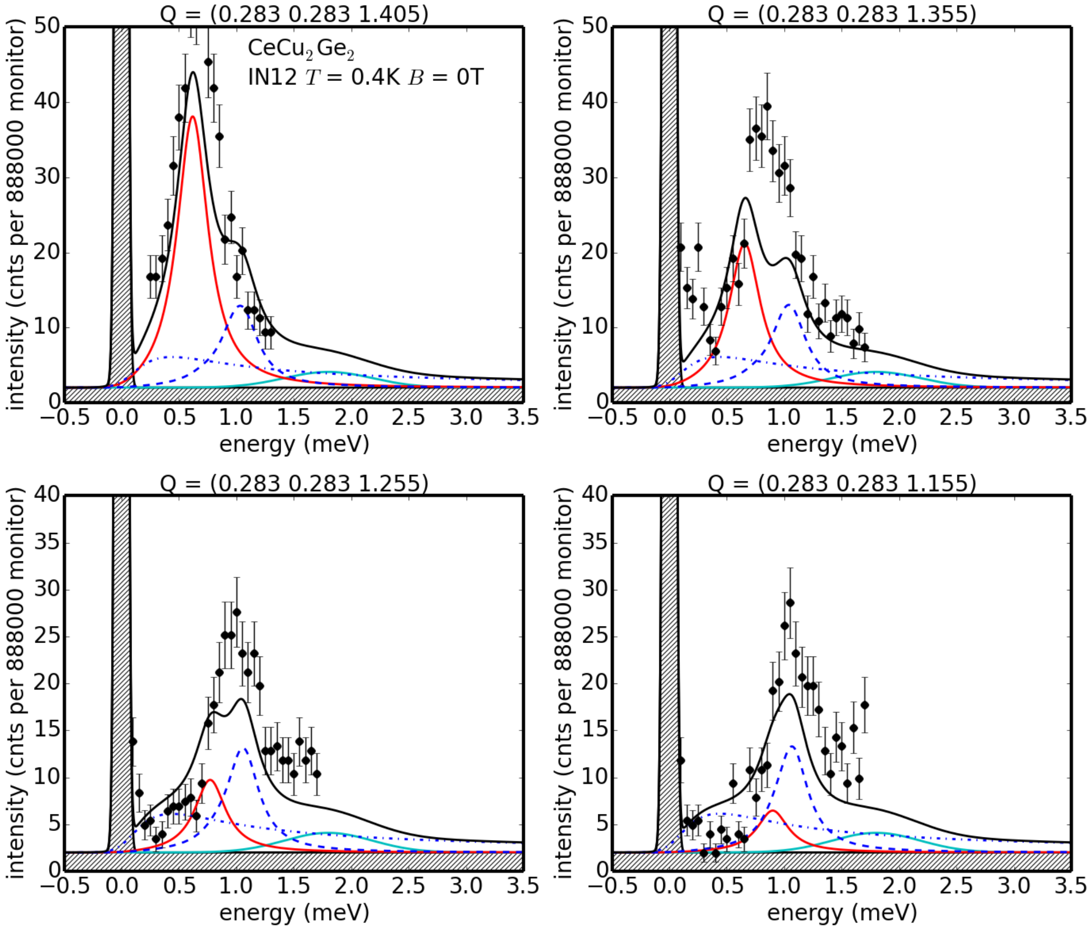

FIGURE 4.30: Constant-$\vec{Q}$ = (0.283 0.283 L) scans (IN12). The black line corresponds to the fitted model. The red line represents the domination spin wave excitation, while the dashed blue line corresponds to the spin wave background. The blue dash dotted line is the fixed quasi elastic. The shaded region indicates the constant background and the elastic line. The typical counting time per point is 5 min.

With the obtained parameters, displayed in Tab. 4.4, a relatively good description of the measured data is achieved considering the simplicity of the model. One can notice a small discrepancy, if the positions of the primary spin wave mode and the spin wave background nearly overlaps. This can be an effect from the inclusion of only nearest and next nearest neighbor interactions. Small additional contributions may lead to slightly changed excitation energies and thus slightly changes the cross over points of the different spin wave modes. However, this effect is small enough to ensure the energy scales of the principal interactions are correctly attributed. The small offsets in the counting rate for some of the constant-Q scans is most likely a result of the not perfectly isotropic sample shape. A plot of the excitation energy versus the momentum transfer can be found in Fig. 4.31.

The comparison of the peak position to the fitted dispersion shows explicitly that spin

	PANDA
χ_{afm}	84 ± 5
$\Gamma_0(meV)$	0.165 ± 0.009
D (meV)	44 ± 3
2SJ_1 (meV)	-0.042 ± 0.007
2SJ_2 (meV)	-0.18 ± 0.01
g$\mu_B B_{\text{int}}$	0.187 ± 0.008

TABLE 4.4: Fitting parameters for the dispersion measured on PANDA.

wave modes other than the one arising from (0.285 0.285 1.457) are needed to describe the data. Only by considering also intensity from spin wave modes starting $\vec{Q}$ = (±0.285 ∓0.285 1.457), the down shift of intensities for H $>$ 0.4 can be explained. It should be further pointed out that a simple estimation of the spin wave velocity from the points in Fig. 4.31 by fitting the linear part of the HH and L dispersion would result in an overestimation of the interaction strength. However, the relative strength of the interaction in and out of the basal would be similar.

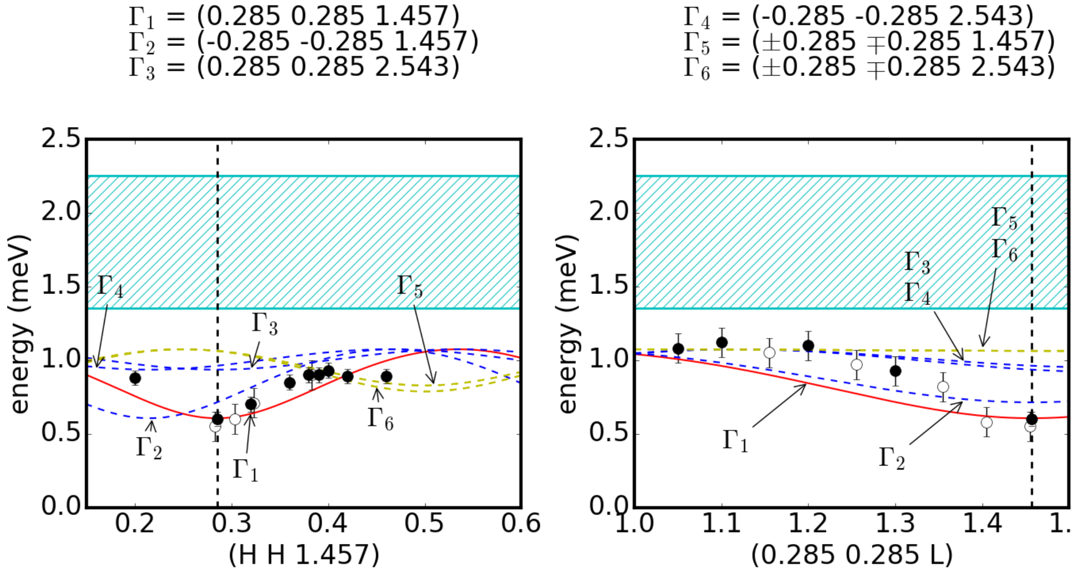

FIGURE 4.31: Dispersion (excitation energy vs. momentum transfer) for the fitted parameters. The excitation energy for different spin wave modes are labeled to their respective Γ-point. The color coding is to allow clear distinction and the vertical dashed line marks the closes Γ-point at $\vec{Q}_{AF}$ = (0.285 0.285 1.457). The closed (open) dots represent the intensity maxima in the PANDA (IN12) data. The shaded area corresponds to the additional Gaussian.

The results confirm the speculation in [37] and [35] of spin wave excitations in the antiferromagnetic state. The observed spin wave excitation at 0.9 meV in the powder data agrees with the results presented here.

Calculating T_N using S = 1/2 for the Ce^{3+} ion and [128]

$$T_{N,\,calc} = -\frac{2S(S+1)}{3k_B}\sum_i z_i J_i \tag{4.22}$$

$$= -\frac{2S(S+1)}{3k_B}\left[2SJ_1 + 4SJ_2\right] \tag{4.23}$$

yields $T_{N,\,calc}$ = 4.7 K, close to the observed value 4.15 K. Assuming the reduction of T_N by Kondo screening is proportional to χ_{afm}/χ_{qe} together with the assumption of a 1-k magnetic structure with four domains yields 4.14 K, which agrees remarkably well with the observed value. In this context, the reduction of the ordered moment even at low temperature, compared to the crystal electric field value, appears too large for the Kondo effect only. An additional, yet not understood mechanism might be present.

The molecular field B_m = 3.4±0.2 T obtained here (using g = 6/7 for the free Ce ion) appears small, considering the stability of the AF1 phase up to more than the double value. This will be resolved in Sec. 4.3.5.

4.3.3 Comparison of the RKKY interaction in the CeT_2X_2 compounds

The estimation of the interactions in the antiferromagnetic $CeCu_2Ge_2$ allows a comparison of the antiferromagnetic $CeCu_2Ge_2$, the superconducting $CeCu_2Si_2$ (investigated in [30]), and the paramagnetic $CeNi_2Ge_2$ (investigated in [32]). An overview of those compounds is given in Tab. 4.5. In all three compounds, the magnetic fluctuations are correlated to a similar incommensurate wave vector close, but distinctly different to (1/4 1/4 /2). The ratio c/a is approximately constant for all compounds, while the volume of the unit cell is enlarged for $CeCu_2Ge_2$. The occurrence of antiferromagnetism, superconductivity and paramagnetism is correlated to the increase of Kondo temperature in agreement with the Doniach phase diagram [22].

For $CeCu_2Si_2$, the strength of the RKKY interaction was estimated from the dispersion of the paramagnons in the paramagnetic state at temperature slightly above the superconducting transition temperature as well as band structure arguments. The paramagnon spectrum was found to be gapless as expected for an unordered system and their peak shape was described using an over-damped harmonic oscillator. For the interactions, a similar next nearest neighbor model as in this work was used. Only the interaction in diagonal direction in the basal plane was considered also. This interaction is denoted with the label 'basal' contrary to 'center' for the interaction to the center atom. The so obtained values are for $CeCu_2Si_2$: $2SJ_1$ = - 0.63 meV (lower limit), $2SJ_2^{basal}$ = -0.08 $2SJ_1$ and $2SJ_2^{center}$ = -0.6 $2SJ_1$. The absolute value of the $2SJ_2^{center}$ interaction is

	$CeCu_2Ge_2$	$CeCu_2Si_2$ (S)	$CeNi_2Ge_2$
a ($Å^{-1}$)	4.16	4.1 [129]	4.15
c ($Å^{-1}$)	10.20	9.9 [129]	9.842
c/a	2.45	2.4	2.37
V ($Å^3$)	176	166	169.5
$\vec{\tau}$	(0.285 0.285 0.543)	(0.215 0.215 0.542)	(0.23 0.23 0.5)
T_K (K)	5.1 [40]	$\approx$15	30 [31]
J_2 (meV)	0.18	0.63	?
J_{out} (meV)	0.15	0.33	$<<$ J_{basal}
J_{basal} (meV)	0.125	0.87	$>>$ J_{out}
J_{out}/J_{basal}	1.2	0.38	0
state	AF	SC	PM

TABLE 4.5: Comparison of $CeCu_2Ge_2$, $CeCu_2Si_2$ (S) and $CeNi_2Ge_2$. If not stated otherwise, the values are from this work ($CeCu_2Ge_2$), [30] ($CeCu_2Si_2$ (S)) or [32] ($CeNi_2Ge_2$). It was assumed S = 1/2.

two times larger compared to an three times increased Kondo temperature, which is in agreement with the respective positions in the Doniach phase diagram. In contrast, J_1 is 15 times stronger in $CeCu_2Si_2$.

This tendency is further followed in $CeNi_2Ge_2$. Below $T_K \approx 30$ K, inelastic neutron scattering revealed stripes of magnetic intensity with a maximum corresponding to a wave vector (0.23 0.23 0.5). The stripes are in the HH direction, while in L direction the fluctuations decay fast. Therefore, the fluctuations are correlated to the basal plane. The excitation energy is around 4 meV and no dispersion was observed. The behavior is not compatible with a simple picture of paramagnons. The authors in [32] assume the fluctuations to have a quasi-two-dimensional character. From this, it assumed that the interactions are confined to the basal plane.

The behavior of these three compounds is systematic over the Doniach phase diagram (Fig. 4.32). In the common phase diagram for heavy fermion systems, going along a tuning parameter (pressure, composition etc.), T_N is scaled according to the Doniach phase diagram until it reaches zero and the magnetic order is suppressed. The resulting quantum critical point is surrounded by the superconducting dome, followed by paramagnetism. The total interaction in and out of the basal plane can be calculated for the next nearest neighbor model using

$$J_{out} = J_2 \sin(\alpha) \tag{4.24}$$

$$J_{basal} = J_1 + J_2^{basal} + J_2 \cos(\alpha) \tag{4.25}$$

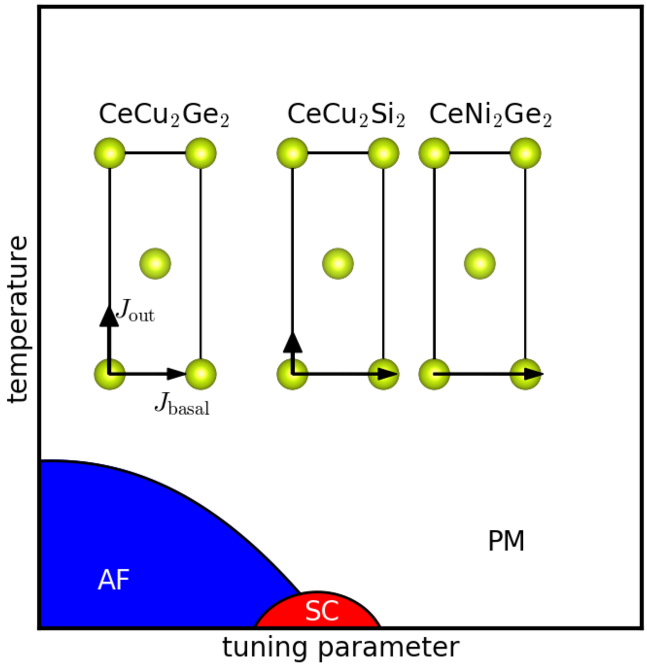

FIGURE 4.32: Schematic phase diagram of heavy fermion systems for a tuning parameter, e.g. composition, pressure. The relative size (normalized to one) of the interactions J_{out} and J_{basal} are depicted for $CeCu_2Ge_2$, $CeCu_2Si_2$ and $CeNi_2Ge_2$ together with the magnetic Ce atoms in the unit cell.

where $\alpha \approx 60°$ is the angle between the body diagonal and the basal plane diagonal. Note that in Fig. 4.32, the strength of the interaction was normalized. In the antiferromagnetic state ($CeCu_2Ge_2$), J_{out} and J_{basal} are on the same scale. Upon entering the superconducting state ($CeCu_2Si_2$), J_{out} becomes smaller than J_{basal}. Finally J_{out} becomes zero in the paramagnetic state ($CeNi_2Ge_2$).

Those results may reveal an important piece in the puzzle of magnetic fluctuation mediated superconductivity: at least in the CeT_2X_2 compounds discussed here, the interplay of magnetism and superconductivity is not only controlled by the energy scale of competing mechanisms (Kondo and RKKY), but also on the anisotropy of the long range RKKY interaction. Such a behavior is in line with the observation that superconductivity is supported by strong anisotropy in tetragonal systems [130].

Further work on the exploration of the anisotropy of the RKKY along the Doniach phase diagram is highly desirable. To rule out doping effects, such an investigation should be made on a series of isoelectronic compounds covering the antiferromagnetic, superconducting and paramagnetic state. In the CeT_2X_2 (T = Au, Ag, Cu; X = Si, Ge) no paramagnetic compound exists. In analogy to the increase of the hybridization upon substituting Ge by smaller Si atoms, substituting Ge by the even smaller C atoms is expected to further increase the hybridization. The resulting hypothetical CeT$_2$C$_2$ (T = Au, Ag, Cu) compounds are expected to become either superconducting or paramagnetic.

4.3.4 Temperature dependence of the excitation spectrum

The temperature dependence of the excitation spectrum was measured with constant $\vec{Q} = \vec{Q}_{\mathrm{AF}}$ scans for different temperatures below T_{N}. To fit the obtained data, contribution from the elastic line that correspond to intensity from the magnetic Bragg peak, i.e. the coherent part as well as the additional gaussian at 0.25 meV, were scaled according to the order parameter. Additionally, the broad gaussian at 1.8 meV was also scaled with the order parameter.

The temperature correction in Eq. 4.20 for the spin wave and in Eq. 4.13 for the quasi elastic was adjusted according to the nominal set temperature. The molecular field parameter that produces the gap in the spin wave excitation spectrum, as well as the intensity of the spin wave, were scaled according to the order parameter.

For the quasi elastic single site excitation, the intensity was scaled according to $\chi_{\mathrm{qe}} \propto (|T - T_{\mathrm{N}}|/T_{\mathrm{N}})^{-\gamma}$ with the mean field critical exponent $\gamma = 1$. For $T < 2$ K, the width was held constant at $\Gamma_{qe} = \mathrm{k_B} T_{\mathrm{K}}$. For $T > 2$ K, Γ_{qe} was fitted as a free parameter.

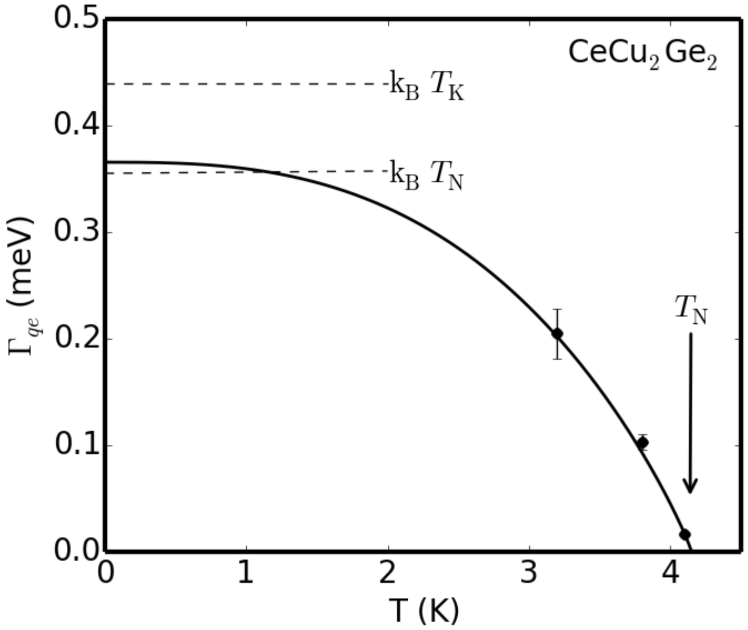

FIGURE 4.33: Temperature dependence fitted molecular field parameter. The points for $T < 2$ K corresponds to the fixed value. The solid line is the order parameter scaling established before.

It should be noted that the scale of the interactions were assumed temperature independent. This assumption might not be necessarily correct, however the data measured at $\vec{Q}_{AF}$ are insensitive to changes in the interaction. Hence, the temperature dependence of the interactions can not be answered.

With the simple approach outlined here, the excitation spectra for all temperatures measured could be described. The lack of enhanced spin wave fluctuations together with the common mean field temperature scaling of the single site fluctuations identify local fluctuations as the driving mechanism of the temperature induced phase transition. The critical exponent $\gamma = 1$ for the susceptibility is consistent with the scaling of the order parameter. Measurements reported in [41; 42; 40] suggests a critical exponent for the specific heat $\alpha = 1$. Therefore, the scaling law $\alpha + 2\,\beta + \gamma = 2$ is fulfilled with exponents according to the mean field prediction for a 2nd order phase transition.

The obtained temperature dependence of Γ_{qe} is pictured in Fig. 4.33. The solid line corresponds to the order parameter scaling, which gives a well description for the $T > 2$ K values. Extrapolating this line to low temperature gives Γ_{qe} = 0.37 meV = 4.3 K/k_B. This is close to T_N and somewhat smaller than the currently established Kondo temperature for $CeCu_2Ge_2$. As Γ_{qe} is inversely proportional to the life time of the single site excitation, an additional relaxation mechanism would result in a larger value of Γ_{qe}. Also neglecting the resolution can not be responsible for a smaller width. Therefore, it is reasonable to consider a smaller Kondo temperature T_K = 4.3 K. The data at lower temperature are compatible with such a smaller Kondo temperature.

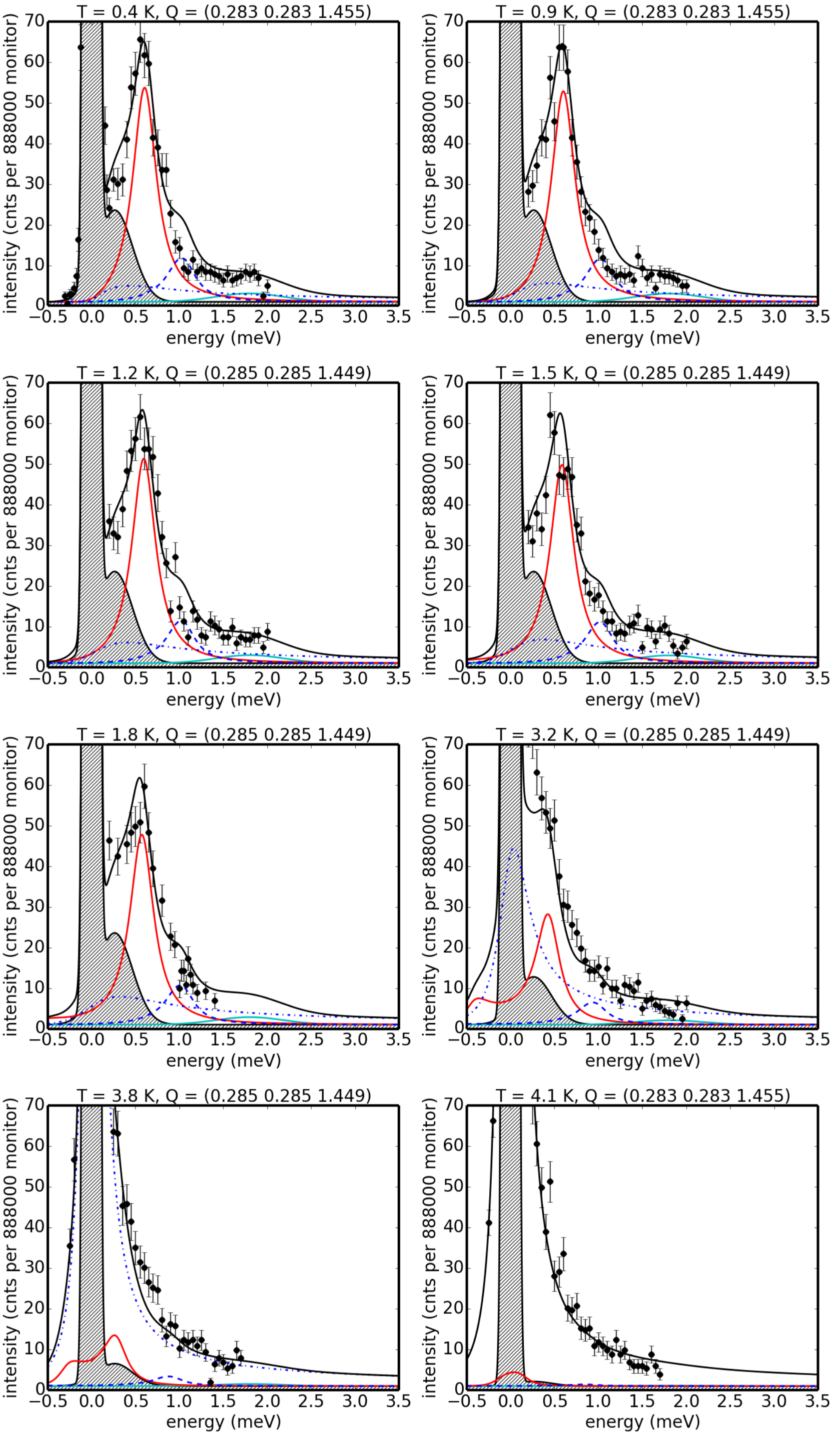

FIGURE 4.34: Constant-$\vec{Q}$ = (0.283 0.283 1.455) scans (IN12) at different temperatures. The black line corresponds to the fitted model. The red line represents the domination spin wave excitation, while the dashed blue line corresponds to the spin wave background. The blue dash dotted line is the fixed quasi elastic. The shaded region indicates the constant background and the elastic line. The typical counting time per point is 5 min.

4.3.5 Field dependence of the excitation spectrum

Inside the AF1 phase the spin wave splits up in two separated peaks. This can be accounted for by the two sublattice antiferromagnetic model. Depending on the sublattice spin direction, the external field is added (subtracted) for (anti-)parallel spins. The spectra corresponding $B = B_m + B_{exth}$ and $B = B_m - B_{ext}$ are then superposed to obtain the resulting spectrum. The respective intensities are labeled I^+ and I^-. Strength of the external field $g\mu_B B_{ext}$ and the intensities I^+ and I^- are free fit parameters. The remaining parameters are adopted from the zero field dispersion. This simple approach nicely describes the splitting (Fig. 4.35 and Fig. 4.36 (left)).

The values obtained by the fit are plotted against the actual applied external field B in Fig. 4.37. $g_{free}\mu_B B_{ext}$ depends linearly on B as expected, but the slope is surprisingly

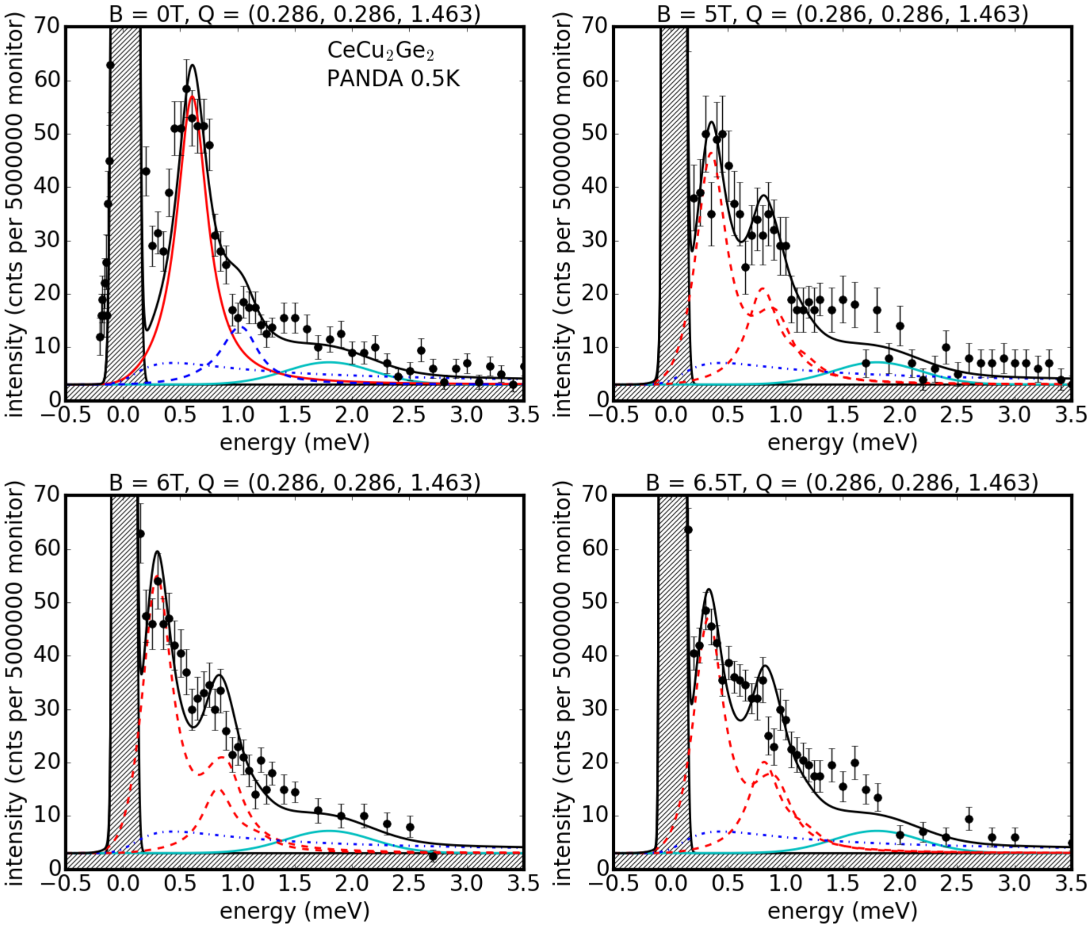

FIGURE 4.35: Constant-$\vec{Q}$ = (0.286 0.286 1.463) scans (PANDA) at magnetic field. The black line corresponds to the fitted model. The dashed blue line corresponds to the spin wave background. The blue dash dotted line is the fixed quasi elastic. The shaded region indicates the constant background and the elastic line. The dominating spin wave excitation is represented by the red line (solid for B = 0 T, dashed B ≠ 0 T). The typical counting time per point is 10-20 min.

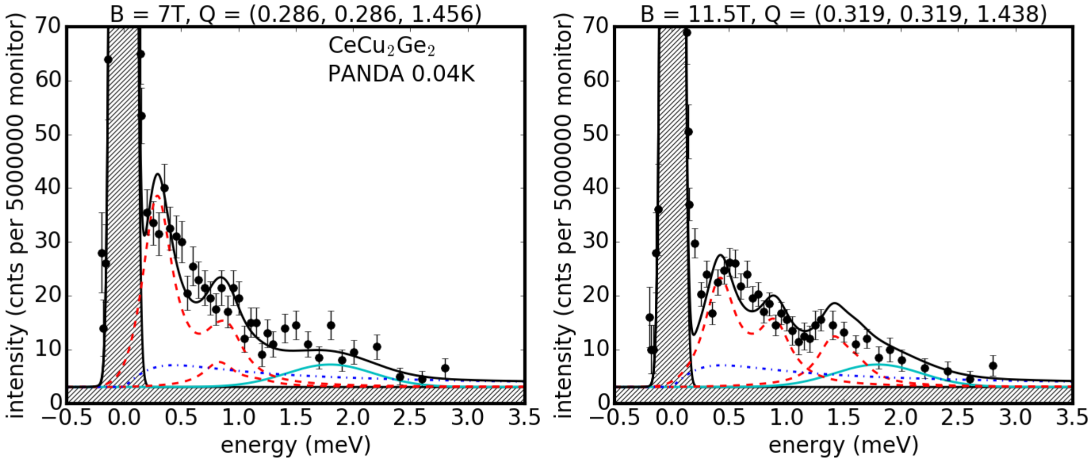

FIGURE 4.36: Constant-$\vec{Q}$ scans (PANDA) at different magnetic fields. The black line corresponds to the fitted model. The dashed blue line corresponds to the spin wave background. The blue dash dotted line is the fixed quasi elastic. The shaded region indicates the constant background and the elastic line. The dominating spin wave excitation is represented by the dashed red line. The typical counting time per point is 10-20 min.

small. A linear fit gives $m = (0.0208 \pm 0.0009)$ meV/T.

From $E = g_{\mathrm{free}}\mu_{\mathrm{B}}B$ ($g_{\mathrm{free}} = 6/7$ for the free Ce^{3+} ion), one would expect $m = g_{\mathrm{free}}\mu_{\mathrm{B}} = 0.0496$ meV/T. This discrepancy can not be explained as an uneven sublattice magnetization, resulting in bulk magnetization. From [63] one can estimate that the order of magnitude of this effect is $m = 0.025 g\mu_{\mathrm{B}} = 0.0013$ meV/T and therefore is too small. It would also lead to an increase of m. The reason for this apparent discrepancy is the assumption that the Landé-factor corresponds to the free ion. The authors of [131] found that if magnetic field is included in a RKKY-Hamiltonian via an Zeeman term, the RKKY interaction retains it conventional form, but an effective gyromagnetic factor

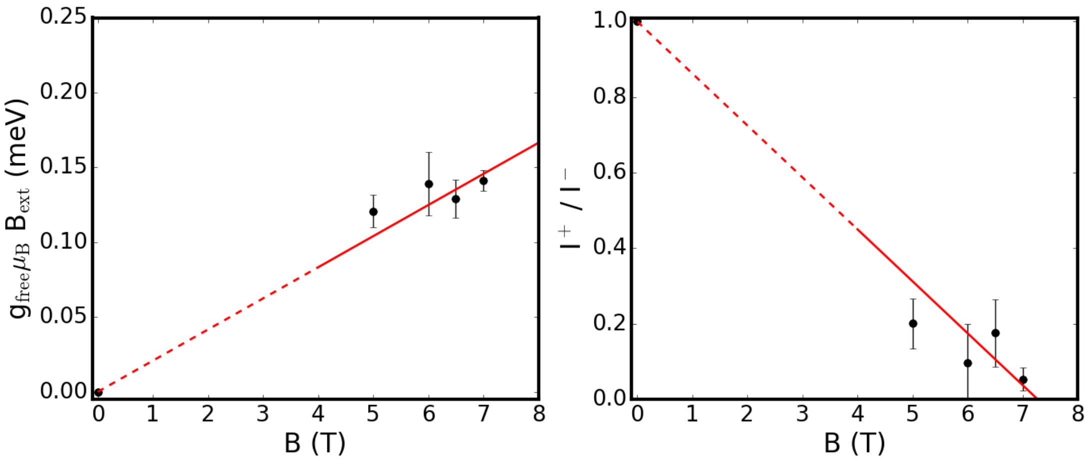

FIGURE 4.37: Magnetic field dependence of the fit parameters $g_{\mathrm{free}}\mu_B B_{\mathrm{exth}}$ (left) and I^+/I^- (right). The red line is a linear fit to the obtained parameters in the AF1 phase.

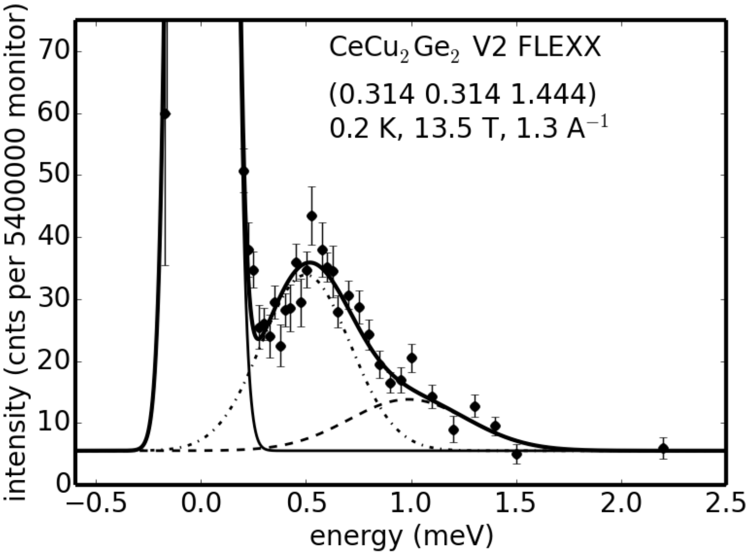

FIGURE 4.38: Constant-$\vec{Q}$ scan (V2 FLEXX) at 13.5 T. The black line corresponds to an empiric fit using two gaussians (dashed and doted/dashed lines). The typical counting time per point is 10-20 min.

g^{eff} = $g_{\mathrm{corr}}g_{\mathrm{e}}+g_{\mathrm{j}}$ has to be used, where g_{corr} = $Am^{*}k_{\mathrm{F}}/h^{2}$ and $g_{\mathrm{e}} \approx$ -2 is the Landé-factor for the free electron. A is the contact potential between local and conduction band electrons. The calculated correction is $g_{\mathrm{corr}}g_{\mathrm{e}}$ = - 0.50±0.01, which is approximately two times larger as expected in [131] for a normal metal. The increase is not surprising, since $g_{\mathrm{corr}} \propto m^{*}$, which is large in CeCu$_2Ge_2$ (80m_e [132]) compared to normal metals. The contact potential A fulfills $A > 0$ as expected for electrons. Using g^{eff} = 0.36 ± 0.01, the value for the molecular field yields B_{m} = 9 T, slightly higher than B_1.

The I^{+} intensity is suppressed upon approaching the AF1/AF2 transition. A linear extrapolation using I^{+}/I^{-} = 1 in zero field gives a total suppression of the I^{+} at (7.2±0.3) T, close to the AF1/AF2 transition. This behavior can be interpreted as a destabilization of anti-parallel sublattice while parallel sublattice is stabilized. This destabilization could be connected to the AF1/AF2 transition mechanism. An actual two sublattice antiferromagnet would either be polarized (spin-flop transition) or have a metamagnetic spin-flip transition. For CeCu$_2$Ge$_2$ the energetic advantage of nesting would be lost for such simple magnetic structures. Instead magnetic order is established in the AF2 phase that has comparable nesting properties. The molecular field is expected to be higher for this structure to be stable also in the high external field. To verify this hypothesis, the scan in the AF2 phase (11.5 T, Fig. 4.36 (right)) is fitted using the same approach as for the AF2 phase, except also the molecular field was set as a free parameter in the fit. The obtained parameters are $g\mu_{\mathrm{B}}B_{\mathrm{m}}$ = (0.42±0.03) meV, $g\mu_{\mathrm{B}}B_{\mathrm{exth}}$ = (0.35±0.03) meV and I^{+}/I^{-} = 0.14±0.04. Indeed, the molecular field is larger than the external field. From $g\mu_{\mathrm{B}}B_{\mathrm{m}}$, g^{eff} = 0.525 is derived. This hints a change in electronic properties. The molecular field then corresponds to 13.8 T. Extrapolating I^+/I^- to zero, assuming also I^+/I^- = 1 in zero field, yields 13.4 T. Both values are close to the phase transition to the unknown phase at 12.6 T. This suggests that the mechanism of this phase transition is comparable to the one of the AF1/AF2 transition.

For the phase above 12.6 T, only data measured at V2FLEXX are available. Due to lower $\vec{Q}$-resolution, the quality of the data obtained are not comparable to the PANDA or IN12 data. It was not possible to resolve the splitting in AF1 and AF2 phase. A constant $\vec{Q}$-scan at 13.5 T is shown Fig. 4.38. The $\vec{Q}$-position was kept fixed from the AF2 phase as no wave vector corresponding to magnetic fluctuations is known in this phase. The elastic line was fitted using only one single gaussian as it consisted only of incoherent scattering. A constant background of 5.5 counts was assumed. The remaining inelastic spectrum was fitted using two Gaussins. The smaller one at higher energy mostly accounts for the unknown broad feature already observed in the PANDA and the IN12 data. The larger Gaussian would be compatible with the existence of spin waves on a similar energy scale above B_3. The intensity is comparable to the AF1 and AF2 phase. Even the spectrum is clearly gaped at the measured $\vec{Q}$, it is not possible to state if the spectrum is gaped as the measurement was obviously not performed at the Γ point of the magnetic unit cell in this phase.

4.3.6 Summary

In summary, the low energy excitation spectrum was described considering two contributions: the single site Kondo effect, modeled by a quasi elastic contribution and an inter-site spin wave excitation from the RKKY interaction. For the spin wave excitation, the simplest possible model, a two suplattice antiferromagnet with only next nearest neighbor interactions, was considered. A reasonable description of the spectra for the dispersion, temperature and magnetic field dependence was achieved. The dispersion yielded the interactions $2SJ_1$ = (-0.042 ± 0.007) meV (basal plane) and $2SJ_2$ = (-0.18 ± 0.01) meV (body diagonal), i.e. the interaction in the basal plane were found to be vanishingly small and the diagonal interaction to the centered Ce place dominates.

Comparing this situation to CeCu$_2$Si$_2$ and CeNi$_2$Ge$_2$ reveals a strong enhancement of the interaction in the basal plane going from antiferromagnetism (CeCu$_2$Ge$_2$) to superconductivity (CeCu$_2$Si$_2$) and finally paramagnetism (CeNi$_2$Ge$_2$). This new finding appears to be an important puzzle piece for the understanding of the magnetism in CeT$_2$X$_2$ compounds as well as other heavy fermion systems.

The temperature dependence of the excitation spectrum is as expected for a 2nd order transition.

The field dependence revealed a splitting of the spin-wave peak. This could be modeled by assuming parallel or antiparallel field for each sublattice of the two suplattice antiferromagnet model. Effective Landé factors in AF1 (g^{eff} = 0.36) and AF2 (g^{eff} = 0.525) had to be introduced. These effective Landé-factor are justified by the RKKY character of the electronic system. Finally, the spin-waves persist in the C-phase.

Chapter 5

Magnetic phase diagram of $CeCu_2(Si_{0.55}Ge_{0.45})_2$

5.1 Specific heat

The results of the specific heat measurements are depicted in Fig. 5.1. In zero field, three phase transitions are observed: a continuous upturn at T_0 = 2.9 K as expected for a paramagnetic to afm order transition, a sharp peak located at T_1 = 2.1 K and an anomaly at T_L = 1.46 K as previously reported [133]. In the following, the field dependence of these phase transitions is discussed, starting at highest temperature.

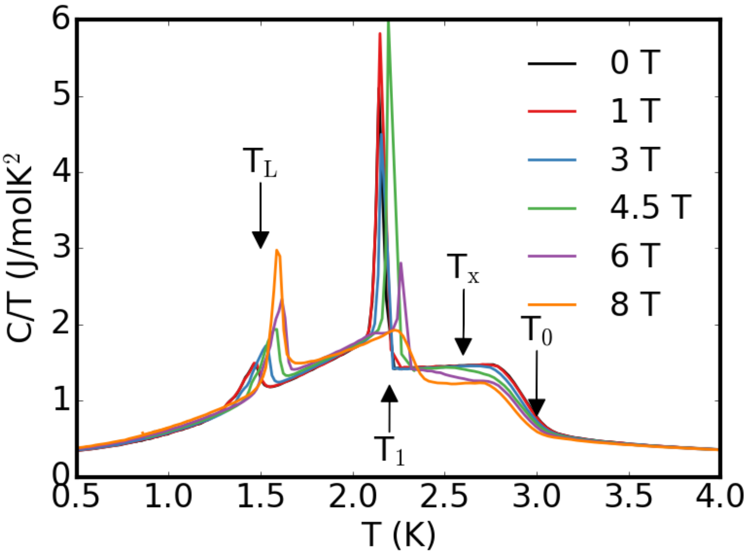

FIGURE 5.1: Specific heat measured in magnetic field up to 8 T.

In zero field, T_0 was associated with the the Néel-temperature. As later shown, the neutron diffraction results indicate that the onset of magnetic order is happening at lower temperatures in non zero field. To avoid confusion, T_0 is used for specific heat data and T_N for the neutron diffraction data. The upturn, indicating T_0, only shows a small change under magnetic field regarding its position. In contrast, the height shows a change as it is clearly reduced for $B > 3$ T. A contribution to the T_0-jump starts to move to lower temperature upon increasing the field, marked as T_x. T_1 was previously attributed to a change of the orientation of the ordered moments [134]. Because the peak at T_1 is very narrow, it can be assumed as a first-order transition [133]. Upon increasing the field, the position slightly increases from 2.1 K in zero field to 2.3 K at 6 T. At 8 T, the peak disappears and T_1 and T_X merged, leaving a continuous curve behind, with very similar shape as T_0. The anomaly at T_L was previously identified by neutron diffraction as a lock-in transition of the propagation vector [134]. With increasing field, it shifts to higher values (to 1.6 K at 8 T). The hight of the jump follows a $\propto B^2$ dependence.

5.2 Neutron diffraction

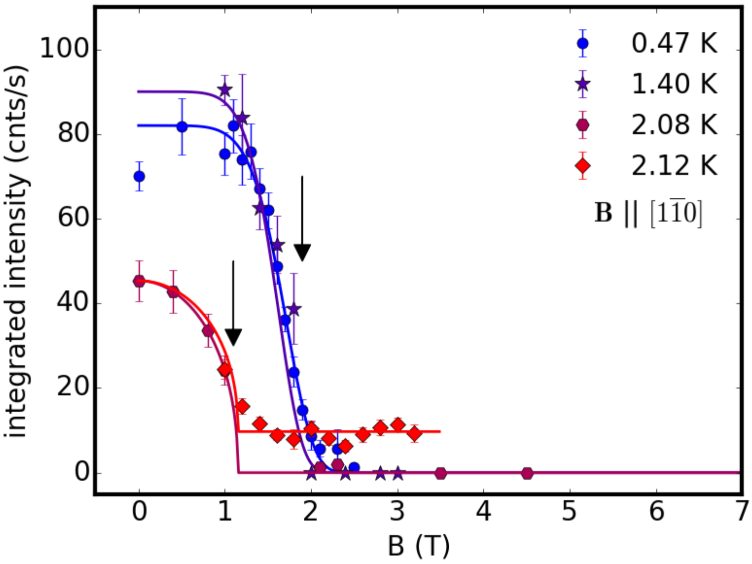

FIGURE 5.2: Magnetic field dependence of the integrated intensity for representative temperatures. The solid lines are guides for the eyes.

The integrated intensities obtained for increasing magnetic field while holding the temperature constant is shown in Fig. 5.2 and Fig. 5.3. At lowest temperatures (0.47 K to 2.08 K), the integrated intensity stays constant until a sharp drop off to zero appears between 1 and 2 T, ruling out a 2nd order phase transition. This behavior is different for the higher temperatures (2.20 K and 2.28 K): here, the integrated intensity persist up to

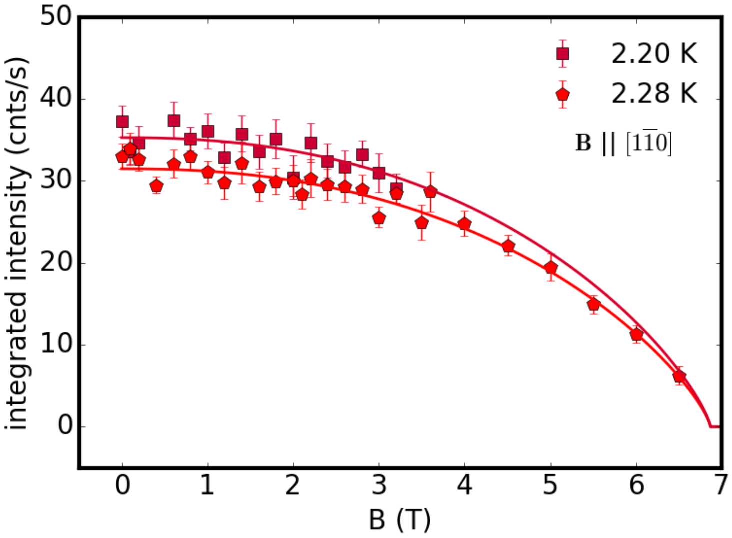

FIGURE 5.3: Magnetic field dependence of the integrated intensity for representative temperatures. The solid lines are guides for the eyes.

nearly 7 T and the drop off follows an order parameter dependence $\propto [1-(B/B_0)^\alpha]^\beta$ with α = 2.3 ± 0.4, β = 0.8 ± 0.2 and B_0 = 6.8 ± 0.3 T, consistent with $CeCu_2Ge_2$. At 2.12 K a mixture of both behaviors is observed: up to 1 T the field dependence follows nearly exactly the values for 2.08 K. Above 1 T, the integrated intensity stays at a constant, non-zero value up to at least 3 T. Therefore, two magnetic phases exist: one low temperature phase and a high temperature phase with much larger critical field. A first order transition between both is happening very close to 2.12 K, with a small range of coexistence.

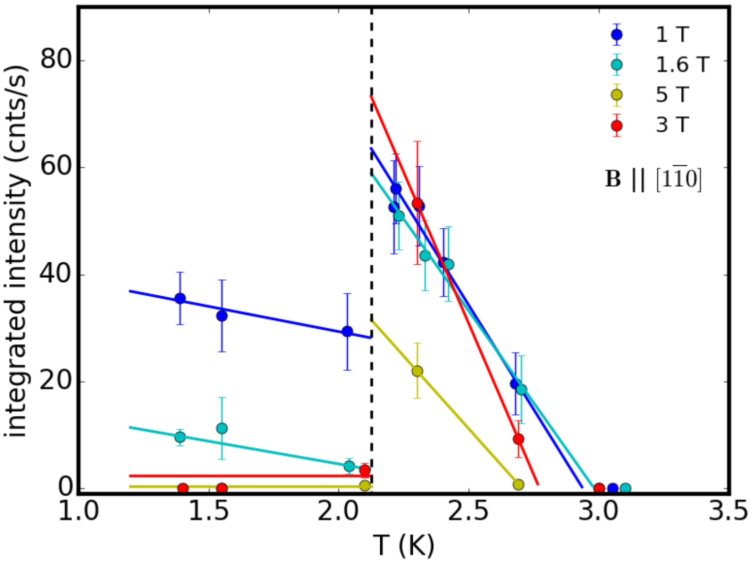

FIGURE 5.4: Temperature dependence of the integrated intensity for various magnetic fields.

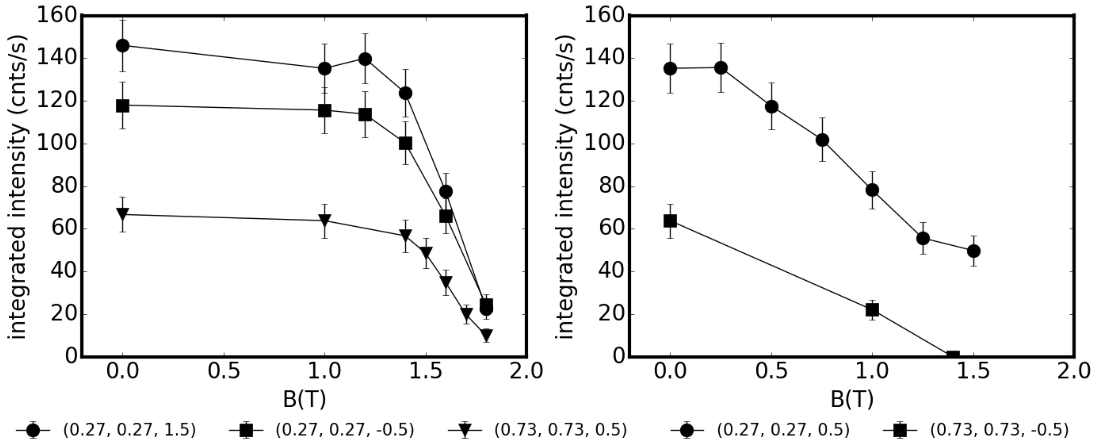

FIGURE 5.5: Magnetic field dependence of the integrated intensity for magnetic satellites corresponding to the $(\pm\tau_h \pm\tau_h \mp\tau_l)$ domain (left) and the $(\pm\tau_h \pm\tau_h \pm\tau_l)$ domain (right). T = 0.5 K (LAF) phase.

The temperature dependence of the integrated intensity upon cooling for various magnetic fields is shown in Fig. 5.4. Starting at high temperature, the integrated intensity increases linearly as expected for a 2nd order transition. Upon increasing the magnetic field, the intensity is further suppressed. The linear dependence lasts as low as 2.12 K. At this point, the integrated intensity drops off sharply, a clear sign for a first order transition. For 3 T and 5 T, no magnetic intensity is observed below 2.12 K.

The (B,T) dependence for constant field and constant temperature measurements agree within the observed phase boundaries. Comparing the absolute values of the integrated intensity, a difference for the constant field and constant temperature measurements is visible. In the high temperature phase, the integrated intensity obtained with constant field is approximately 1.5 times the intensity obtained with constant temperature. This is most likely a domain population effect. Such a difference is not found for the low temperature phase.

In both phases (measured at 0.47 K and 2.2K), after the magnetic Bragg peaks disappear, lowering the magnetic field again does not reestablish the magnetic intensity. Instead, the sample has to be heated to $>$ 6 K and cooled down again. From Fig. 5.5, one can see that the with of the intensity drop depends on the type of domain in the LAF phase. A reasonable assumption is, that no phase transition is happening around 2 T, but instead the $(\pm\tau_h \pm\tau_h \mp\tau_l)$ and $(\pm\tau_h \pm\tau_h \pm\tau_l)$ domains are depopulated in favor of the $(\pm\tau_h \mp\tau_h \pm\tau_l)$ and $(\pm\tau_h \mp\tau_h \mp\tau_l)$ domains, which have peaks out of the scattering plane.

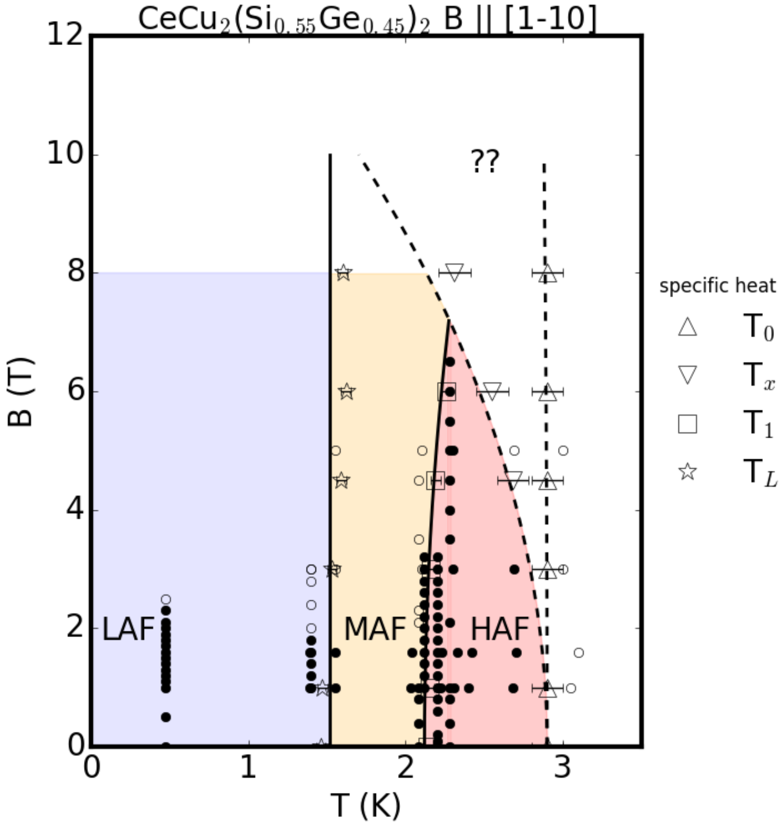

FIGURE 5.6: Magnetic phase diagram of CeCu$_2$(Si$_{0.55}$Ge$_{0.45}$)$_2$ from the specific heat and neutron diffraction data. Solid lines represent first order phase transitions and dashed lines second order phase transitions. The existence (absence) of magnetic satellites is indicated by the closed (open) dots.

5.3 Phase diagram

From the specific heat measurements and the (B,T) dependent neutron diffraction results, the magnetic phase diagram (Fig. 5.6) was constructed. Somewhat similar as before for the CeCu$_2$Ge$_2$ phase diagram, the closed dots represent the presence of the zero field peaks from LAF, MAF or HAF and the open symbols are used to indicate those peaks are absent.

In the LAF and MAF phase, the magnetic satellites already disappear at around 2 T. It is assumed that this is not an actual phase transition, but a depopulation of the domains with satellites in the scattering plane. This view is supported by the fact, that no change in specific heat is observed. Favoring of the magnetic domains with satellites outside the scattering plane would be in line with the finding on the AF2 phase in CeCu$_2$Ge$_2$. As the magnetic satellites from the still populated domains are out of the scattering plane, no information from the neutron diffraction of the further field dependence is available.

The presence of the lock-in transition up to 8 T in the specific heat data suggest no further change in the magnetic order up to at least 8 T.

The HAF phase is continuously suppressed by magnetic field of $\approx$ 6.8 T at 2.28 K. A good result for the field dependence of the onset of the HAF phase is obtained by the scaling $[1-(B/B_0)^2]$. A smaller exponent would miss the suppression of the zero field magnetic order at 2.28 K and 6.8 T, while a larger exponent would lead a vanishing of the magnetic order below 8 T.

The nature of the C-phase is unknown. The presence of the step in specific heat at T_0 points towards magnetic order, but no neutron data for this phase that could prove microscopically the existence of magnetic order is available.

This situation is very similar to $CeCu_2Ge_2$, where in a similar way an unknown phase emerges in magnetic field. Using the quadratic dependence of the suppression of the HAF phase, one would expect the MAF and LAF phases vanish at 15 T in favor of the unknown phase. From the available date, the existence of an additional pocket around 10 T, in analogy to the AF2 phase in $CeCu_2Ge_2$, can neither be confirmed nor rejected.

5.4 Summary

Starting from the already known zero field phases LAF, MAF and HAF, the magnetic field dependence was explored. For LAF and MAF, the magnetic satellites already disappear at around 2 T. This was attributed to a depopulation of the domains with satellites in the scattering plane. The HAF phase is continuously suppressed and the magnetic satellites vanish at around 7 T. At higher field, a phase of unknown magnetic order is present. The overall shape of the phase diagram is very similar to $CeCu_2Ge_2$.

Chapter 6

$CeCo_xIr_{1-x}In_5$

6.1 Initial growth attempt

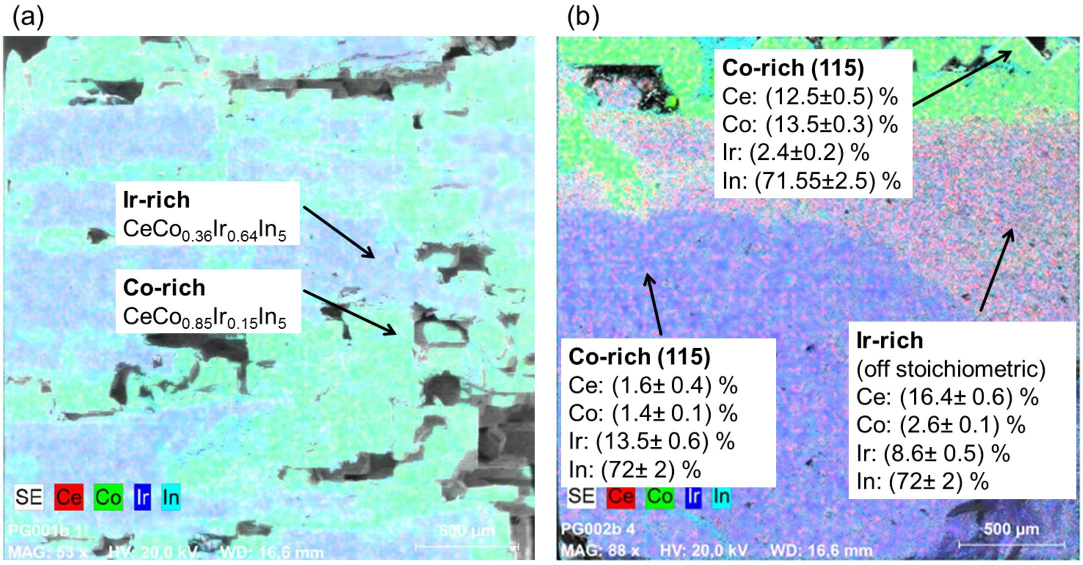

FIGURE 6.1: EDX maps of polished surfaces of two different samples showing the elements Ce, Co, Ir and In. The nominal composition for both samples is $CeCo_{0.5}Ir_{0.5}In_5$.

The initial growth attempt yielded pieces of the approximate size 8 x 8 x 5 mm with layers stacked together. EDX maps of the polished surface are depicted in Fig. 6.1. Co- and Ir-rich regions are observed in $CeCo_xIr_{1-x}In_5$. The Ir-rich regions have a tendency to form rectangular areas connected by Co-rich parts (see Fig. 6.1 (a)). In Fig. 6.1 (b) on the top, a Co-rich region of $CeCo_xIr_{1-x}In_5$ and in the lower part an Ir-rich region is visible which is adjacent to regions of non stoichiometric composition with excess Ce and a deficit in Co/Ir. This kind of clustering is in general not uncommon. Similar clustering effects have been observed in the related Ce_2PdIn_8 [135].

An off stoichiometric phase was observed, that could not be connected to a composition within the $Ce_nM_mIn_{3n+2m}$ scheme. A possible explanation is that $CeIn_3$ and MIn_2 layers grow aperiodic on each other in this regions. From those results, one can conclude that two issues have to be addressed: (i) elimination of non stoichiometric phases and (ii) reliable control of homogeneous Co/Ir distribution.

6.2 Optimization of the preparation process

To cure the issues depicted above, the following changes in the growth process have been tested:

- Ir powder as starting material
- Prealloying of Co and Ir
- Alloying stoichiometric ratios by arc melting
- Starting materials prealloyed in stoichiometric ratios by arc melting
- Different amount of In flux
- Change of temperature profile
- Annealing after growth

If not otherwise stated, the rest of the preparation process was not altered from the above.

Ir powder as starting material

Using powder instead of chunks might improve the homogeneity of initial distribution in the melt. Therefore, to achieve a more homogeneous Co/Ir distribution, Ir powder was used as starting material. This resulted in similar samples as with the initial growth. The polished surface of the obtained samples were pointwise characterized by EDX. The number of occurrences of a specific amount of Ce, Co and Ir is shown in Fig. 6.2. Similar as for the initial growth, one can see an accumulation at 17 % Ce, while no improvement in Co/Ir distribution is achieved. In fact, the grown samples are lacking significantly Co.

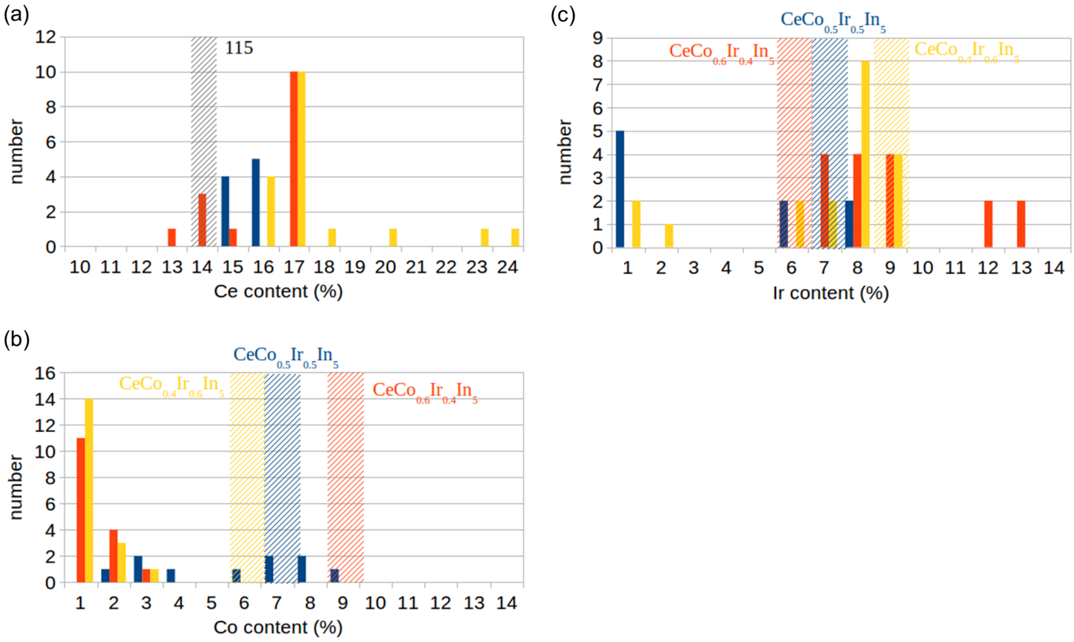

FIGURE 6.2: Number of occurrences of (a) Ce (b) Co and (d) Ir content in samples grown from power. Determined from EDX spectra at random points of polished sample surfaces. The hatched region indicates the nominal content. In has been left out, as the uncertainty in the determination is too large to distinguish between the occurring compositions effectively.

Prealloying of Co and Ir

Co and Ir in ratios of 0.4:0.6, 0.5:0.5 and 0.6:0.4 were prealloyed by arc melting before the flux growth. The growth results were similar characterized as before and the results are shown in Fig. 6.3. The occurrence of 115 is somewhat improved, but a significant amount of 17 % Ce is present. No improvement for homogeneous Co/Ir distribution was observed: on the contrary, the Co/Ir ratio seems to be uniformly distributed over a wide range.

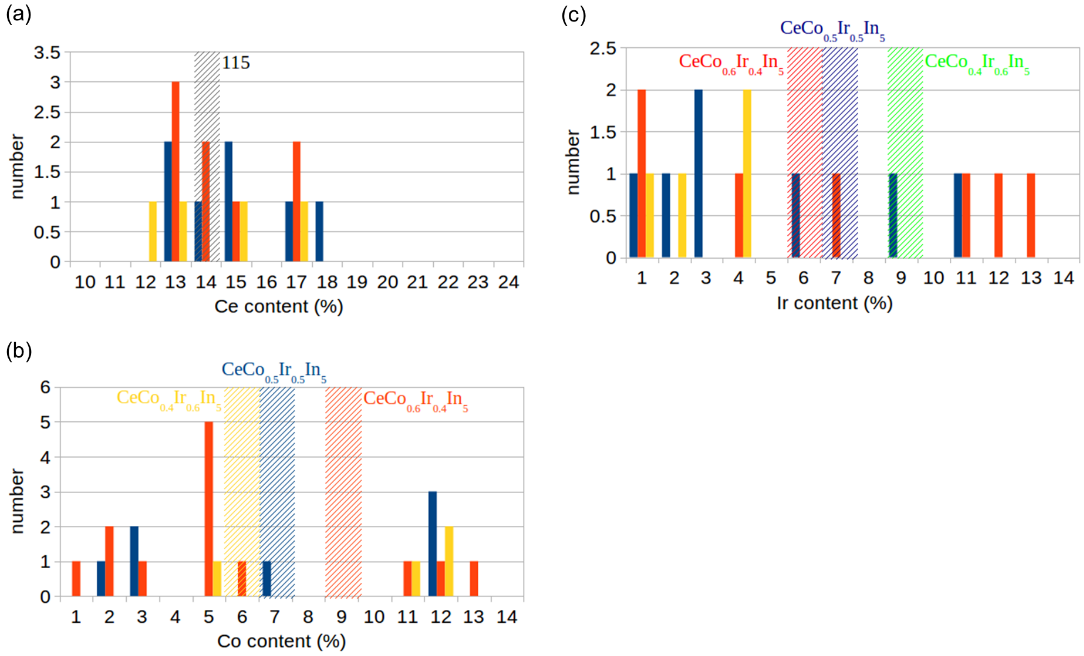

FIGURE 6.3: Number of occurrences of (a) Ce (b) Co and (d) Ir content in samples grown from prealloyed Co and Ir. Determined from EDX spectra at random points of polished sample surfaces. The hatched region indicates the nominal content. In has been left out as the uncertainty in the determination is too large to distinguish between the occurring compositions effectively.

Alloying stoichiometric ratios

A stoichiometric amount of $CeCo_{0.5}Ir_{0.5}In_5$ was alloyed by arc melting. The resulting metal lump was broken apart and a SEM image and an EDX map was obtained (Fig. 6.4). The constituents accumulate in longish grains. The Ce and In content of these grains vary on a large scale (from 14 % up to 20 % for Ce and from 60% to 75 % for In). Therefore, these grains are not single crystal. The Ir content is rather homogeneous around 7 to 8 %. Co accumulates in the grain boundaries.

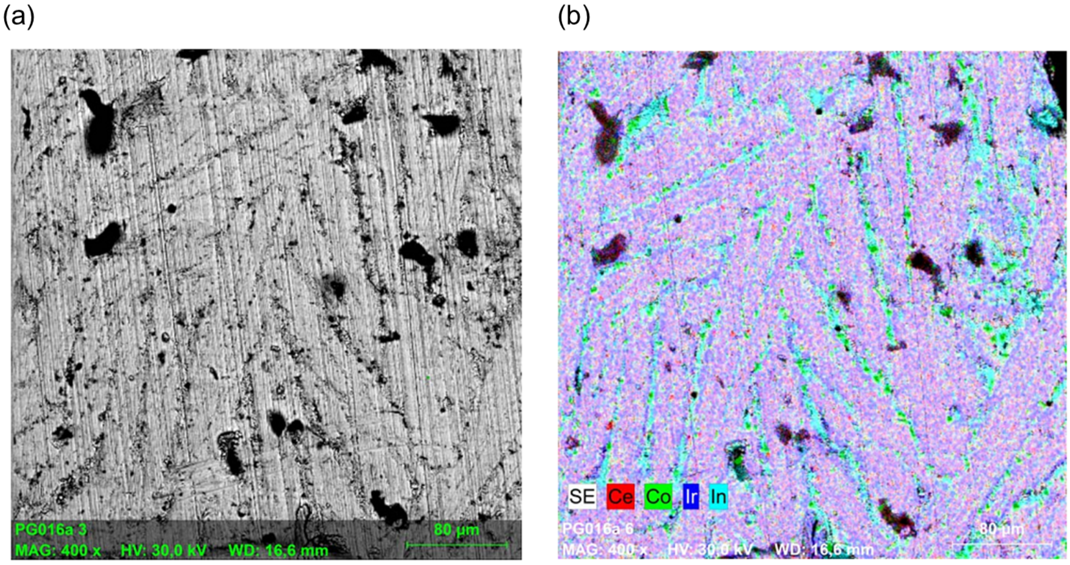

FIGURE 6.4: (a) SEM image and (B) EDX map including the elements Ce, Co, Ir and In of the of the polished surface of stoichiometric $CeCo_{0.5}Ir_{0.5}In_5$ alloy.

Starting materials prealloyed in stoichiometric ratios by arc melting

The previously prealloyed metal lump, together with additional In flux, was put to the furnace. The resulting ratio of materials was 1:0.5:0.5:25. The growth results was characterized by EDX (Fig. 6.5). The phase purity of CeCo$_x$Ir$_{1-x}$In$_5$ is clearly improved. Only little impurities with 16 % Ce and 9 % (Co + Ir) are observed. However, no improvement in the Co/Ir distribution is present.

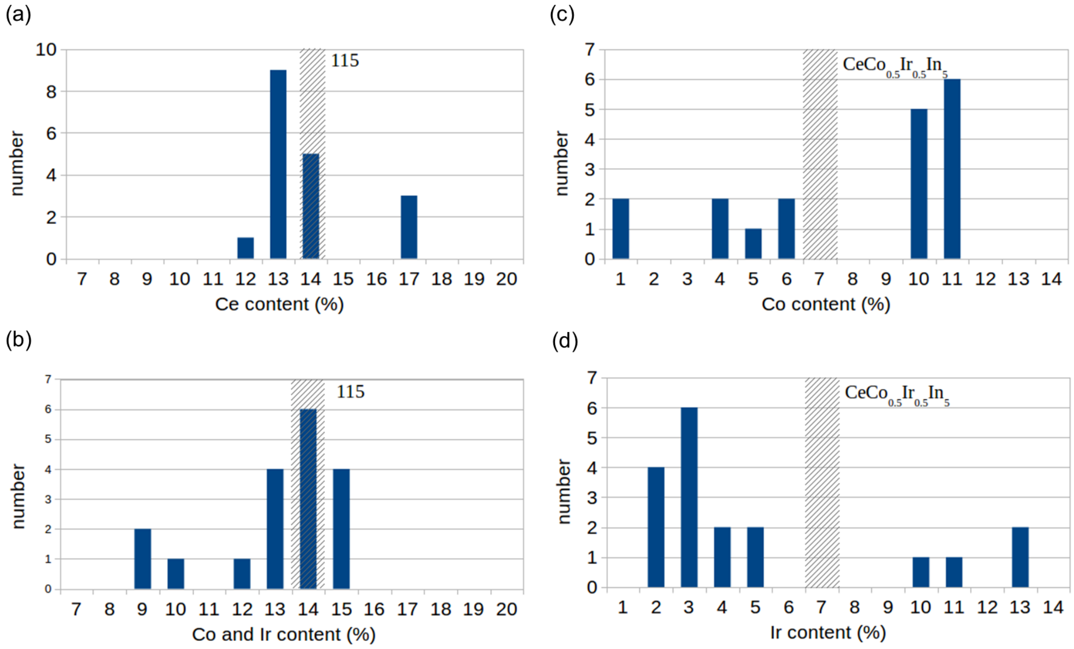

FIGURE 6.5: Number of occurrences of (a) Ce (b) Co and Ir and (d) Ir content in samples grown from stoichiometric CeCo$_{0.5}$Ir$_{0.5}$In$_5$ alloy as starting material. Determined from EDX spectra at random points of polished sample surfaces. The hatched region indicates the nominal content. In has been left out as the uncertainty in the determination is too large too distinguish between the occurring compositions effectively.

Different amount of In flux

The amount of In flux was varied from the initial 1:0.5:0.5:25 to 1:0.5:0.5:50 and 1:0.5:0.5:100. From the EDX characterization (6.6), the probability to crystallize as $CeCo_{0.5}Ir_{0.5}In_5$ clearly improves for the 1:0.5:0.5:50 ratio compared to the initial growth. A higher amount of flux (1:0.5:0.5:100) tends to form non stoichiometric 16 % Ce and 10 % (Co + Ir) phase, even more than the initial amount of flux. A significant improvement in the Co/Ir distribution was not recognized.

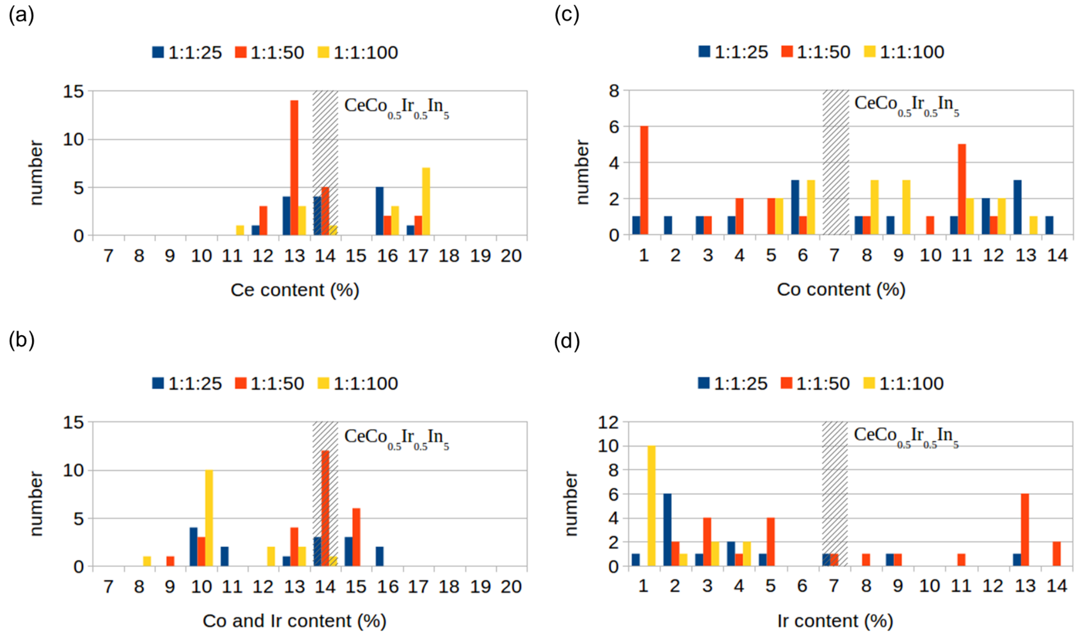

FIGURE 6.6: Number of occurrences of (a) Ce (b) Co and Ir, (c) Co and (d) Ir content in samples grown with different In flux. Determined from EDX spectra at random points of polished sample surfaces. The hatched region indicates the nominal content. In has been left out as the uncertainty in the determination is too large to distinguish between the occurring compositions effectively.

Change of temperature profile

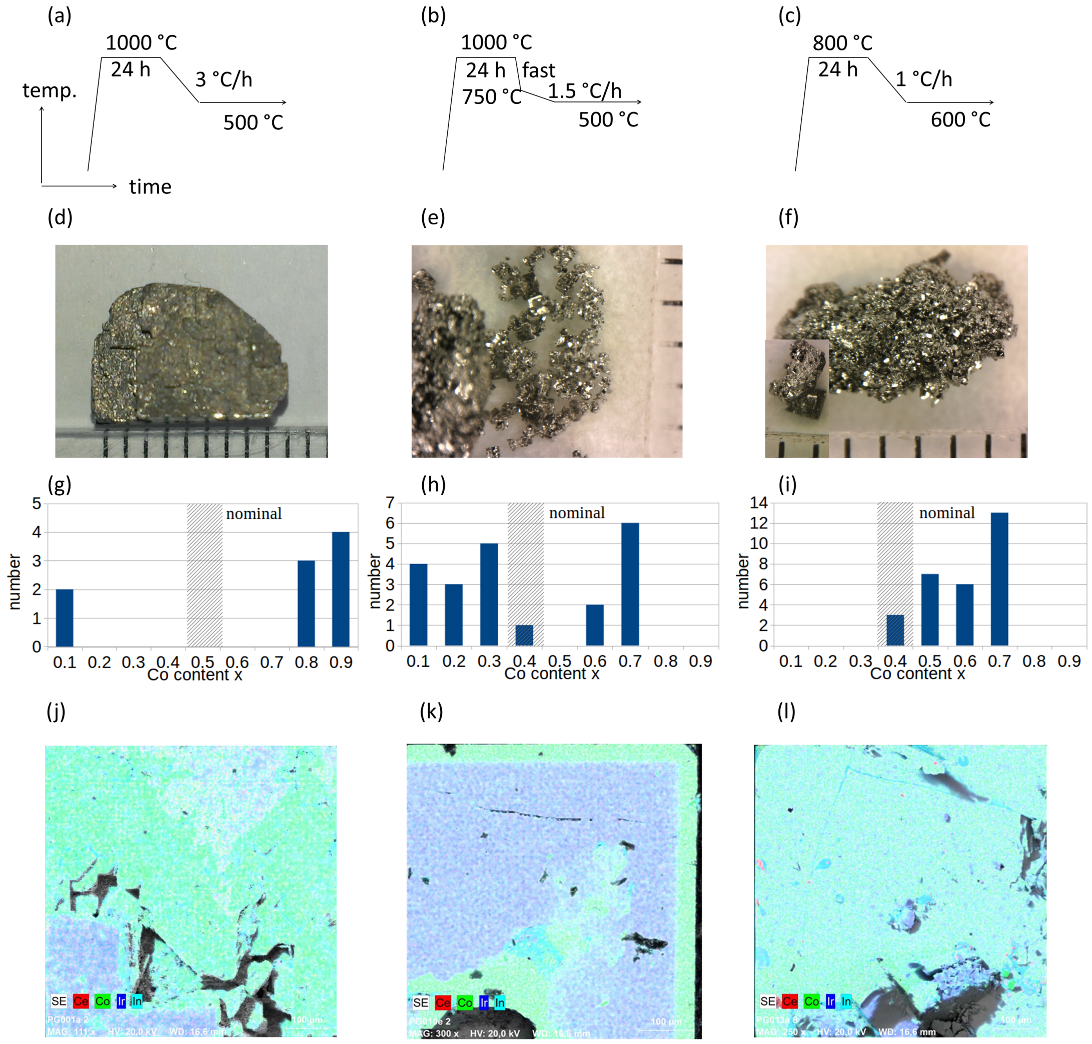

FIGURE 6.7: (a) to (c): Temperature profile for the samples investigated in each column. (d) to (f): Representative pictures of one of the grown crystals. The markers correspond to 1 mm. (g) to (i): Number of occurrences of Co content in samples (only $CeTIn_5$ phase). Determined from EDX spectra at random points of polished sample surfaces. The hatched region indicate the nominal content. (j) to (l): EDX maps of polished surfaces of two different sample including the elements Ce, Co, Ir and In. The nominal composition for the grown crystals in the left column is $CeCo_{0.5}Ir_{0.5}In_5$ and $CeCo_{0.4}Ir_{0.6}In_5$ for the center and right column.

Different temperature profiles have been tested as shown in Fig. 6.7 (a) to (c), where (a) is the initial temperature profile. The second cooling profile has two steps, where the melt is first cooled within hours to 750°C, before a much lower cooling rate is applied. For both growth attempts with changed temperature profile, no single piece was obtained. Instead smaller pieces that were only loosely attached to each other, so they could be easily separated. These pieces are mainly of the $CeCo_{0.5}Ir_{0.5}In_5$ phase. Two step cooling did not achieve an improved Co/Ir distribution. From the EDX map, one can see that only Ir is incorporated in $CeCo_{0.5}Ir_{0.5}In_5$ at first. As the transition from the inner Ir-only region to the outer Co only region is very sharp, one may assume the incorporation of Co only starts when all Ir in the melt is already consumed. Also for the cooling profile in right column in Fig. 6.7, the Co content is different from the nominal value. However, an accumulation is clearly visible for $x = 0.7$. This is the most homogeneous Co/Ir distribution achieved so far. Comparing the growth from the middle column and the right column, it appears that higher cooling rates (either the initial fast cooling from 1000°C to 750°C or the later cooling with 1.5°C/h) favors the incorporation of Ir. For the lower cooling rate of 1°C/h, the rates of Co and Ir incorporation might be on a similar scale and thus the Co/Ir distribution may be controlled in this way. To verify this hypothesis, further investigations with cooling rates $<$ 1°C/h are required.

Annealing after growth

Similar samples from the initial growth attempt and from the growth with prealloyed Co/Ir were annealed. The difference between before annealing and after annealing for 7 day at 600°C are shown in Fig. 6.8.

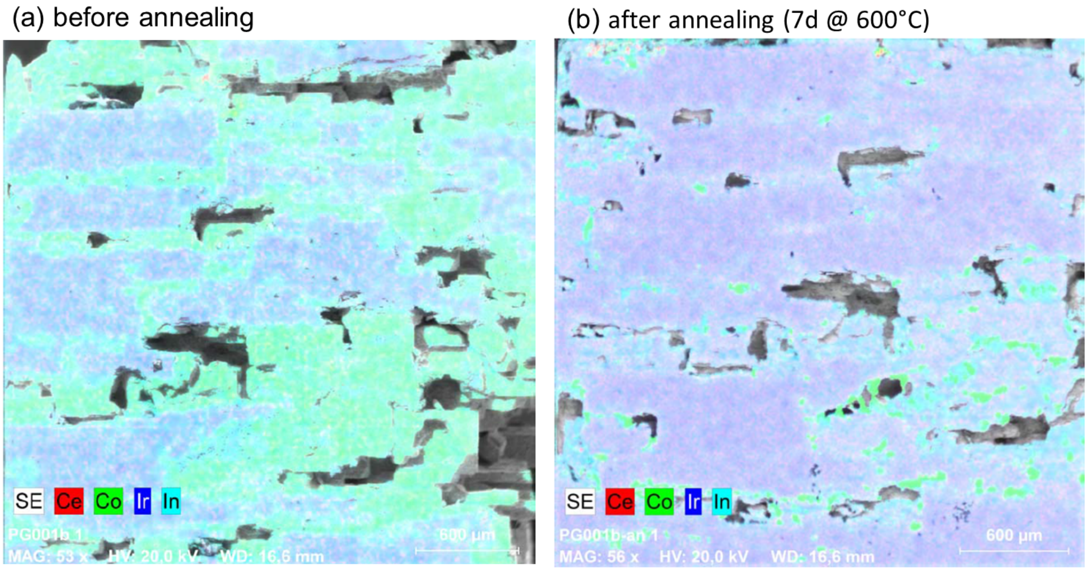

(a) before annealing

(b) after annealing (7d @ 600°C)

FIGURE 6.8: EDX maps of polished surface of a sample (a) before and (b) after annealing for 7 days at 600°C including the elements Ce, Co, Ir and In. The nominal composition is $CeCo_{0.5}Ir_{0.5}In_5$.

The Co/Ir distribution is clearly improved. The large Co-rich areas nearly disappeared, only small Co-rich clusters are left behind. To completely remove these clusters, longer duration and/or higher temperatures are needed. Fig. 6.9 shows the composition of the same sample after annealing for 5 days at 500°C and after an additional 12 days at 550°C. After the first annealing, the $CeCo_{0.5}Ir_{0.5}In_5$ composition is maintained. After the second annealing, a significant amount of 17% Ce and 9 to 10 % Co and Ir is present. Thus, annealing should be limited to less than 12 days and/or temperatures below 500°C. Unfortunately, a meaningful statement on Co/Ir distribution can not be given here, because the whole sample had lacked Ir before. Comparing the annealing of these two samples indicates that the goal to archive better Co/Ir distribution by annealing while maintaining the $\mathrm{CeCo_{0.5}Ir_{0.5}In_5}$ composition, seems to contradict each other.

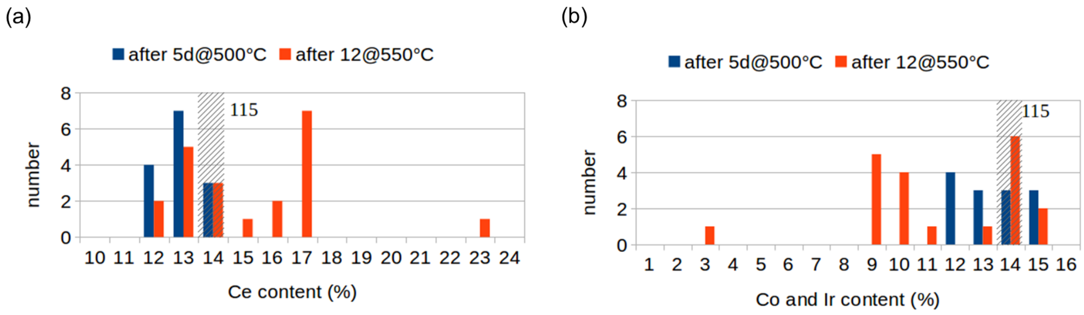

FIGURE 6.9: Number of occurrences of (a) Ce and (b) Co and Ir content of the same sample after annealing for 5 days at 500°C and after 12 additional days at 550°C. Determined from EDX spectra at random points of polished sample surfaces. The hatched region indicates the nominal content. In has been left out as the uncertainty in the determination is too large to distinguish between the occurring compositions effectively.

6.3 X-ray powder diffraction

A sample grown from prealloyed Co/Ir was pulverized and x-ray powder diffraction was performed. For refinement, $CeIn_3$, $CeMIn_5$ and Ce_2MIn_8 phases as well as an In phase for residual In flux were assumed. The refined profile is shown in Fig. 6.10. The distribution of the scattering volume in the powder is 47 % $CeMIn_5$, 33 % Ce_2MIn_8, 20 % In and no $CeIn_3$.

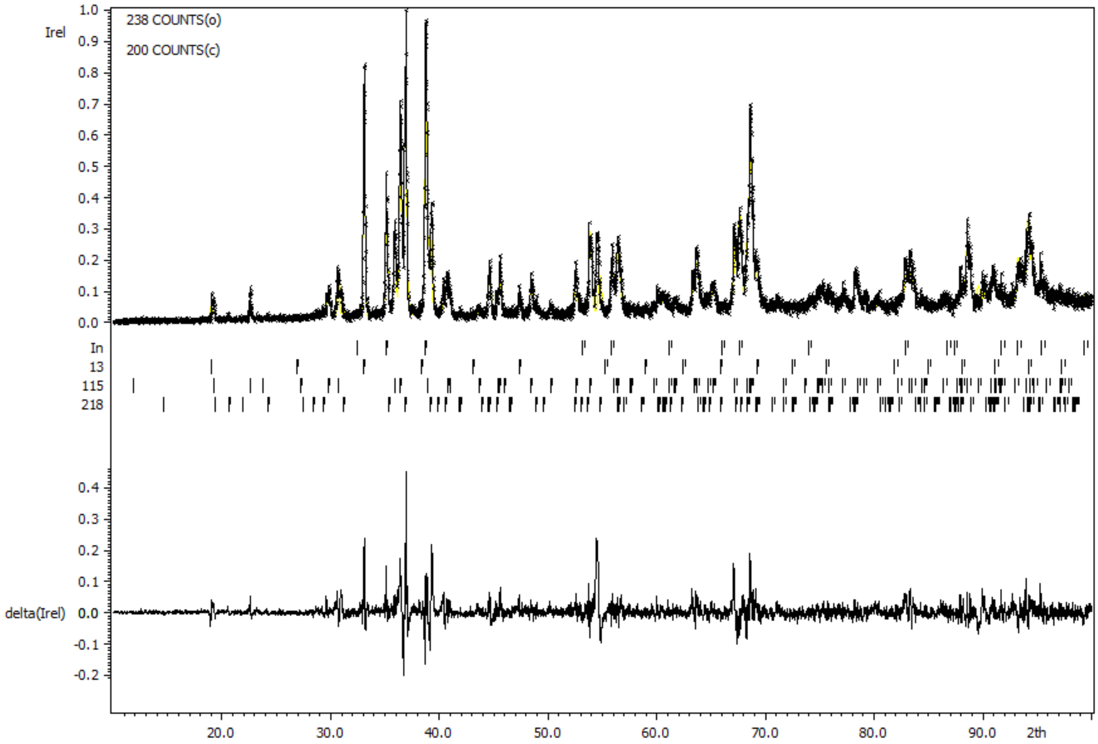

FIGURE 6.10: Powder profile of a sample grown from prealloyed Co/Ir.

6.4 Specific heat

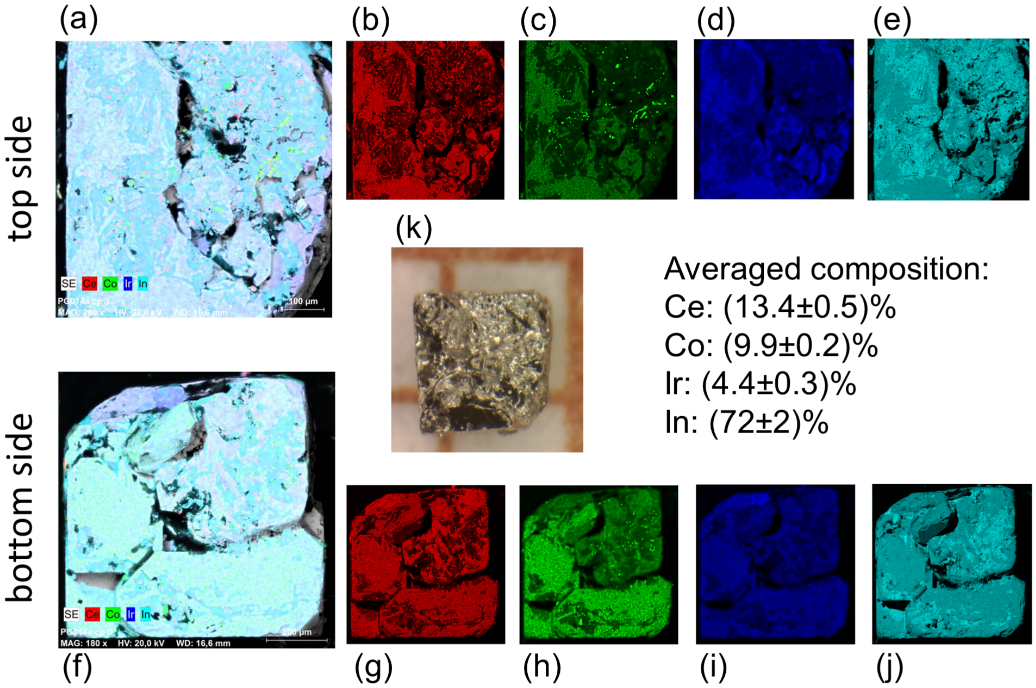

FIGURE 6.11: (a) to (j) EDX maps of the investigated $Co_{0.7}Ir_{0.4}In_5$ sample from both sides. The EDX maps correspond to the element Ce ((b) and (g)), Co ((c) and (h)), Ir ((d) and (i)) and In ((e) and (j)). (a) and (f) show a combination of all four elements. (k) shows an optical microscopy image of top side of the sample.

A sample grown with the parameters shown in Fig. 6.7 (right column) was investigated. The sample size was 1x1x0.2 mm. EDX maps of the sample from both sides as well as an optical microscope image is shown in Fig. 6.11. EDX indicates a Co/Ir ratio of 0.7:0.3 over the whole sample. Single crystal diffraction yielded lattice constants of a = (4.6381 $\pm$ 0.0022) Å and c = (7.5681 $\pm$ 0.0046) Å. Comparing the a lattice constant to literature values [136] ($CeCoIn_5$: a = 4.61292 Å; $CeIrIn_5$: a = 4.674 Å) by Vegard's law yields a Co/Ir ratio of 0.6. The c lattice constant measured here is larger than the literature values for both $CeCoIn_5$ and $CeIrIn_5$ (c = 7.55513 Å and c = 7.501 Å, respectively).

Specific heat data are shown in Fig. 6.12. A single jump is observed at T_c = 1.5 K. No sign of phase separation in a $CeCoIn_5$ and $CeIrIn_5$ phase is visible. This points against the existence of a miscibility gap for $CeCo_xIr_{1-x}In_5$.

For comparison, the results from [5] on pure $CeCoIn_5$ and $CeIrIn_5$ can be used. The width of the jump is comparable with that of $CeCoIn_5$ and $CeIrIn_5$. The data was fitted in the normal state by a linear temperature dependence that yielded γ = 0.291(5) J/molK^2, somewhat close to the value for $CeCoIn_5$ [5]. Note that an offset had to be used for the linear fit. This might be due to the presence of residual In flux. For the superconducting

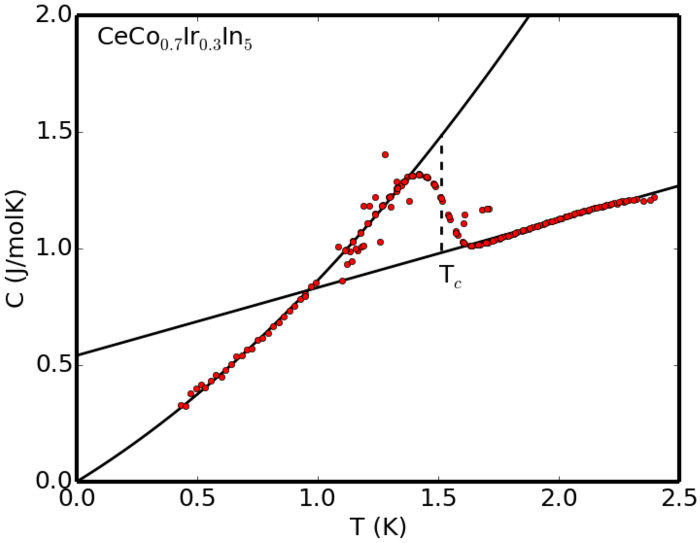

FIGURE 6.12: Specific heat measurement of the Co$_{0.7}$Ir$_{0.3}$In$_5$. The dashed line indicates the transition temperature. The fitted solid lines are described in the text.

state, $C = \gamma_0 T + aT^2$ was fitted as in [5]. The linear term corresponds to the impurity band that forms in the linear nodes of the superconducting energy gap. It can be used as a measure for sample quality. The quadratic term corresponds to lines of nodes in the energy gap. The fit yields $\gamma_0 = 0.63(3)$ J/molK^2 and $a = 0.22(2)$ J/molK^3. This indicates a worse sample quality as in [5], but still on the same order of magnitude. The slightly smaller T_c compared to the phase diagram may be explained by this. a is very close to the value of CeCoIn$_5$. This could be a hint for the existence of two distinct superconducting phases. Further measurements on samples with larger Ir content are highly desirable. Comparing the size of the jump, the value fitted here is rather well matched by a linear interpolation between the values for CeCoIn$_5$ and CeIrIn$_5$.

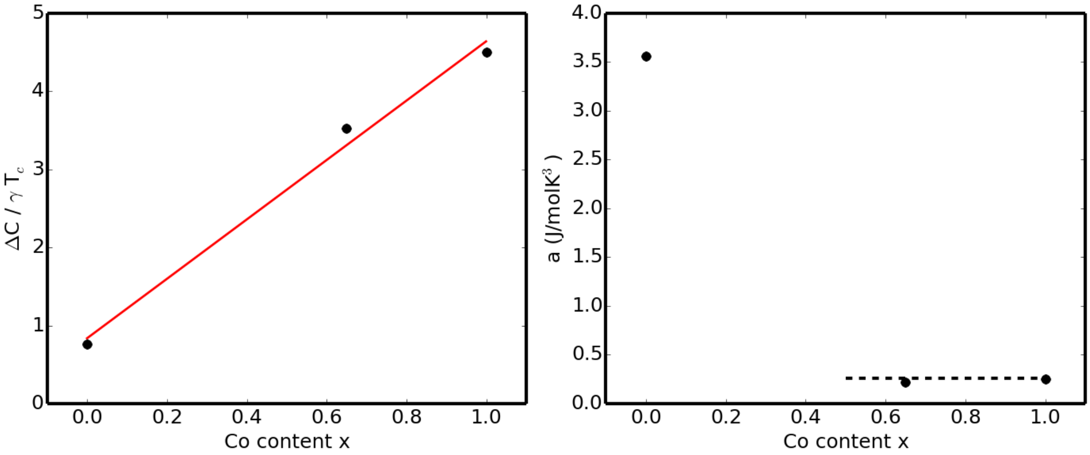

FIGURE 6.13: Left: $\Delta C/\gamma T_c$ versus the composition. The red line is a linear fit. Right: coefficient a in $C = \gamma_0 T + aT^2$ versus the composition. The dashed line is a guide for the eye. Values for $x = 0, 1$ are from [5].

6.5 Summary

Initial growth attempts showed problems with the occurrence of non stoichiometric phases and clustering of Co- or Ir-rich clusters. Several ideas were followed to overcome this. For improvement of the $CeCo_{1-x}Ir_xIn_5$ phase purity, prealloying of the starting materials and subsequent growth as well as a flux ratio 1:1:50 are promising. To achieve control of the Co/Ir ratio, work on the cooling profile, especially the cooling rate, is advised. To achieve sufficient scattering volume for inelastic neutron scattering, alignment of multiple crystals will be necessary. The results on $CeCo_{0.7}Ir_{0.4}In_5$ are encouraging that mixed crystals of $CeCo_{1-x}Ir_xIn_5$ can be grown. No hints of a miscibility gap were detected. Reliable growth parameters are not established yet, but are expected to be found by an reasonable amount of further work.

Chapter 7

Summary

For $CeCu_2Ge_2$, it was found that the magnetic structure in the AF1 phase is well described as a spin density wave with ordered moments in $[1\bar{1}0]$ direction. A distinction between structures with one or two propagation vectors $\vec{\tau}_{1,2}$ = (0.285 0.285 ±0.544) could not be made, although the 1-k structure is preferred. In all cases, the moments are significantly reduced compared to the CEF value. For the Kondo temperature, the data suggest T_K = 4.3 K, slightly smaller than the previous reported values. The reduction of the ordered magnetic moments appears rather large considering $T_K \approx T_N$.

When magnetic field is applied along $[1\bar{1}0]$ direction, the AF1 phase is continuously suppressed at high temperature in favor of the C-phase with a yet unknown order. At low temperature, AF1 is stable until 7.5 - 7.8 T. Then an 1st order transition to the AF2 happens. AF2 is an elliptical helix with a single propagation vector $\vec{\tau}_{AF2}$ = (0.34 0.27 0.55). The ordered moment is similar to the 1-k SDW for AF1. Above T_N in zero field, short range order was observed, hinting competition of AF1 and AF2. It is assumed that both structures correspond to different nesting properties of the Fermi surface. The ferromagnetic sub lattices in AF1 appear to be more unstable than those of AF2, hence causing the phase transition in magnetic field. A change in the Fermi surface is further indicated by different effective Landé factors in the AF1 (g^{eff} = 0.36) and AF2 (g^{eff} = 0.525) phases. The effective Landé factor is a consequence of the RKKY character of the electronic system and therefore sensitive to the electronic system.

The AF2 phase eventually vanishes at 12.6 T and is replaced by the C-phase. So far, no propagation vector for the C-phase could be found, but spin wave excitations on a similar energy scale were detected.

From the zero field dispersion, the strength of the next nearest neighbor RKKY interactions was extracted using the simplest antiferromagnetic model, yielding $2SJ_1$ = (-0.042

± 0.007) meV (basal plane) and $2SJ_2$ = (-0.18 ± 0.01) meV (body diagonal). After considering the Kondo effect, the calculated ordering temperature is in remarkable well agreement with the observed value. Comparing the RKKY interaction to $CeCu_2Si_2$ and $CeNi_2Ge_2$ reveals a strong enhancement of the interaction in the basal plane going from antiferromagnetism ($CeCu_2Ge_2$) to superconductivity ($CeCu_2Si_2$) and finally paramagnetism ($CeNi_2Ge_2$). This new finding appears to be an important puzzle piece for the understanding of the CeT_2X_2 family as it suggests a dependence of the aniosotropy of the RKKY interaction from the hybridization strength of the 4f orbital and the conduction band.

In $CeCu_2(Si_{0.55}Ge_{0.45})_2$ the phase diagram with magnetic field in $[1\bar{1}0]$ direction was investigated. The domain population changes in the LAF and MAF phases at around 2 T in favor of the domains producing magnetic satellites out of the [110]/[001] scattering plane. The specific heat indicates that LAF and MAF are stable up to at least 8 T . The HAF phase is continuously suppressed by the magnetic field. Critical exponents for temperature and magnetic field scaling agree with the mean field values. An additional transition that is very stable in the magnetic field points to the existence of an unknown magnetic phase that replaces the HAF phase. The situation is rather similar to that in $CeCu_2(Si_{0.55}Ge_{0.45})_2$. One can conclude, that if magnetic field is capable of inducing a phase transition in $CeCu_2(Si_{1-x}Ge_x)_2$, also much larger field is required.

For the $CeTIn_5$ compounds, superconducting samples were grown, i.e. $CeCo_xIr_{1-x}In_5$. The results indicate that no miscibility gap is present. For further neutron scattering studies, additional work will be required to make the growth process more reliable. Important directions how to proceed so, were developed from the growth attempts in this work.

Bibliography

[1] G. Stewart. Rev. Mod. Phys. 56(4), 755–787 (1984)

[2] K. Andres, J. E. Graebner, H. R. Ott. Phys. Rev. Lett. 35, 1779–1782 (1975)

[3] W. Lieke. J. Appl. Phys. 53(3), 2111 (1982)

[4] F. Steglich, J. Aarts, C. Bredl, W. Lieke, D. Meschede, W. Franz, H. Schäfer. Phys. Rev. Lett. 43(25), 1892–1896 (1979)

[5] R. Movshovich, M. Jaime, J. D. Thompson, C. Petrovic, Z. Fisk, P. G. Pagliuso, J. L. Sarrao. Phys. Rev. Lett. 86, 5152–5155 (2001)

[6] T. Takeuchi, T. Inoue, K. Sugiyama, D. Aoki, Y. Tokiwa, Y. Haga, K. Kindo, Y. Onuki. J. Phys. Soc. Japan. 70(3), 877–883 (2001)

[7] H. Löhneysen, C. Pfleiderer, T. Pietrus, O. Stockert, B. Will. Phys. Rev. B 63(13), 134411 (2001)

[8] D. Aoki, W. Knafo, I. Sheikin. C. R. Phys. 14(1), 53–77 (2013)

[9] M. Takashita, H. Aoki, T. Terashima, S. Uji, K. Maezawa, R. Settai, Y. Onuki. J. Phys. Soc. Japan. 65(2), 515–524 (1996)

[10] É. D. T. d. Lacheisserie, D. Gignoux, M. Schlenker. Magnetism. Springer (2005). ISBN 9780387229676

[11] P. Fulde, M. Loewenhaupt. Adv. Phys. 34(5), 589–661 (1985)

[12] M. T. Hutchings. In F. Seitz, D. Turnbull (eds.), Point-Charge Calculations of Energy Levels of Magnetic Ions in Crystalline Electric Fields, vol. 16 of Solid State Physics, 227 – 273. Academic Press (1964)

[13] M. a. Ruderman, C. Kittel. Phys. Rev. 96(3), 99–102 (1954)

[14] T. Kasuya. Prog. Theo. Phys. 16(1), 58–63 (1956)

[15] K. Yosida. Phys. Rev. 106(I), 893–898 (1957)

[16] P. Coleman. AIP Conf. Proc. 629(1), 79–160 (2002)

[17] J. Kondo. Prog. Theo. Phys. 32(1), 37–49 (1964)

[18] S. Doniach. Phys. B+C 91, 231–234 (1977)

[19] S. Blundell. Magnetism in condensed matter. Oxford Univ. Press (2001)

[20] K. Yosida. Theory of magnetism: Edition en anglais. Solid-State Sci.s Series. Springer (1996). ISBN 9783540606512

[21] W. Rieger, E. Parthe. Monatsh. Chem. 100(2), 444–454 (1969)

[22] T. Endstra, G. Nieuwenhuys, J. Mydosh. Phys. Rev. B 48(13), 9595–9605 (1993)

[23] B. Grier, J. Lawrence, V. Murgai, R. Parks. Phys. Rev. B 29(5), 2664–2672 (1984)

[24] A. Loidl, K. Knorr, G. Knopp, A. Krimmel, R. Caspary, A. Böhm, G. Sparn, C. Geibel, F. Steglich, A. Murani. Phys. Rev. B 46(15), 9341–9351 (1992)

[25] O. Stockert, E. Faulhaber, G. Zwicknagl, N. Stüß er, H. Jeevan, M. Deppe, R. Borth, R. Küchler, M. Loewenhaupt, C. Geibel, F. Steglich. Phys. Rev. Lett. 92(13), 136401 (2004)

[26] E. Faulhaber, O. Stockert, M. Rheinstädter, M. Deppe, C. Geibel, M. Loewenhaupt, F. Steglich. JMMM 272-276, 44–45 (2004)

[27] O. Stockert, M. Deppe, E. Faulhaber, H. Jeevan, R. Schneider, N. Stüß er, C. Geibel, M. Loewenhaupt, F. Steglich. Phys. B: Cond. Mat. 359-361, 349–356 (2005)

[28] E. Faulhaber, O. Stockert, B. Grenier, B. Ouladdiaf, M. Deppe, C. Geibel, F. Steglich, M. Loewenhaupt. Phys. B: Cond. Mat. 378-380, 78–79 (2006)

[29] P. Gegenwart, C. Langhammer, C. Geibel, R. Helfrich, M. Lang, G. Sparn, F. Steglich, R. Horn, L. Donnevert, A. Link, W. Assmus. Phys. Rev. Lett. 81(7), 1501–1504 (1998)

[30] O. Stockert, J. Arndt, E. Faulhaber, C. Geibel, H. S. Jeevan, S. Kirchner, M. Loewenhaupt, K. Schmalzl, W. Schmidt, Q. Si, F. Steglich. Nat. Phys. 7(2), 119–124 (2010)

[31] G. Knopp, A. Loidl, U. Gottwick, C. D. Bredl, F. Steglich, R. Caspary, A. P. Murani. JMMM 74, 341–346 (1988)

[32] B. Fåk, J. Flouquet, G. Lapertot, T. Fukuhara, H. Kadowaki. J. Phys.: Cond. Mat. 12(25), 5423–5435 (2000)

[33] H. Kadowaki, B. Fåk, T. Fukuhara, K. Maezawa, K. Nakajima, M. A. Adams, S. Raymond, J. Flouquet. Phys. Rev. B 68(14), 140402 (2003)

[34] T. Ebihara, Y. Sugiyama, Y. Narumi, Y. Sawai, K. Kindo, E. O'Farrell, M. Sutherland, N. Harrison. J. Phys. Conf. Ser. 391, 012010 (2012)

[35] G. Knopp, A. Loidl, K. Knorr, L. Pawlak, M. Duczmal, R. Caspary, U. Gottwick, H. Spille, F. Steglich, a. P. Murani. Z. Phys. B Cond. Mat. 77(1), 95–104 (1989)

[36] A. Krimmel, A. Loidl, H. Schober, P. C. Canfield. Phys. Rev. B 55(10), 6416–6420 (1997)

[37] G. Knopp, H. Spille, A. Loidl, K. Knorr, U. Rauchschwalbe, R. Felten, G. Weber, F. Steglich, A. P. Murani. JMMM 63-64, 88–90 (1987)

[38] M. Loewenhaupt, E. Faulhaber, A. Schneidewind, M. Deppe, K. Hradil. J. Appl. Phys. 111(7), 07E124 (2012)

[39] R. Felten, G. Weber, H. Rietschel. JMMM 63-64, 383–385 (1987)

[40] H. Mendpara, D. A. Joshi, A. K. Nigam, A. Thamizhavel. JMMM 377, 325–333 (2015)

[41] F. R. de Boer, J. C. P. Klaasse, P. A. Veenhuizen, A. Böhm, C. D. Bredl, U. Gottwick, H. M. Mayer, L. Pawlak, U. Rauchschwalbe, H. Spille, F. Steglich. JMMM 63-64, 91–94 (1987)

[42] O. Trovarelli, M. Weiden, R. Müller-Reisener, M. Gómez-Berisso, P. Gegenwart, M. Deppe, C. Geibel, J. Sereni, F. Steglich. Phys. Rev. B 56(2), 678–685 (1997)

[43] G. Zwicknagl. J. Low. Temp. Phys. 147(3-4), 123–134 (2007)

[44] D. Jaccard, H. Wilhelm, K. Alami-Yadri, E. Vargoz. Phys. B: Cond. Mat. 259-261, 1–7 (1999)

[45] G. Knebel, C. Eggert, D. Engelmann, R. Viana, A. Krimmel, M. Dressel, A. Loidl. Phys. Rev. B 53(17), 11586–11592 (1996)

[46] A. Krimmel, A. Loidl. Phys. B: Cond. Mat. 234-236(0921), 877–879 (1997)

[47] M. Deppe. Ph.D. thesis, TU Dresden (2004)

[48] N. Oeschler, M. Deppe, E. Lengyel, R. Borth, P. Gegenwart, G. Sparn, C. Geibel, F. Steglich. Phys. Rev. B 71(9), 094409 (2005)

[49] H. Q. Yuan, F. M. Grosche, M. Deppe, C. Geibel, G. Sparn, F. Steglich. Sci. 302(5653), 2104–7 (2003)

[50] A. T. Holmes, D. Jaccard, K. Miyake. J. Phys. Soc. Japan. 76(5), 051002 (2007)

[51] H. Yuan, M. Deppe, G. Sparn, F. M. Grosche, C. Geibel, F. Steglich. Acta Phys. Pol. B 34(2), 533 – 536 (2003)

[52] F. Thomas, J. Thomasson, C. Ayache, C. Geibel, F. Steglich. Phys. B: Cond. Mat. 186-188, 303–306 (1993)

[53] A. T. Holmes, A. Demuer, D. Jaccard. Acta Phys. Pol. B 34(2), 567 (2003)

[54] N. D. Mathur, F. M. Grosche, S. R. Julian, I. R. Walker, D. M. Freye, R. K. W. Haselwimmer, G. G. Lonzarich. Nature 394(6688), 39–43 (1998)

[55] A. Onodera, S. Tsuduki, Y. Ohishi, T. Watanuki, K. Ishida, Y. Kitaoka, Y. Onuki. Solid. State Comm. 123(3-4), 113–116 (2002)

[56] A. Holmes, D. Jaccard, K. Miyake. Phys. Rev. B 69(2), 024508 (2004)

[57] Y. Onishi, K. Miyake. J. Phys. Soc. Japan. 69(12), 3955–3964 (2000)

[58] G. Knebel, C. Eggert, T. Schmidt, A. Krimmel, M. Dressel, A. Loidl. Phys. B: Cond. Mat. 230-232, 593–595 (1997)

[59] A. Loidl, A. Krimmel, K. Knorr, G. Sparn, M. Lang, C. Geibel, S. Horn, A. Grauel, F. Steglich, B. Welslau, N. Grewe, H. Nakotte, F. R. de Boer, A. P. Murani. Ann. Phys. 504(2), 78–91 (1992)

[60] B. Welslau, N. Grewe. Phys. B: Cond. Mat. 165-166, 387–388 (1990)

[61] N. Büttgen, H.-A. von Nidda, A. Loidl. Phys. B: Cond. Mat. 230-232, 590–592 (1997)

[62] D. K. Singh, A. Thamizhavel, J. W. Lynn, S. Dhar, J. Rodriguez-Rivera, T. Herman. Sci. rep. 1, 117 (2011)

[63] K. Sugiyama, T. Miyauchi, Y. Ota, T. Yamada, Y. Oduchi, N. Dung, Y. Haga, T. Matsuda, M. Hagiwara, K. Kindo, T. Takeuchi, R. Settai, Y. Onuki. Phys. B: Cond. Mat. 403(5-9), 769–771 (2008)

[64] B. Zeng, Q. R. Zhang, D. Rhodes, Y. Shimura, D. Watanabe, R. E. Baumbach, P. Schlottmann, T. Ebihara, L. Balicas. Phys. Rev. B 90(15), 155101 (2014)

[65] M. Doerr, S. Granovsky, M. Rotter, M. Loewenhaupt, A. Schneidewind, Z.-S. Wang. Phys. Proc. 75, 572 – 579 (2015)

[66] E. Faulhaber. Ph.D. thesis, TU Dresden (2008)

[67] C. Petrovic, R. Movshovich, M. Jaime, P. G. Pagliuso, M. F. Hundley, J. L. Sarrao, Z. Fisk, J. D. Thompson. EPL Europhys. Lett. 53(3), 354–359 (2001)

[68] C. Petrovic, P. G. Pagliuso, M. F. Hundley, R. Movshovich, J. L. Sarrao, J. D. Thompson, Z. Fisk, P. Monthoux. J. Phys.: Condens. Matter 337, 16 (2001)

[69] E. G. Moshopoulou, Z. Fisk, J. L. Sarrao, J. D. Thompson. J. Solid State Chem. 158(1), 25–33 (2001)

[70] J. M. Lawrence. Phys. Rev. B 22(9), 4379–4388 (1980)

[71] R. Kumar, A. Cornelius, J. Sarrao. Phys. Rev. B 70(21), 214526 (2004)

[72] P. Pagliuso, R. Movshovich, a.D. Bianchi, M. Nicklas, N. Moreno, J. Thompson, M. Hundley, J. Sarrao, Z. Fisk. Phys. B: Cond. Mat. 312-313, 129–131 (2002)

[73] P. Pagliuso, C. Petrovic, R. Movshovich, D. Hall, M. Hundley, J. Sarrao, J. Thompson, Z. Fisk. Phys. Rev. B 64(10), 100503 (2001)

[74] G. Knebel, D. Aoki, J.-P. Brison, J. Flouquet. J. Phys. Soc. Japan. 77(11), 114704 (2008)

[75] M. Nicklas, V. Sidorov, H. Borges, P. Pagliuso, J. Sarrao, J. Thompson. Phys. Rev. B 70(2), 020505 (2004)

[76] C. Stock, C. Broholm, J. Hudis, H. Kang, C. Petrovic. Phys. Rev. Lett. 100(8), 087001 (2008)

[77] S. Kambe, H. Sakai, Y. Tokunaga, R. E. Walstedt. Phys. Rev. B 82(14), 144503 (2010)

[78] S. Kawasaki, G.-q. Zheng, H. Kan, Y. Kitaoka, H. Shishido, Y. Onuki. Phys. Rev. Lett. 94(3), 037007 (2005)

[79] J. D. Thompson, Z. Fisk. J. Phys. Soc. Japan. 81(1), 011002 (2011)

[80] A. B. Gokhale, G. J. Abbaschian. Bull. Alloy Phase Diagr. 10(2), 142–146 (1989)

[81] J. a. Zan, T. Yuen, C. L. Lin, X.-Y. Huang, J. Li. J. Appl. Phys. 93(10), 8340 (2003)

[82] H. Hegger, C. Petrovic, E. Moshopoulou, M. Hundley, J. Sarrao, Z. Fisk, J. Thompson. Phys. Rev. Lett. 84(21), 4986–4989 (2000)

[83] A. L. Cornelius, P. G. Pagliuso, M. F. Hundley, J. L. Sarrao. Phys. Rev. B 64(14), 144411 (2001)

[84] K. Uhlířová. Ph.D. thesis, Charles University in Prague (2010)

[85] J. S. Hwang, K. J. Lin, C. Tien. Rev. Sci. Instrum. 68(1997), 94 (1997)

[86] P. J. Mohr, B. N. Taylor, D. B. Newell. Rev. Mod. Phys. 84(4), 1527–1605 (2012)

[87] Brückel. In M. Angst, T. Brückel, R. D., R. Zorn (eds.), Scattering Methods for Condensed Matter Research: Towards Novel Application at Future Sources. Forschungszentrum Jülich, Jülich (2012)

[88] S. Lovesey. Theory of neutron scattering from condensed matter. No. 1 in International series of monographs on physics. Clarendon Press (1984)

[89] E. Ressouche. École thématique de la Société Française de la Neutronique 13, 02001 (2014)

[90] G. Shirane, S. M. Shapiro, J. M. Tranquada. Neutron Scattering with a Triple-Axis Spectrometer. Cambridge University Press (2002). ISBN 9780511534881. Cambridge Books Online

[91] E. F. Bertaut. Acta Crystallogr. Sec. A 24(1), 217–231 (1968)

[92] A. Wills. J. Phys. IV 11(PR9), Pr9–133–Pr9–158 (2001)

[93] J. M. Perez-Mato, J. L. Ribeiro, V. Petricek, M. I. Aroyo. J. Phys.: Cond. Mat. 24, 163201 (2012)

[94] J. Rodríguez-Carvajal. Phys. B: Cond. Mat. 192(1-2), 55–69 (1993)

[95] H. T. Stokes, B. J. Campbell, R. Cordes. Acta Crystallogr. Sec. A 69(4), 388–395 (2013)

[96] B. J. Campbell, H. T. Stokes, D. E. Tanner, D. M. Hatch. J. Appl. Crystallogr. 39(4), 607–614 (2006)

[97] V. Petříček, M. Dušek, L. Palatinus. Z. Kristallogr. 229(5) (2014)

[98] A. T. Brunger. Nature 335, 472–475 (1992)

[99] R. Schedler, U. Witte, M. Loewenhaupt, J. Kulda. Phys. B: Cond. Mat. 335(1-4), 41–43 (2003)

[100] Y. A. Izyumov, S. V. Maleev. JETP 14(5), 1168–1171 (1962)

[101] Y. A. Izyumov. Sov. Phys. Usp. 6(3), 359 (1963)

[102] M. Blume. Phys. Rev. 130(5), 1670–1676 (1963)

[103] M. Blume. Phys. Rev. 133(5A), A1366–A1369 (1964)

[104] R. I. Schermer, M. Blume. Phys. Rev. 166(2), 554–561 (1968)

[105] U. Fano. Rev. Mod. Phys. 29(1), 74–93 (1957)

[106] Y. Su, K. Nemkovskiy, S. Demirdiş. JLSRF 1, A27 (2015)

[107] O. Schärpf, H. Capellmann. Physica Status Solidi (a) 135(2), 359–379 (1993)

[108] W. Schweika. J. Phys. Conf. Ser. 211, 012026 (2010)

[109] A. Schneidewind, P. Čermák. JLSRF 1, A12 (2015)

[110] O. Stockert, M. Enderle, H. v. Löhneysen. Phys. Rev. Lett. 99(23), 237203 (2007)

[111] M. Popovici. Acta Crystallogr. Sec. A 31(4), 507–513 (1975)

[112] H. Wilhelm, T. Lühmann, T. Rus, F. Steglich. Rev. Sci. Instrum. 75(8), 2700–2705 (2004)

[113] O. V. Kovalev. Representation of Crystallographic Space Groups. Taylor & Francis (1993). ISBN 9782881249341

[114] N. van Dijk, B. Fåk, T. Charvolin, P. Lejay, J. Mignot. Phys. Rev. B 61(13), 8922–8931 (2000)

[115] C. Broholm, J. K. Kjems, G. Aeppli, Z. Fisk, J. L. Smith, S. M. Shapiro, G. Shirane, H. R. Ott. Phys. Rev. Lett. 58(9), 917–920 (1987)

[116] N. van Dijk, B. Fåk, T. Charvolin, P. Lejay, J. Mignot, B. Hennion. Phys. B: Cond. Mat. 241-243, 808–810 (1998)

[117] W. Knafo, S. Raymond, B. F k, G. Lapertot, P. C. Canfield, J. Flouquet. J. Phys.: Cond. Mat. 15(22), 3741–3749 (2003)

[118] J. C. Slater. Phys. Rev. 35(5), 509–529 (1930)

[119] T. Holstein, H. Primakoff. Phys. Rev. 58(12), 1098–1113 (1940)

[120] F. Dyson. Phys. Rev. 102(1930), 1230–1244 (1956)

[121] F. Dyson. Phys. Rev. 102(5), 1217–1230 (1956)

[122] F. Bloch. Z. Phys. B Cond. Mat. 61(3-4), 206–219 (1930)

[123] S. Petit. École thématique de la Société Française de la Neutronique 12, 105–121 (2011)

[124] A. Furrer, T. Strässle, J. Mesot. Neutron Scattering in Condensed Matter Physics. Series on neutron techniques and applications. World Scientific (2009). ISBN 9789810248314

[125] S. Lovesey. Theory of neutron scattering from condensed matter. No. 2 in International series of monographs on physics. Clarendon Press (1984)

[126] R. W. Erwin, J. W. Lynn, J. J. Rhyne, H. S. Chen. J. Appl. Phys. 57(1985), 3473–3475 (1985)

[127] A. Yaouanc, P. de Réotier. Muon Spin Rotation, Relaxation, and Resonance: Applications to Condensed Matter. International Series of Monographs on Physics. OUP Oxford (2011). ISBN 9780199596478

[128] D. Feng, G. Jin. Introduction to Condensed Matter Physics. Bd. 1. World Scientific (2005). ISBN 9789812387110

[129] O. Stockert, J. Arndt, A. Schneidewind, H. Schneider, H. Jeevan, C. Geibel, F. Steglich, M. Loewenhaupt. Phys. B: Cond. Mat. 403(5-9), 973–976 (2008)

[130] P. Monthoux, D. Pines, G. G. Lonzarich. Nature 450(7173), 1177–83 (2007)

[131] T. Balcerzak. Phys. Status Solidi C 3(1), 212–215 (2006)

[132] G. Bossé, L. S. Bilbro, R. V. Aguilar, L. Pan, W. Liu, A. V. Stier, Y. Li, L. H. Greene, J. Eckstein, N. P. Armitage. Phys. Rev. B 85(15), 155105 (2012)

[133] M. Deppe, R. Borth, C. Geibel, P. Hinze, N. Oeschler, O. Stockert, F. Steglich. JMMM 272-276, 40–41 (2004)

[134] O. Stockert, M. Deppe, C. Geibel. Acta Phys. Pol. B 34(2), 963–966 (2003)

[135] M. Kratochvilova, M. Dusek, K. Uhlirova, a. Rudajevova, J. Prokleska, B. Vondrackova, J. Custers, V. Sechovsky. J. Crys. Growth 397, 47–52 (2014)

[136] E. Moshopoulou, J. Sarrao, P. Pagliuso, N. Moreno, J. Thompson, Z. Fisk, R. Ibberson. Appl. Phys. A Mater Sci. Process. 74, s895–s897 (2002)